Reliability Modeling and Parametric Yield Prediction of GaAs Multiple Quantum Well Avalanche Photodiodes

A Thesis
Presented to
The Academic Faculty

by

Ilgu Yun

In Partial Fulfillment
of the Requirements for the Degree of
Doctor of Philosophy
in Electrical and Computer Engineering

Georgia Institute of Technology

October 1997

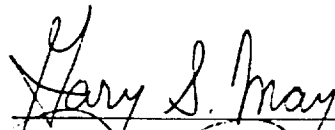# Reliability Modeling and Parametric Yield Prediction of GaAs Multiple Quantum Well Avalanche Photodiodes
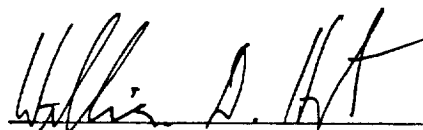
Approved:

Hary S. May

Dr. Gary S. May, ECE, Chairman

[signature]

Dr. Kevin F. Brennan, ECE

[signature]

Dr. William D. Hunt, ECE

Date approved by Chairman ___11/20/97___

ii

Dedication

To my parents with love

ACKNOWLEDGEMENTS

TABLE OF CONTENTS

CHAPTER

LIST OF TABLES

LIST OF FIGURES

SUMMARY

Reliability modeling and parametric yield prediction of GaAs/AlGaAs multiple quantum well (MQW) avalanche photodiodes (APDs), which are of interest as an ultra-low noise image capture mechanism for high definition systems, have been investigated.

First, the effect of various doping methods on the reliability of GaAs/AlGaAs multiple quantum well (MQW) avalanche photodiode (APD) structures fabricated by molecular beam epitaxy is investigated. Reliability is examined by accelerated life tests by monitoring dark current and breakdown voltage. Median device lifetime and the activation energy of the degradation mechanism are computed for undoped, doped-barrier, and doped-well APD structures. Lifetimes for each device structure are examined via a statistically designed experiment. Analysis of variance shows that dark current is affected primarily by device diameter, temperature and stressing time, and breakdown voltage depends on the diameter, stressing time and APD type. It is concluded that the undoped APD has the highest reliability, followed by the doped well and doped barrier devices, respectively.

To determine the source of the degradation mechanism for each device structure, failure analysis using the electron-beam induced current method is performed. This analysis reveals some degree of device degradation caused by ionic impurities in the

passivation layer, and energy-dispersive spectrometry subsequently verified the presence of ionic sodium as the primary contaminant. However, since all device structures are similarly passivated, sodium contamination alone does not account for the observed variation between the differently doped APDs. This effect is explained by dopant migration during stressing, which is verified by free carrier concentration measurements using the capacitance-voltage technique.

Reliability modeling provided the estimation of performance metrics as a function of process variables. Since literally millions of these devices must be fabricated for imaging arrays, it is critical to evaluate potential performance variations of individual devices in light of the realities of semiconductor manufacturing. Even in a defect-free manufacturing environment, random variations in the APD fabrication process lead to varying levels of device performance. Accurate device performance prediction requires precise characterization of these manufacturing variations. Therefore, a novel methodology for modeling the parametric yield prediction of GaAs MQW APDs has been presented.

The approach described requires a model of the probability distribution of each of the relevant process variables, as well as a model to account for the correlation between this measured process data and device performance metrics. The availability of these models enables the computation of the joint density function required for predicting performance using the Jacobian transformation method. The resulting density function can then be numerically integrated to determine parametric yield. Since they have demonstrated the capability of highly accurate function approximation and mapping of

complex, nonlinear data sets, neural networks are proposed as the preferred tool for generating the models described above. In apply this methodology to the MQW APDs, it was shown that using a small number of test devices with varying active diameters, barrier and well widths, and doping concentrations enables accurate prediction of the expected performance variation of APD gain and noise in larger populations of devices. This approach will ultimately allow device yield prediction prior to high volume manufacturing in order to evaluate the manufacturability   rely on both design specifications and process capability.

CHAPTER 1

INTRODUCTION

1.1 Background and Motivation

As semiconductor manufacturing technology continues to rapidly develop, device

dimensions decrease and the speed of computing and communication systems increases.

Therefore, analyzing the sensitivity of the yield and performance of these systems to

fluctuations in manufacturing processes is important. These fluctuations can influence

the statistically distributions of device model parameters, which result in statistically

varying performance characteristics in finished integrated circuits. Although small

process fluctuations may not always cause catastrophic failures, they often cause systems

not to meet certain specifications. ICs are often categorized (or priced) according to

specific performance criteria, and these criteria are directly influenced by variations in

individual device parameters (such as gain or noise in an avalanche photodiode). It is

therefore crucial for circuit and device designers, as well as manufacturers, to account for

statistical variations early in the design level, thereby aiding in production scheduling and

planning.

Recently, device simulators such as ATLAS [1] have been used to predict performance during the design phase. These simulators rely on analytical expressions and deterministic algorithms to simulate the behavior of semiconductor devices. For example, in the case of avalanche photodiodes (APDs), the breakdown voltage, dark current, light current and ionization rates for electrons and holes computed by ATLAS are based on nominal values of device model and manufacturing process parameters, and the effects of random parameter fluctuations are usually disregarded. This can cause a misleading interpretation of the results, since circuit behavior can be affected significantly by seemingly insignificant changes in a few critical model parameters.

It is therefore important for a designer to be able to verify the behavior of a system not only under nominal conditions, but also when appropriate changes are made to the device model parameters to reflect process fluctuations. Statistical process simulators such as FABRICS [2][3] have been developed to account for variations in device parameters. However, most attempts made in this direction thus far rely on Monte Carlo simulations to predict parametric yield. In Monte Carlo techniques, a large number of pseudo-random sets of values for the device model parameters are generated based on the means and standard deviations extracted from electrical test data. For each set of parameters, a simulation is performed to obtain information about the behavior of the circuit, and performance distributions are then extracted from the set of simulation results. Thus, although they are currently used in many applications, Monte Carlo techniques suffer from several drawbacks.

The most obvious disadvantage of the Monte Carlo approach is that it requires large numbers of simulations, and is therefore very computationally expensive. More importantly though, Monte Carlo simulations typically vary each device parameter independently, and in so doing, ignore the highly correlated nature of device parameters. The result of this oversight is often overly pessimistic and inaccurate performance predictions. Another disadvantage of Monte Carlo simulations is that they must assume a specific statistical distribution a priori in order to "randomly" generate sets of device and/or process parameters. In most cases, a normal distribution (with a given mean and variance) is assumed. For a mature, well-characterized fabrication process which has been used to manufacture large numbers of ICs, this assumption might be acceptable. However, newly developed or highly specialized processes often exhibit non-standard statistical behavior. Distributions of parameters from such processes as this may possess significant skew or kurtosis, or they may not even be normal at all. Thus, simulation methods which attempt to account for parameter variation should not assume normally distributed data arbitrarily, but should instead more accurately reflect the statistics of the fabrication process used.

The approach presented in this thesis seeks to develop a statistical device simulation and modeling tool that will allow designers to observe and account for the effects of parameter fluctuations early in the design cycle, providing significantly more manufacturable products. This will be accomplished by computing circuit parametric yield numerically from integrals of the form:

$$\int p(y)dy \quad\quad\quad (1.1)$$

where y is a particular device performance characteristic (such as gain or noise) and p(y) is its probability density function (pdf). P(y) can be derived by: (1) measuring or simulating a statistically significant sample of device parametric data; (2) using neural networks to encode the probability distributions of the measured data, obtaining the joint probability density function of all the marginal pdf's of the measured parameters; and (3) computing p(y) directly from the joint pdf using a standard mathematical transformation.

This approach advances the state-of-the-art in IC parametric yield prediction due to the following: (1) the use of actual measured data, rather than mathematical models, to generate statistical device parameter density functions [4]; (2) the innovative use of neural networks, rather than adaptive local fitting techniques, to model the density functions [5]; and (3) the direct computation of the device performance distributions, thus avoiding slow, computationally intense, and potentially inaccurate Monte Carlo techniques.

Current methodology for predicting parametric yield involves computationally intensive Monte Carlo simulations of parameter variations. One of the major advantages of the new methodology will be to eliminate the need for such simulations, and to replace these methods with the use of actual probability distribution models generated from measured test data. Upon successful completion, this methodology is expected to provide device designers with the ability to understand the manufacturability of various design

options and enable process engineers to extrapolate the consequences of process modifications by processing a relatively small set of test structures.

These capabilities will ultimately allow device yield prediction prior to high-volume manufacturing in order to evaluate the impact of both design decisions and process capability. In the applying this methodology to the MQW APDs, it is shown in this thesis that using a small number of test devices with varying active diameters, barrier and well widths, and doping concentrations enables accurate prediction of the expected performance variation of APD lifetime, gain and noise in large populations of devices.

1.2 Reliability Modeling

One of the two main objectives of this thesis is to accurately model the reliability of GaAs multiple quantum well (MQW) avalanche photodiodes (APDs). Reliability modeling of undoped, doped-barrier, and doped-well GaAs MQW APDs has been performed via accelerated life testing, and failure mode analysis was conducted using the electron beam induced current (EBIC) method, energy dispersive spectrometry (EDS) analysis and capacitance-voltage measurements. Since an increase in dark current results in a reduction of APD signal-to-noise ratio and breakdown voltage determines the operational voltage range of the device, these two parameters represent the most sensitive indicators of the characteristic degradation in these devices. Thus, dark current and breakdown voltage were the parameters monitored. The results of the life testing were

used to estimate device lifetime by assuming an Arrhenius-type temperature dependence [6]. Using the median device lifetime and its standard deviation as parameters, a failure probability model of these devices was derived using a lognormal failure distribution [7].

Reliability modeling allows the prediction of device lifetime as a function of process variables, but even in a defect-free manufacturing environment, random variations in the fabrication process will lead to varying levels of device performance. These manufacturing variations result from the fluctuation of various physical parameters (i.e. - doping concentration, layer thickness, etc.), which in turn manifest themselves first as variations in APD device operation (as characterized by breakdown voltage or dark current), and finally as variations in device performance metrics (such as gain, noise and device lifetime). Therefore, to enhance the manufacturability of GaAs MQW APDs, the effect of manufacturing parameters on the reliability of MQW APDs has to be identified.

1.3 Overview of Parametric Yield Prediction

The second objective of this work is to develop a methodology for statistical yield prediction of the parametric performance of these devices given the realities of the fabrication process. From the reliability modeling, accurate comprehensive device performance prediction requires precise characterization of variations in device performance metrics. Therefore, a methodology for modeling parametric performance based on manufacturing variations needs to be developed.

This first requires a model to be developed which reflects the probability distribution of each of the relevant process variables. This model can be obtained directly from measured process data. A second model is then required to account for the correlation between this measured process data and device performance metrics. This can be derived either from the evaluation of analytical expressions relating process variables to performance or through device simulation. The availability of the above models enables the computation of the joint probability density function required for predicting performance using the Jacobian transformation method [8], which converts the process variable distributions to the device performance metric distributions. The resulting density function can then be numerically integrated to determine parametric yield. Since they have demonstrated the capability of highly accurate function approximation and mapping of complex, nonlinear data sets, neural networks are proposed as the preferred tool for generating the models described above [9-12].

1.4 Thesis Organization

The remainder of this thesis is constructed to explore the reliability modeling of various GaAs MQW APD structures and to investigate the statistical prediction of parametric performance. Chapter 2 provides a brief summary of previous work regarding the characterization and modeling of avalanche photodiodes and a detail device description and an explanation of the operation of APDs investigated here. Chapter 3

describes the reliability modeling of various GaAs MQW APD structures in detail and investigates the device lifetime of each APD structure. Chapter 4 explains the ATLAS device simulator and demonstrates how ATLAS simulations can be calibrated to closely match measurement data. Chapter 5 discusses device modeling using neural networks. Using data generated from the ATLAS simulator, performance metrics, such as gain, noise, and device lifetime, were modeled and the sensitivity of each performance metrics was also investigated.

The modeling results described above can be used to predict the parametric yield of each performance metric with respect to the manufacturing parameters. A methodology for doing so is presented in Chapter 6 where a detailed explanation of the procedures necessary to calculate parametric yield is provided. In addition, this methodology to predict parametric yield is compared with Monte Carlo method. Finally, Chapter 7 draws conclusion regarding this work and provides suggestions for future work.

CHAPTER 2

AVALANCHE PHOTODIODES

2.1 Historical Development

The widespread development of high-speed detector applications, such as optical fiber communication systems and high definition systems, has been responsible for renewed interest in compound semiconductor photodetectors [13]. For these applications, a photodetector is an important component, and the following crucial requirements must be met by these devices: 1) detection and transformation of the incoming light pulse stream at high quantum efficiency (the number of electron-hole pairs generated per incident photon), high speed, and with low dark current, low capacitance, and low noise, 2) amplification of the electrical signal to levels high enough that thermal noise of the electronics becomes negligible, 3) provision of an appropriate interface to the main electronics [14][15].

Among photodetectors, avalanche photodiodes (APDs) are considered an alternative to photomultiplier tubes (PMTs) in some applications because of enhanced sensitivity. One of the main advantages of APDs is their high signal-to-noise ratio due to internal gain resulting from the avalanche multiplication process, even though

multiplication can also generate excess noise. Avalanche photodiodes have been developed in various semiconductor materials, including elementary semiconductors such as silicon and germanium, as well as binary, ternary and even quarternary III-V and II-VI compound semiconductors. For the wavelength range of 1.3 to 1.55 μm, photodetectors are primarily made out of III-V materials, such as AlGaAs/GaAs, InGaAs/InP, InGaAs/GaAs, InGaAsP/InP, GaAlAsSb/GaSb, GaAs/InP, and InP/GaAs, because dark current is inversely proportional to the energy gap and these materials have relatively wide bandgaps. Other key factors in selecting the appropriate material system for a detector include the operational wavelength range and gain and noise performance.

Silicon APDs provide a high ratio of electron and hole ionization coefficients which results in optimal performance at the 0.8-μm wavelength region. Silicon APDs were first investigated by Heitz et al. [16], and Kaneda [17] surveyed reach-through structure and characteristics of Si APDs. In silicon APDs, multiplication noise decreases as the avalanche region length increase because the hole-to-electron ionization coefficient ratio also decreases. In addition, quantum efficiency is improved as the depletion length increases, which leads to increased the breakdown voltage. However, silicon is not sensitive to the 1.3- to 1.6-μm wavelengths, and since the ionization coefficient ratio is a function of the electric field, impact ionization must be initiated by electrons to reduce the electric field in the avalanche region and to minimize the excess noise.

Germanium APDs are useful in the wavelength range from 1.0 to 1.6 μm, and since these APDs provide high quantum efficiency, they are suitable for fiber optic

systems [18]. However, they yield a poor signal-to-noise ratio because the ionization coefficients of electrons and holes are almost equal, and the dark current of germanium APD at room temperature is relatively high due to its smaller bandgap.

InP APDs have also been reported as a component in optical communication systems because they have excellent characteristics, including low noise and high sensitivity in the 1 - 1.6 µm wavelength range [19]. These characteristics are crucial requirements for receivers in optical communication systems. However, InP structures have suffered from high leakage currents. This problem arises from the nearly equal values of electron and hole ionization coefficients in InP.

To improve the sensitivity of APDs, the ratio of ionization coefficients must be increased. As demonstrated by McIntyre (1966), a large difference in the ionization rates for electrons and holes is essential for a low-noise APD [20]. APD performance is enhanced by minimizing the excess noise generated by carrier multiplication. This excess noise is reduced when the ratio of the ionization rate of electrons to that of holes (or vice-versa) is large. Chin et. al. first proposed a means of artificially enhancing the ratio of electron-to-hole ionization coefficients through use of a MQW structure in the GaAs/AlGaAs material system [21]. Later, Brennan and Summers analyzed the use of the doped quantum well APD as a photomultiplier [22], and Aristin et. al. evaluated various MQW APD structures, including the undoped, doped-barrier, and doped-well devices [23]. These new structures enable very low noise and high-speed performance. However, the noise performance of MQW APDs is limited by dark currents due to both thermionic emission and field-assisted tunneling of carriers out of quantum wells.

11

Therefore, increased dark current can severely limit the long-term reliability of these devices.

Reliability assessment of avalanche photodiodes has been performed by several authors. Sudo et al. conducted accelerated life tests on germanium APDs to measure their failure rates under practical use conditions [24]. This author also used bias temperature tests and the light-beam induced current method to evaluate lifetime and analyze the failure modes of InP/InGaAs APDs [25][26]. Kuhara likewise investigated the long-term reliability of InGaAs/InP photodiodes passivated with polyimide films [27], and Bauer and Trommer performed a similar investigation on devices passivated with silicon nitride [28]. Finally, Skrimshire, et. al. performed accelerated life tests on both mesa and planar InGaAs photodiodes for comparison purposes [29].

2.2 Applications

High-speed, high-sensitivity APDs are used in variety of applications including fiber optic communication systems, and high definition imaging systems [30][31]. Recently, APDs have been used in high-bandwidth receiver modules for fiber optic communication systems to provide greater signal-to-noise ratio. To increase high bit rate in fiber optic communication networks requires the enhancement of suitable high performance optoelectronic component. The APD is used at the receiving end of the fiber to convert the optical signal into an electrical current which can be processed to recover

the original data. For low bit rate and short range applications such as a local area networks, the strict device performance is not necessarily needed. However, for high bit rate and long distance applications, the high-speed and reliable device performance is required. For these applications, preamplifier input noise can limit the receiver sensitivity. To alleviate this problem, an APD is used to provide signal gain before the preamplifier input. The enhanced signal-to-noise ratio permits effective processing of the output by a subsequent receiver.

Another application for APDs is in the development of imaging systems for both the visible and non-visible portions of the spectrum. While fiber optic communication systems are usually limited to the 1.3-1.55 μm spectral range, the imaging systems can utilize a wide range of materials to operate in a variety of optical ranges depending on the application. In such systems, the APD can capture the optical images and amplify the signal using its internal gain properties.

Currently, a high definition television imaging system is under investigation at the Georgia Tech Microelectronic Research Center. This system faces a number of unique manufacturing challenges. The system uses a 1920 x 1080 imaging array of superlattice avalanche photodiodes as its image capture mechanism operating at wavelengths below 1 μm. GaAs/AlGaAs multiple quantum well (MQW) avalanche photodiodes (APDs) are of interest as an ultra-low noise image capture mechanism for this system. In this application, the image capture stage must have sufficient optical gain to enable very sensitive light detection, but at the same time, the gain derived during detection must not

contribute additional noise. Various APD structures, including doped-barrier, doped-well, and undoped devices have been fabricated, and these structures are all being considered as candidates for this application.

2.3 Device Description of the GaAs/AlGaAs MQW APD
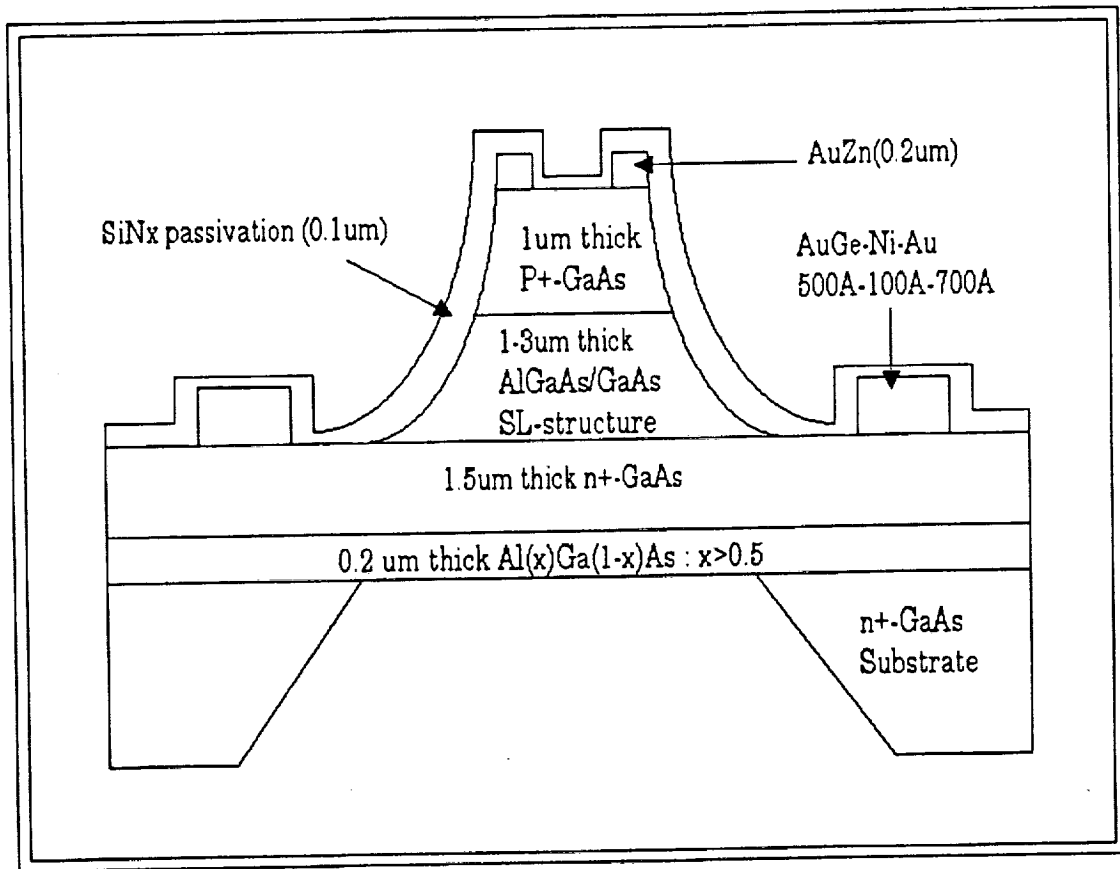
Figure 1. Cross sectional view of GaAs/AlGaAs MQW APD

14

The device structure of the photodiodes investigated in this thesis is shown in Figure 1. The devices were grown by molecular beam epitaxy (MBE) in a Varian Gen-II system at the Georgia Tech Research Institute. The basic structure is that of a p-i-n diode where the intrinsic region is composed of the MQW superlattice structure. All APDs were composed of a 1 µm Be-doped p+ top layer and a 1.5 µm Si-doped n+ backside layer. The p and n contact layers are doped at a level of 10^{18} cm^{-3} [23]. The device configuration allows for both electron and hole injection because both p$^+$ and n$^+$ layers can be illuminated.

The devices were fabricated on 2×10^{-4} cm^2 mesa structures with an active diameter in the range of 75-130 µm using standard photolithographic techniques. Since both the p and n layers can be illuminated by removing the substrate, the device configuration allows for electron or hole injection [32]. A silicon nitride passivation coating suppresses surface leakage current and provides the device with very low dark currents. The fabrication process for these structures is summarized in Figure 2. The choice of the various doping techniques indicated in this figure has a significant effect on device performance.

```
┌─────────────────────────────────────────────────────┐
│  ┌───────────────────────────────────────────┐      │
│  │      Substrate Preparation & Mounting      │      │
│  └───────────────────────────────────────────┘      │
│        ┌───────────────────────────────┐            │
│        │          Deoxidation          │            │
│        └───────────────────────────────┘            │
│  ┌───────────────────────────────────────────┐      │
│  │  Prebake & cooling to growth temperature   │      │
│  └───────────────────────────────────────────┘      │
│     ┌────────────────────────────────────┐          │
│     │    Doping n+GaAs substrate by Si    │          │
│     └────────────────────────────────────┘          │
│   ┌───────────────────────────────────────┐         │
│   │    Doping GaAs N contact layer by Si   │         │
│   └───────────────────────────────────────┘         │
│        ┌──────────────────────────────┐             │
│        │  Growth of superlattice by MBE │             │
│        └──────────────────────────────┘             │
│                                                      │
│  ┌───────────────┐ ┌────────────────┐ ┌───────────────┐ │
│  │  Undoped APD  │ │ Doped Barrier  │ │ Doped Well APD│ │
│  │               │ │      APD       │ │               │ │
│  └───────────────┘ └────────────────┘ └───────────────┘ │
│  ┌───────────────┐ ┌────────────────┐ ┌───────────────┐ │
│  │ Grow undoped  │ │ Grow p+n+ doped│ │ Grow undoped  │ │
│  │ AlGaAs/GaAs   │ │ junction in    │ │ AlGaAs barrier│ │
│  │ multilayers   │ │ AlGaAs         │ │ & p+n+ doped  │ │
│  │               │ │ barrier &      │ │ junction      │ │
│  │               │ │ undoped        │ │ in GaAs well  │ │
│  │               │ │ GaAs well      │ │               │ │
│  └───────────────┘ └────────────────┘ └───────────────┘ │
│                                                      │
│     ┌────────────────────────────────────┐          │
│     │      Doping GaAs P contact layer    │          │
│     └────────────────────────────────────┘          │
│         ┌──────────────────────────┐                │
│         │     Mount P+ contact      │                │
│         └──────────────────────────┘                │
│         ┌──────────────────────────┐                │
│         │    Etch Mesa structure    │                │
│         └──────────────────────────┘                │
│         ┌──────────────────────────┐                │
│         │     Mount N+ contact      │                │
│         └──────────────────────────┘                │
│       ┌────────────────────────────────┐            │
│       │  Deposit passivation layer (SiNx) │          │
│       └────────────────────────────────┘            │
└─────────────────────────────────────────────────────┘
```

Figure 2. The fabrication process for various APD structures

For the doped-barrier MQW APDs, the 1-3 µm thick GaAs/AlGaAs superlattice region consists of 25 periods of 200 Å GaAs quantum wells separated by 800 Å AlGaAs barrier layers. One complete period consists of a 300 Å high-field AlGaAs region doped at 3×10^{18} cm^{-3}, the 200 Å undoped GaAs layer, and a 500 Å undoped AlGaAs layer. The I-V characteristics indicate a low dark current and a low breakdown voltage to be between 6 and 8 V, more than an order of magnitude lower than that of conventional MQW APD structures. The low voltage operation is due to the localized breakdown arising from the fully depleted p-i-n regions within each unit cell. Consequently, the doped barrier structures are more efficient devices than conventional APD structures, and these structures are better suited to on-chip, low power environments.

In the doped-well devices, high electric fields are achieved in the narrow bandgap GaAs wells of the avalanche region by the introduction of 50 Å thick p+ and n+ layers doped at 1.5×10^{18} cm^{-3} [33]. The doped quantum well MQW APD structure is complementary to the doped barrier APD devices and possibly allows more stable doping characteristics. The breakdown voltages of doped-well MQW APDs are slightly higher than the doped barrier devices because of the use of lower doping. The electron to hole ionization ratio is between 10 to 33 at low gains but decreases for gains higher than 5 to approximately 5. These results confirm that, at low bias voltages, the built-in field due to the doping produces lower noise, and at higher bias voltages, the applied field makes the electron and hole ionization rates more equal. Consequently, superior performance of the doped structures with lower bias voltage, higher gain, and lower excess noise than the undoped conventional MQW APDs has been suggested [34].

The undoped MQW APD design is similar, but with the MQW region replaced by a 2.5 µm intrinsic GaAs layer. For the undoped MQW structure, dark current decreases with decreasing well width, and the photocurrent increases slowly with the applied bias voltage, becomes constant between 25-35 V and finally increases exponentially above 50 V. In addition, the breakdown voltage, V_B, increases from 70 to 85 V as the barrier (AlGaAs layer) width is increased from 200 Å to 800 Å. These results indicate that the dark current is due to the generation-recombination of carriers in the narrow bandgap GaAs layer combined with thermionic emission of the carriers over the barriers. The carriers are generated in the well since the dark current increases when the well width increases. However, the thick barriers do not permit carriers to tunnel and carriers need to gain enough energy from the applied field to be injected over the barriers and avoid being trapped at the AlGaAs/GaAs interface. Therefore, MQW structures with narrow well widths have increased barrier height, resulting in lower dark currents.

2.4 Device Operation of GaAs MQW APD

Although electron-hole pairs created in the depletion region are quickly separated by the electric field at the junction in homostructure PIN photodiodes, heterostructure APDs transform an optical input signal into an electric output signal using an avalanche gain mechanism. In APDs, avalanche gain is achieved when the incident or

photogenerated free carriers obtain sufficient energy from the electric field to generate secondary free carriers by impact ionization of the valence electrons into the conduction band, leaving free holes in the valence band. Secondary carriers can then be accelerated by the electric field and generate more carriers by impact ionization of other valence electrons. The generation of electron-hole pairs and avalanche gain depend on the impact ionization rates and the electric field, and the electric field required to observe impact ionization depends on the band gap of the material. As a result of impact ionization, a large number of electron-hole pairs are generated, and a considerably large output signal can be obtained even for relatively small input signals [35].

The band diagram of multiple quantum well APD (shown in Figure 3) illustrates alternating layers of high-gap and low-gap materials and represents the restriction of ionizing collisions to the low-gap regions. Carriers accelerate and gain energy but do not ionize in wide-gap regions. On entering the next well, a free electron gains enough energy from the conduction-band discontinuity ΔEc to ionize. However, the valence-band discontinuity ΔEv is not large enough to supply a similar energy boost to free holes. Thus, electrons enter the well with a higher kinetic energy than holes, so that electrons ionize more efficiently than holes if $\Delta Ec > \Delta Ev$. Hence, a small input optical signal can generate a substantial electrical output.
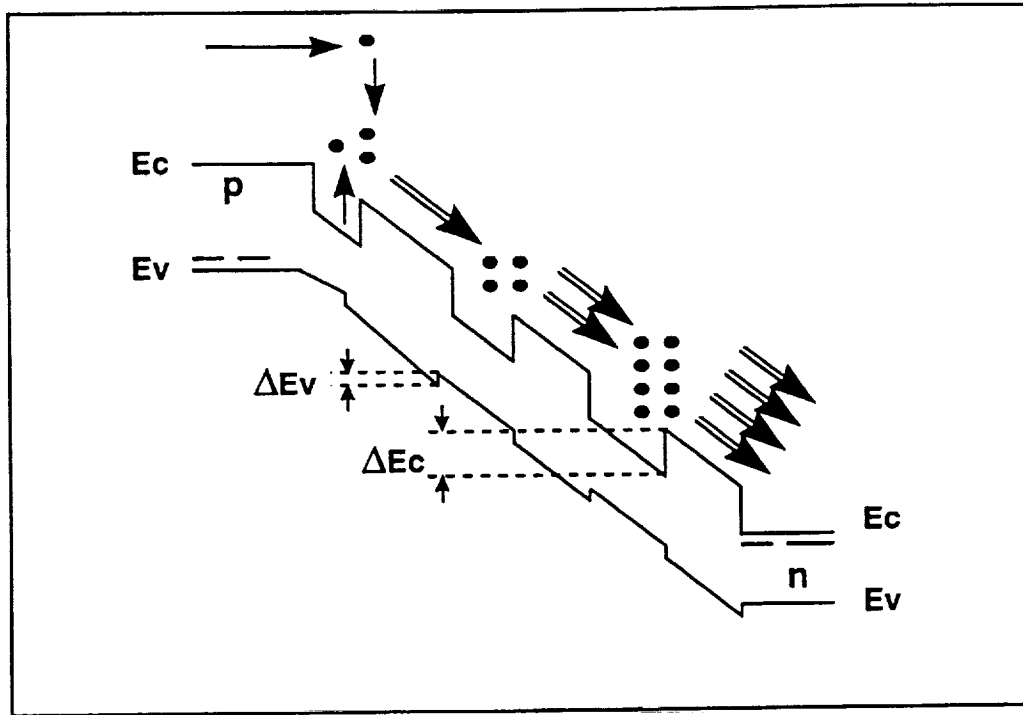
Figure 3 Schematic band diagram of multiple quantum well APD

Reduction of excess noise is crucial if an APD is to detect the low power levels of input signals that result from long wavelength applications. Avalanche multiplication, however, inherently creates extra noise, which adds to the shot noise of the incident carriers. This excess noise results from fluctuation of the avalanche gain. To limit the excess noise caused by avalanche multiplication, holes and electrons must ionize at vastly different rates. Using the multiple quantum well structure, one can artificially tailor the ratio of the ionization coefficients and therefore, reduce excess noise [36]. Examples of the gain and excess noise factors for the MQW APDs investigated in this study are shown in Figures 4 and 5.
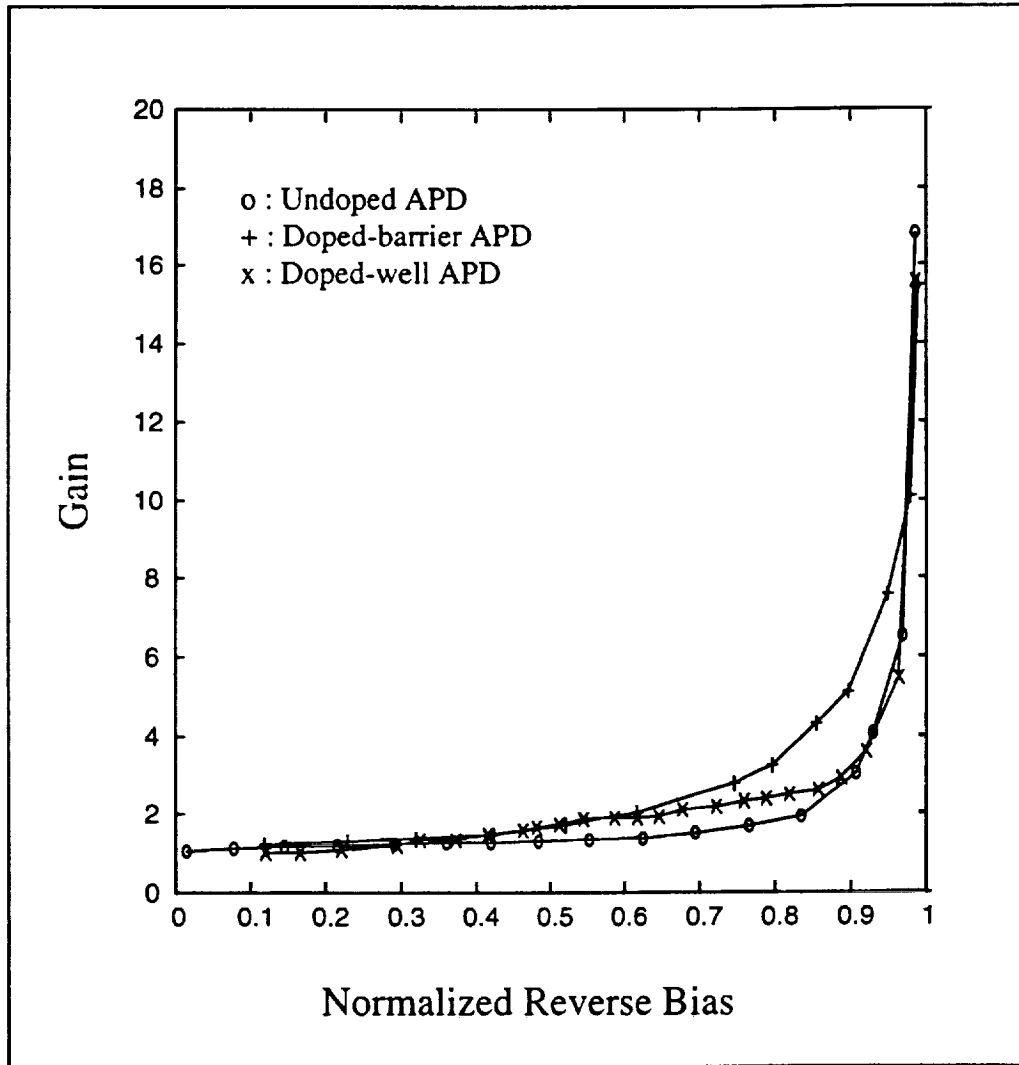
Figure 4 - Gain versus the ratio of reverse bias to breakdown voltage for the undoped, doped-barrier, doped-well MQW APDs under investigation.
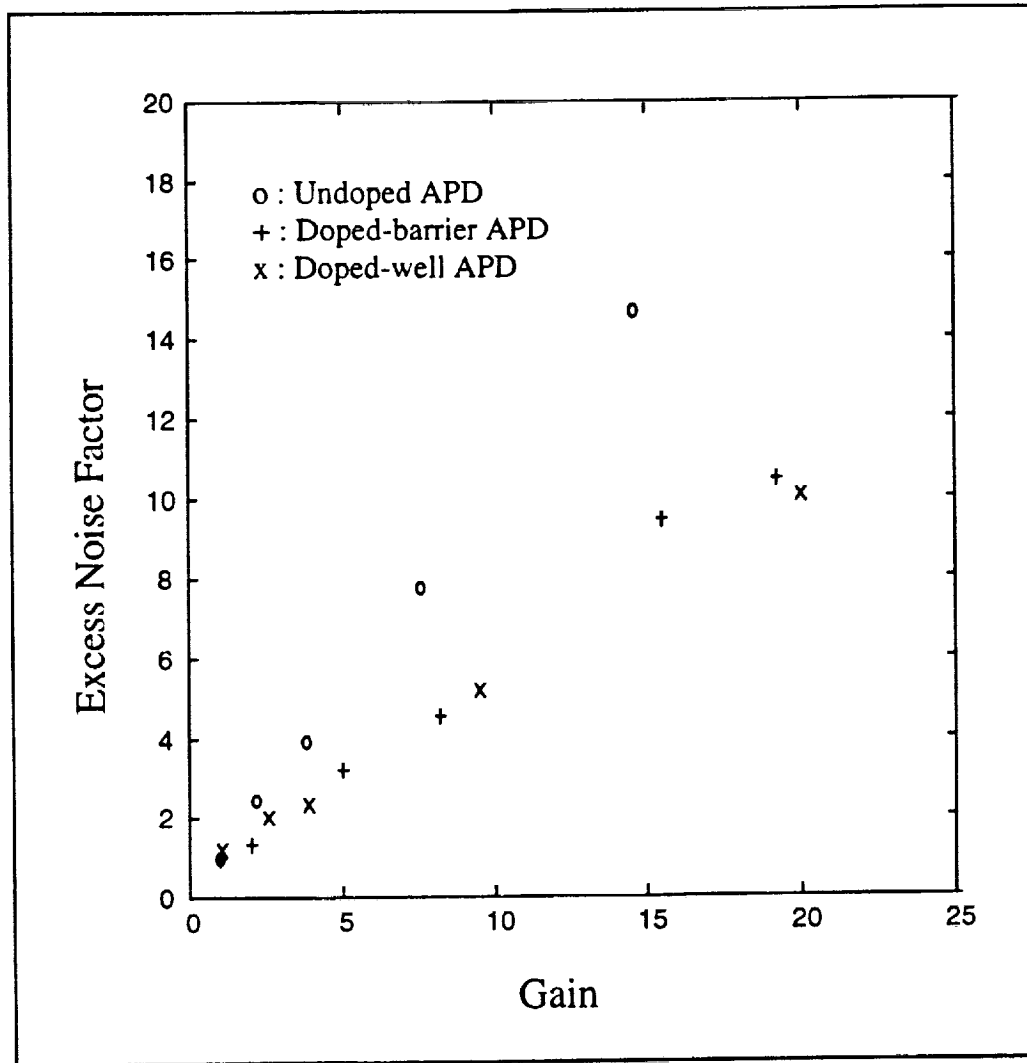
Figure 5 - Excess noise factors for the undoped, doped-barrier, doped-well MQW APDs under investigation.

APD gain and signal-to-noise ratio (SNR) are limited by the dark current in the device. The resulting increases in dark current due to carrier multiplication lead to reduced SNR. Dark current is therefore perhaps the most important performance parameter used to evaluate APD device reliability. The dark current density in general has the following form [37]:

$$J = qn_i \left[\frac{n_i L_p}{n_o \tau_p} + \frac{W}{2\tau_o} \right] + J_T + q\eta\phi_B \qquad (2.1)$$

where q is the electron charge, n_i and n_o are the intrinsic carrier and majority carrier concentrations, L_p and τ_p are the minority carrier diffusion length and lifetime, W is the depletion region width, t_o is the lifetime of the average of the excess minority carrier electron and hole lifetimes (i.e. - $\tau_o = (\tau_{po} + \tau_{no})/2$), η is the quantum efficiency, ϕ_B is the background photon flux, and J_T is the tunneling current. The first, second, third and fourth terms represent the diffusion, generation-recombination, tunneling and background radiation current densities, respectively.

From Equation (2.1), the diffusion current density is proportional to (L_p/τ_p), and the generation-recombination (g-r) current density is proportional to the depletion region width W. Since W is a function of the reverse-bias voltage, the g-r current density is also dependent on that voltage. This is especially significant for APDs operating at the high fields. This factor limits the utility of small band-gap semiconductors for APDs because

they must be operated at high reverse bias voltage. For effective detector performance, low breakdown voltage is a necessity and the three current densities in (2) must be minimized.

2.5 Summary

The historical development and current applications of APDs have been presented. Also, the detail description and the operating principle of GaAs/AlGaAs MQW APDs, which are of interest as ultra-low noise image capture mechanism for high definition system, have been introduced. In the next chapter, reliability study of three different GaAs/AlGaAs MQW APD structures, doped-barrier, doped-well, and undoped structure, will be investigated via accelerated life testing. In chapter 4, because of limited experimental data, the effect of variations in manufacturing parameters on performance metrics, such as device lifetime, gain, and noise, is investigated using simulated data. In chapter 5, the mapping from the manufacturing parameters to the performance metrics is realized by neural networks using the simulated data sets. Parametric yield calculation of each performance metric is presented in chapter 6.

CHAPTER 3

RELIABILITY MODELING OF GaAs MQW APD

3.1 Introduction

In this chapter, accelerated life testing of undoped, doped barrier, and doped well APD device structures is described with the objective of estimating long-term device reliability. Since an increase in dark current results in a reduction of the APD signal-to-noise ratio and breakdown voltage determines the operational voltage range of the device, these two parameters represent the most sensitive indicators of the characteristic degradation in these devices. Thus, dark current and breakdown voltage were the parameters monitored here. Degradation in these parameters was investigated via high temperature storage tests and accelerated life tests, and the results of these tests were used to estimate device lifetime by assuming an Arrhenius-type temperature dependence [6]. Using the median device lifetime and its standard deviation as parameters, a failure probability model of these devices was derived using a lognormal failure distribution [7].

Lifetimes for each device structure were examined via a statistically designed experiment. A comparison of the reliability of the various APD structures was then performed using the analysis of variance (ANOVA) technique [38]. Results of the ANOVA study revealed which input factors were found to have an significant effect on each response. Dark current was mainly dependent on device diameter, temperature and stress time. Breakdown voltage was primarily impacted by diameter, temperature and APD type. Based on the results of this investigation, it has been concluded that the undoped APD structure yields devices that exhibited the highest reliability, followed by the doped well and doped barrier devices, respectively.

Following device stressing, an analysis was conducted to determine the failure mechanism. Potential failure mechanisms were evaluated using scanning electron microscopy (SEM) and the electron-beam induced current (EBIC) method [39]. Based on SEM and EBIC analysis, the presence of ionic impurities contaminating the passivation layer at the junction perimeter was proposed as a potential failure mechanism. Energy-dispersive spectrometry (EDS) [40] was subsequently used to identify ionic sodium as the source of contamination. However, all three device structures are passivated using the same procedure. Therefore, sodium contamination alone could not account for the observed variation between the differently APD device types. On the contrary, this result is explained by dopant migration during stressing, which was verified by the measurement of free carrier concentration before and after stressing using the capacitance-voltage (C-V) technique [41].

3.2 Accelerated Life Testing

3.2.1 Life Test Conditions

Accelerated life tests for the three different APD structures were performed on several different devices of each type with a constant reverse current of 10 μA for 200 hours at three different ambient temperature levels: 100, 150 and 200 °C. These conditions are summarized in Table 1.

Table 1. Accelerated Life Tests Conditions

Temperature [°C]	Current [μA]	Number of Samples	Stress Time [hour]
100	10	4	200
150	10	6	200
200	10	6	200

The accelerated life tests measured the failure rate under stressful operating conditions. To maintain a constant 10 μA current, the reverse bias voltages for the doped-barrier, doped-well and undoped APD were approximately 8, 10 and 80 V, respectively. The activation energy for the failure mechanism and the average device lifetime were subsequently computed. It was assumed that the temperature dependence of the device failure rate (R) obeys the following Arrhenius law [6]:

$$R = R_o * \exp(-E_a / kT) \tag{3.1}$$

where R_o is a temperature-independent pre-exponential failure acceleration factor, E_a is the activation energy, T is the absolute temperature, and k is Boltzmann's constant. During these tests, dark current and breakdown voltage were measured at room temperature (300 °K) after high-temperature stressing. The breakdown voltage was obtained from the device I-V curve using the tangential line method. Typical breakdown voltages were 7.5 - 9 V for the doped-barrier APD, 10 - 12 V for the doped-well APD, and 70 - 85 V for the undoped APD. The devices were classified as failing when the dark currents at room temperature and 90% of the breakdown voltage exceeded 1 μA.

3.2.2 Life Test Results

Several observations were made as a result of the high temperature storage tests and accelerated life tests for the GaAs/AlGaAs APDs. First, unbiased baking of the APD samples resulted in significantly less degradation, which is demonstrated by a comparison of Figures 6 and 7. Dark current increases due to thermal overstress under bias for the doped-barrier devices were generally found to be exponentially dependent on the time of exposure to the reverse-bias field. The doped-well and undoped devices exhibited similar behavior. This fact is shown Figures 8-10(a), in which the dark current at a given

28

reverse-bias voltage increases significantly as a function of stress time. On the other

hand, breakdown voltage was shown to be nearly linearly dependent on stressing time, as

shown in Figures 8-10(b).
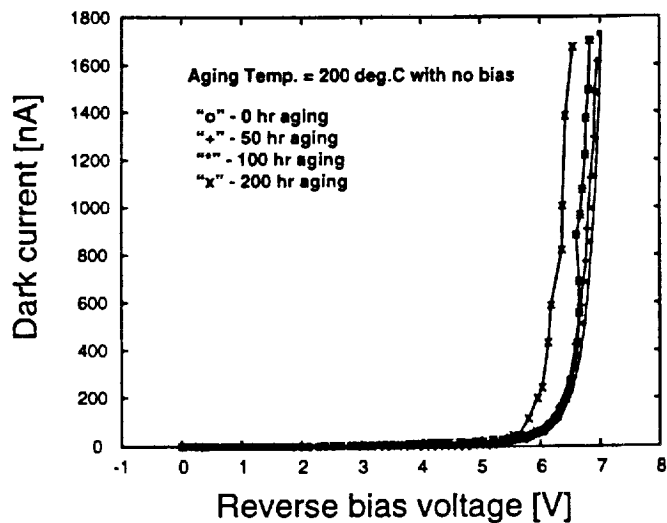
Figure 6. Room-temperature I-V curve of an doped-barrier APD sample after 0, 50, 100, and 200 hours of unbiased baking at 200 degrees C.
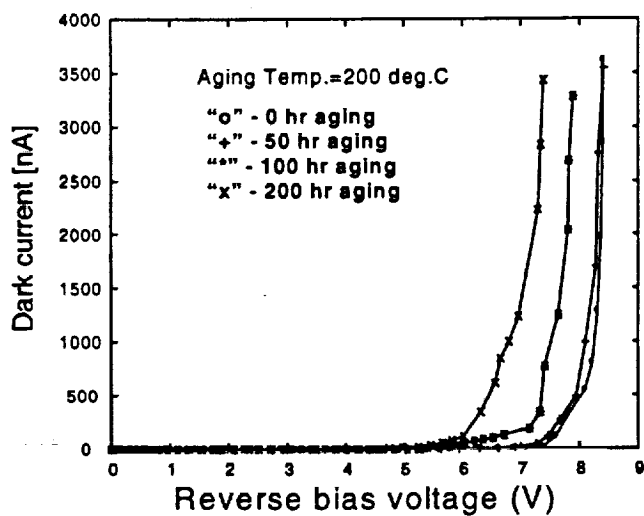
Figure 7. Room-temperature I-V curve of an doped-barrier APD sample after 0, 50, 100, and 200 hours of biased baking at 200 degrees C.

(a)

(b)
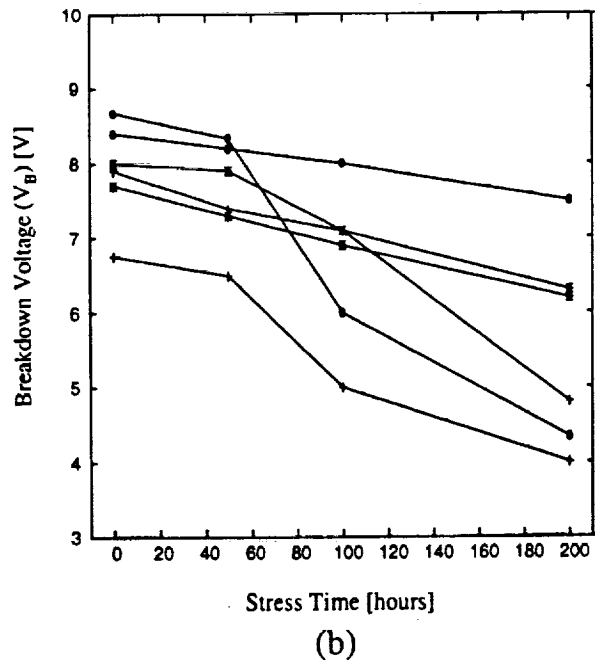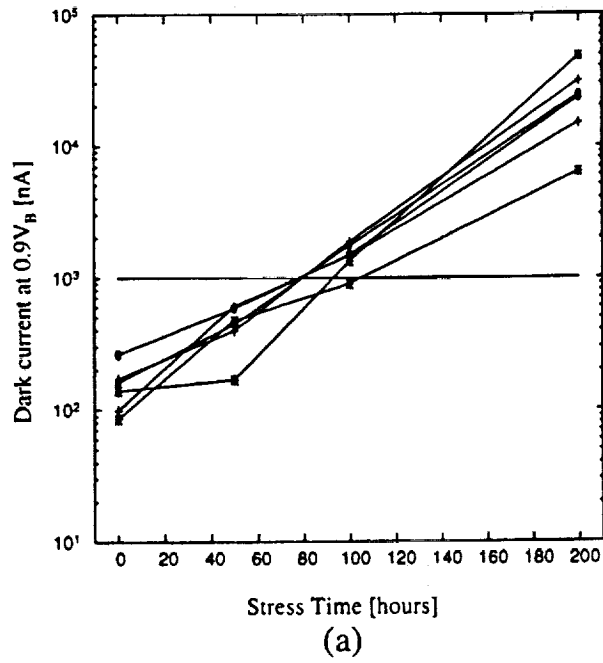
Figure 8. (a) Dark current and (b) breakdown voltage variations of doped-barrier APDs after accelerated life testing at 200 degrees C.
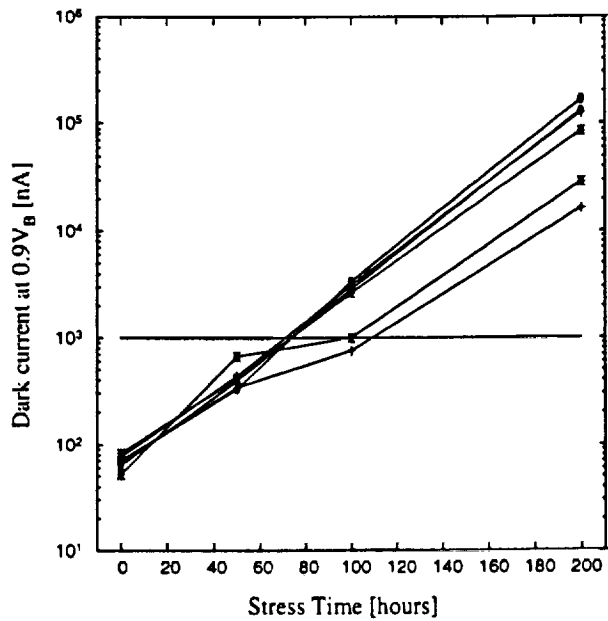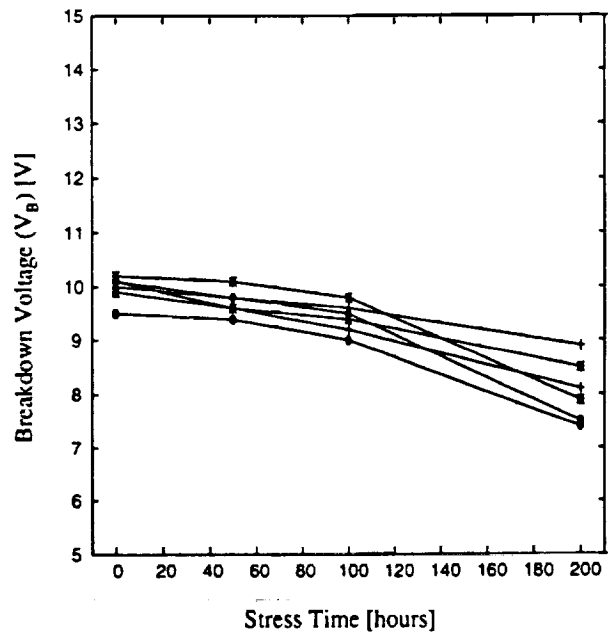
Figure 9. (a) Dark current and (b) breakdown voltage variations of doped-well APDs after accelerated life testing at 200 degrees C.
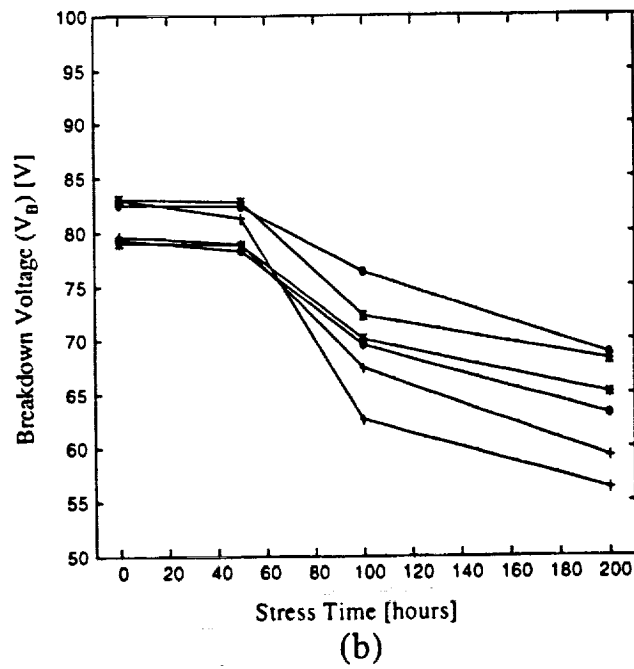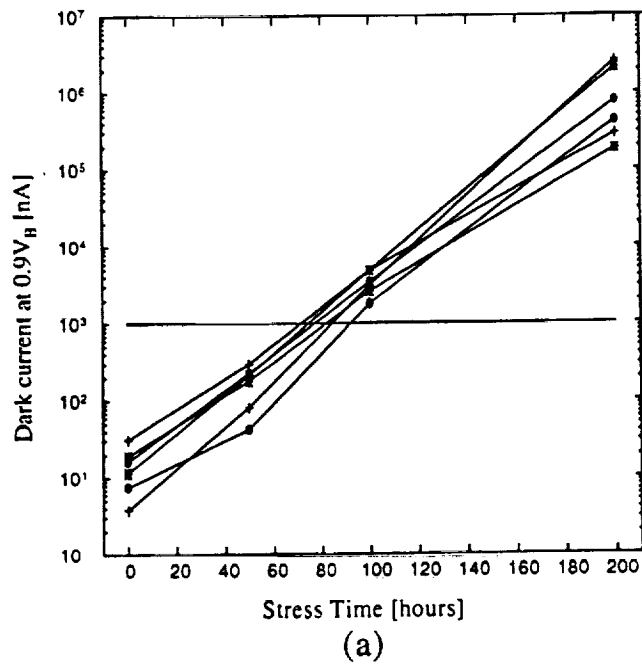
Figure 10. (a) Dark current and (b) breakdown voltage variations of undoped-APDs after accelerated life testing at 200 degrees C.

32

Figures 11-13 depict the percent of cumulative failures for the doped-barrier, doped-well, and undoped devices, respectively, versus the lognormal projection of the device time-to-failure after accelerated life testing. Although the sample size is small, in each case the data appears linear, which indicates that the failure mode is the wearout type. Failures obey the lognormal distribution relatively well. Median lifetimes for the doped-barrier devices at 100, 150, and 200 °C were estimated to be 1400, 250, and 78 hours, respectively, with a standard deviation of 1.84. For the doped-well APDs, median lifetimes at 100, 150, and 200 °C were estimated to be 4204, 315 and 86 hours, respectively, with a standard deviation of 1.94. Finally, in the undoped case, the median lifetimes at 100, 150, and 200 °C are estimated to be 8590, 495 and 84 hours, respectively, with a standard deviation of 2.13.

The Arrhenius plot of median lifetimes as a function of reciprocal aging temperature is shown in Figures 14-16. From these plots, the thermal activation energy of the device aging process is computed to be 0.44, 0.60, and 0.71 eV for the doped-barrier, doped-well and undoped devices, respectively. Using these activation energy levels, the median APD lifetime for the doped-barrier device under practical use conditions can be estimated to be 3.7×10^4 hours (approximately 4.3 years) at room temperature, with a standard deviation of 116 hours. Lifetime estimates for the doped-well and undoped cases were 3.4×10^5 hours (approximately 39 years) with a standard deviation of 343 hours and 1.7×10^6 hours (approximately 197 years) at room temperature, with a standard deviation of 1031 hours.

33
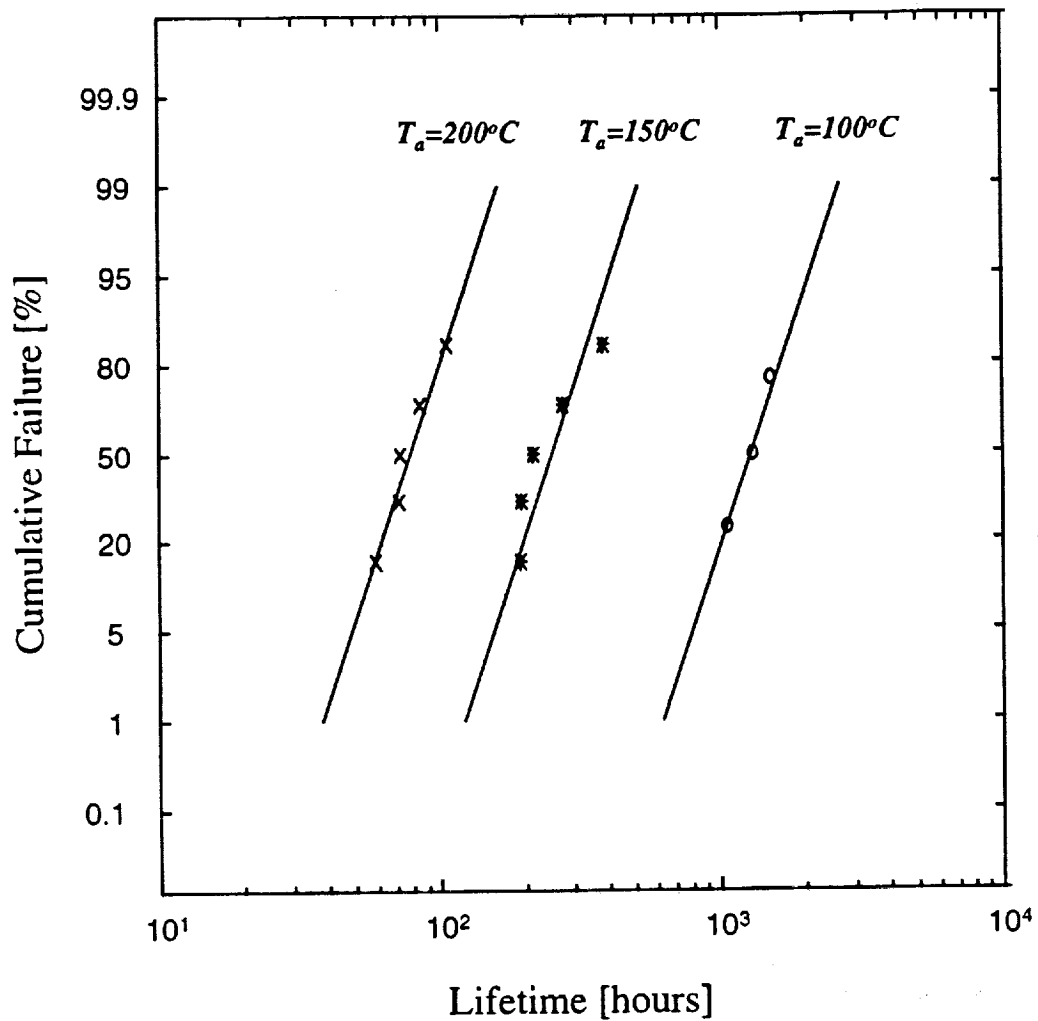
Figure 11. Lognormal projection of time-to-failure versus percent of cumulative failures for doped-barrier APDs after life testing at 100, 150, and 200 degrees C.
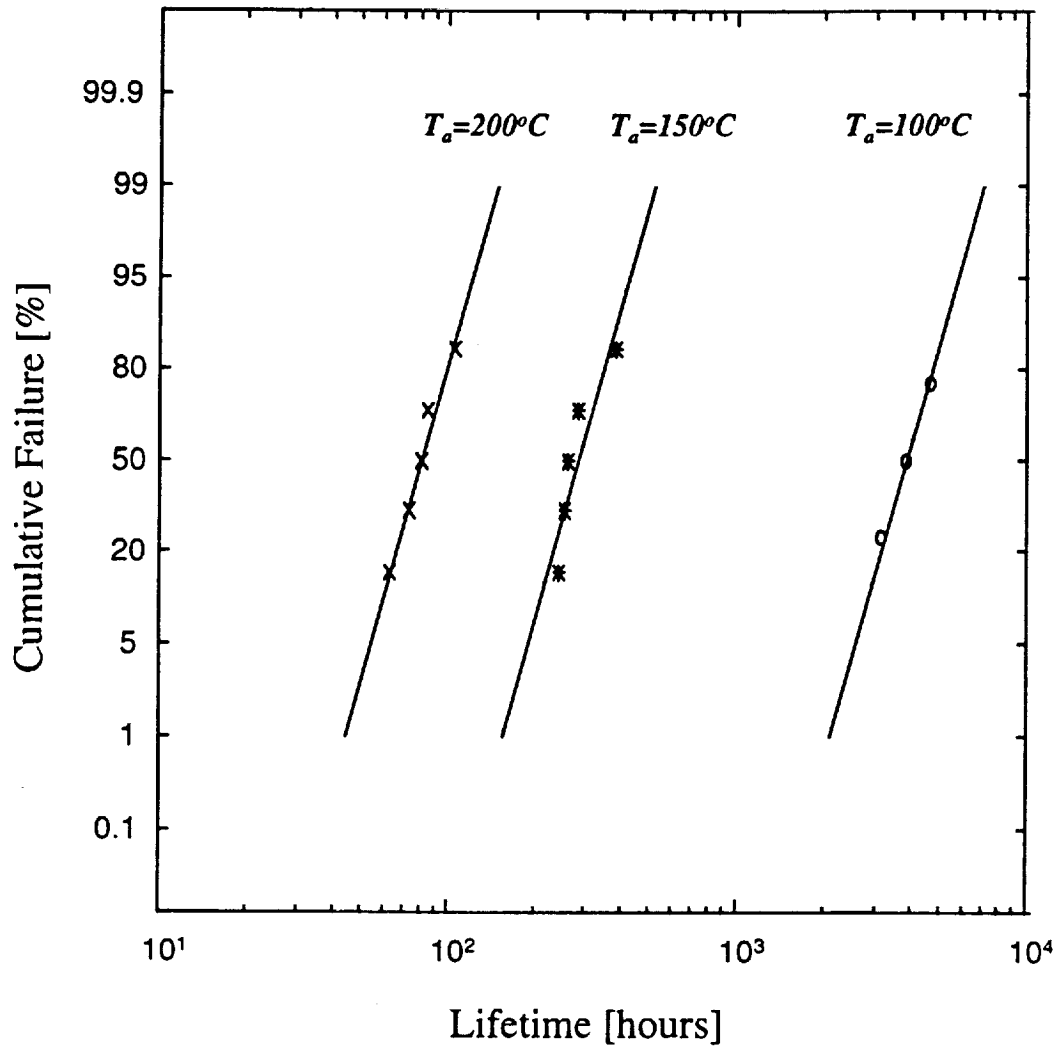
Figure 12. Lognormal projection of time-to-failure versus percent of cumulative failures for doped-well APDs after life testing at 100, 150, and 200 degrees C.
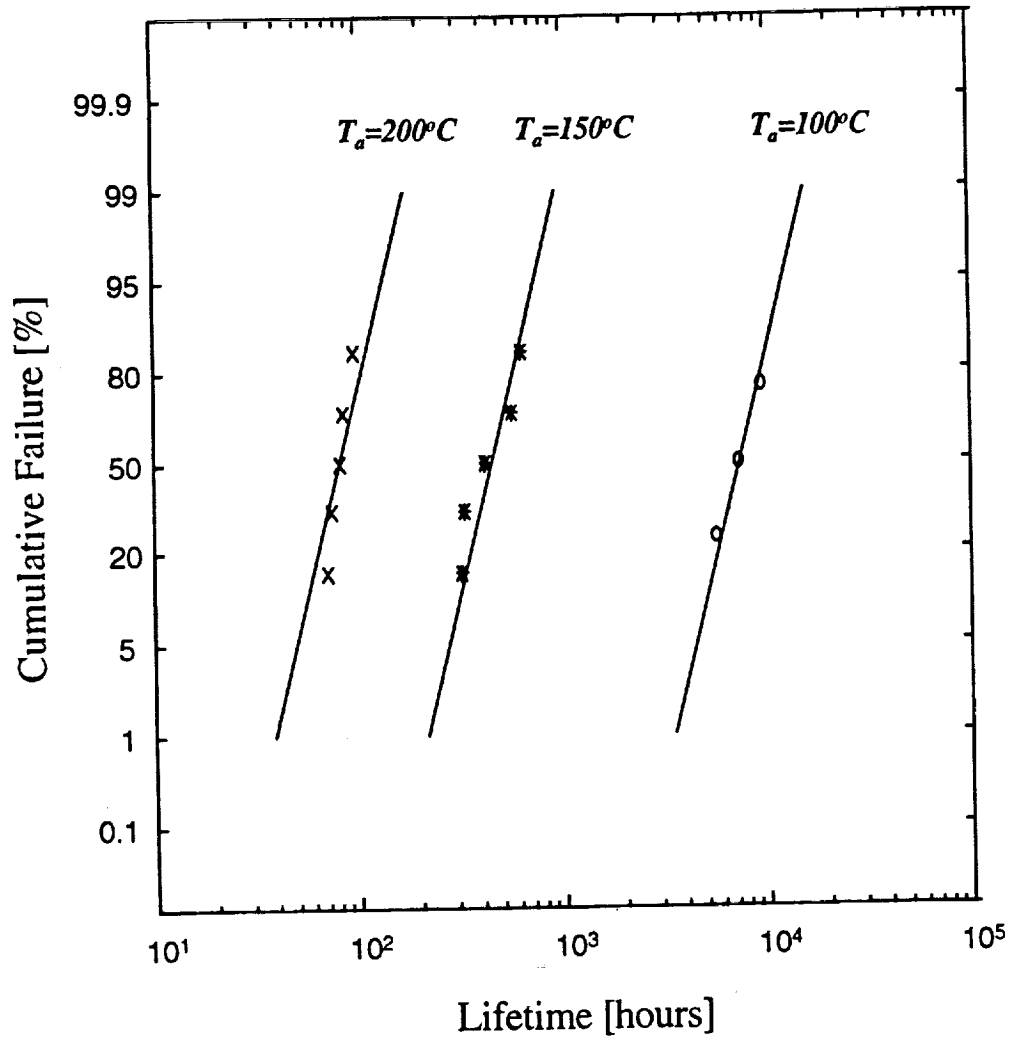
Figure 13. Lognormal projection of time-to-failure versus percent of cumulative failures for undoped APDs after life testing at 100, 150, and 200 degrees C.
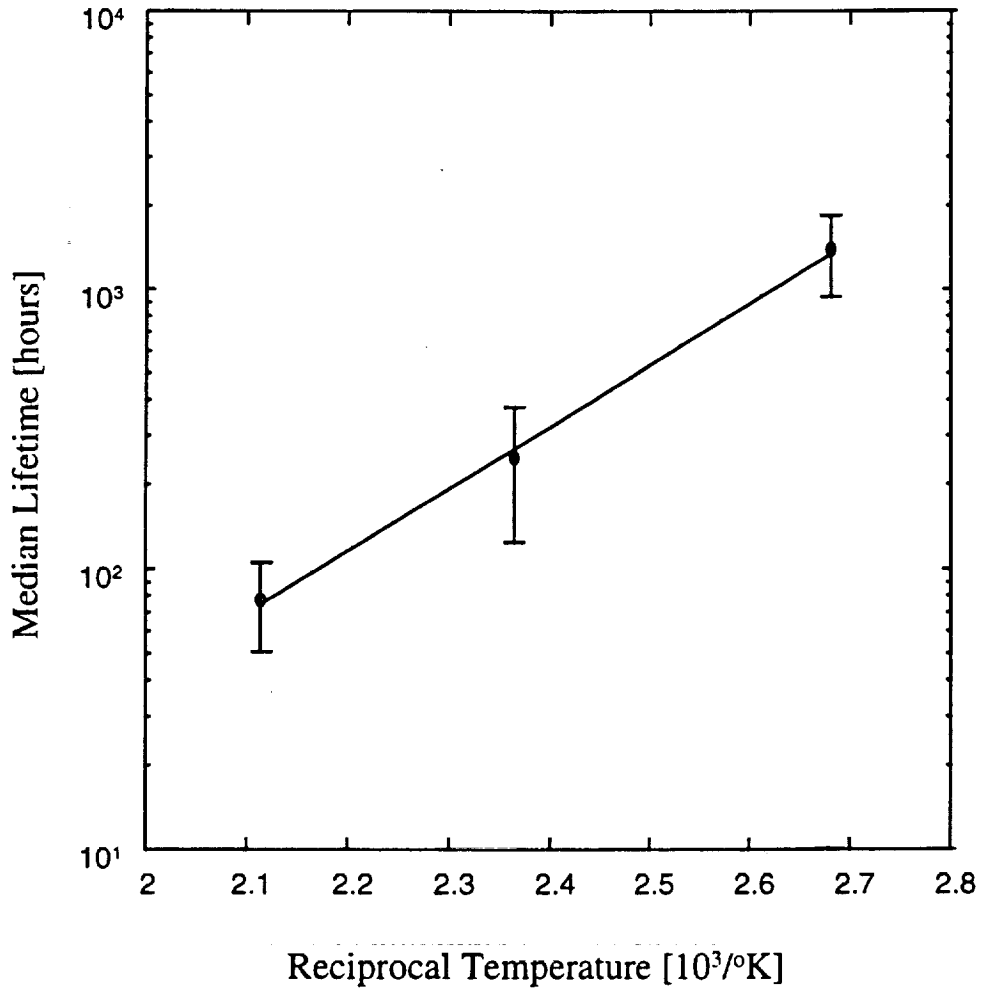
Figure 14. Arrhenius plot of median device lifetime for doped-barrier APDs as a function of reciprocal aging temperature.
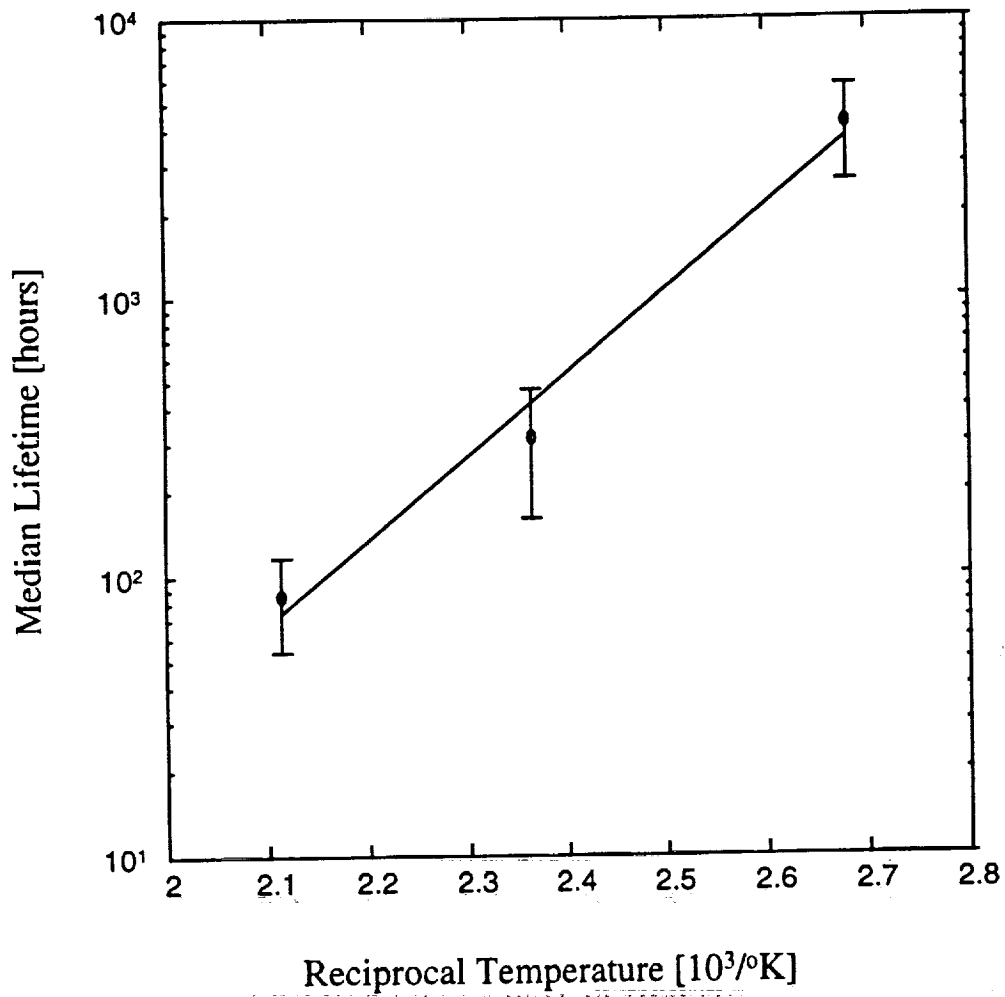
Figure 15. Arrhenius plot of median device lifetime for doped-well APDs as a function of reciprocal aging temperature.
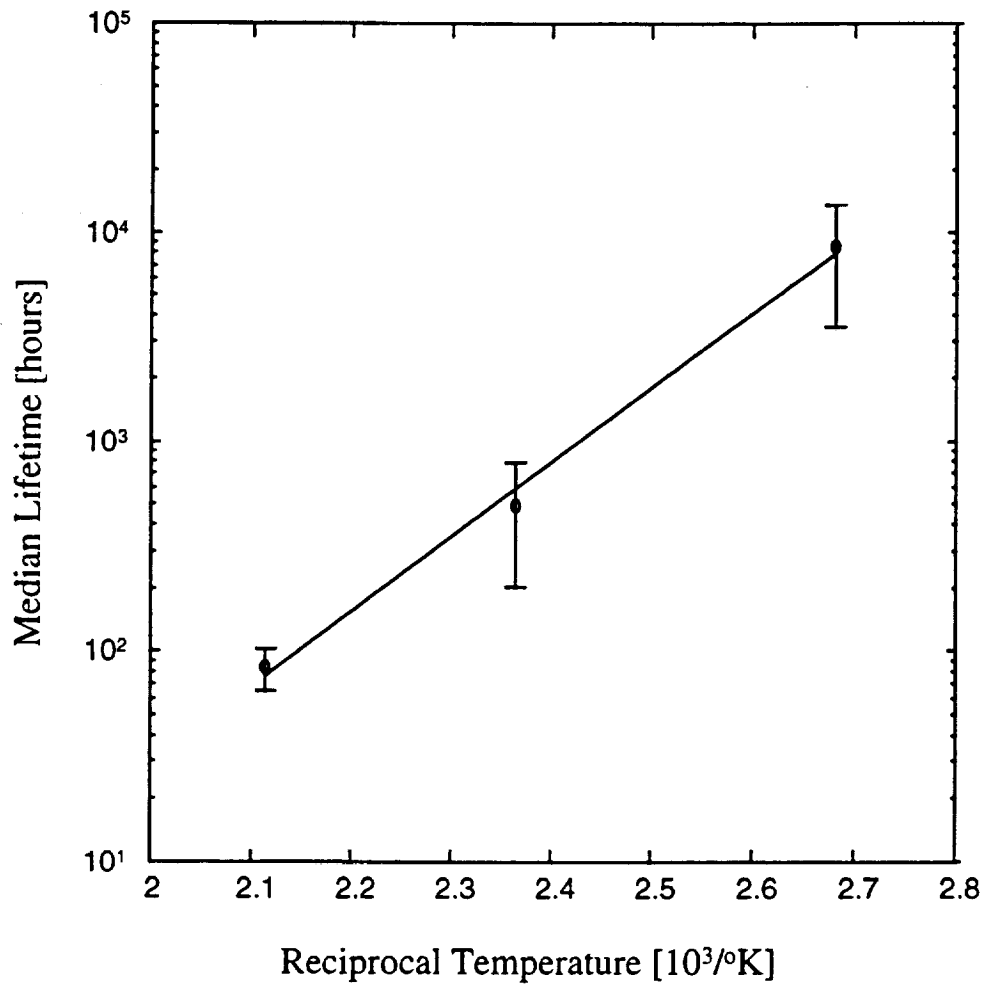
Figure 16. Arrhenius plot of median device lifetime for undoped APDs as a function of reciprocal aging temperature.

It is interesting to note that the doped-well APD, which is a complementary structure of the doped-barrier APD, has a significantly longer median lifetime. A summary of life test results is shown in Table 2.

Table 2. Summary of Life Test Results

Device Type	Activation Energy	Median Lifetime (at 300 °K)	Standard Deviation
Doped-barrier APD	0.44 eV	3.7×10^4 hours	116 hours
Doped-well APD	0.60 eV	3.4×10^5 hours	343 hours
Undoped APD	0.71 eV	1.7×10^6 hours	1031 hours

Due to the lognormal degradation behavior of the APDs, the failure probability of each device as a function of time, P(t), may be computed from the lognormal failure model by using the average device lifetime (μ) and its standard deviation (σ) as [42]:

$$P(t) = \frac{1}{\sigma\sqrt{2\pi}} \int_0^t \frac{1}{t} \exp\left[-\frac{(\ln t - \mu)^2}{2\sigma^2}\right] dt$$

(3.2)

Along with the lognormal plot, this expression provides a quantitative method of evaluating the likelihood of failure for a given device as a function of its age.

3.3 Performance Comparison of APD Structures

Statistical experimental design [38] was used to quantify the impact of each factor on APD reliability and to determine whether the differences between device structures were statistically significant. Due to the mixture of qualitative and quantitative input factors, a D-optimal experimental design with 24 runs was selected to identify the effect of input parameters on the measured responses [43]. The factors investigated in this experiment were device type, diameter of the active area, aging temperature, and stress time. A summary of these input factors is shown in Table 3. Dark current, breakdown voltage, and device lifetime were the measured responses.

Table 3 - Input Factors

Parameter	Values
APD Type	Doped-barrier APD (DB) Doped-well APD (DW) Undoped APD (UND)
Aging Temperature	100-200 °C
Stress Time	50-150 hour
Diameter	75-130 μm

A comparison of the various APD structures in terms of reliability was performed using the analysis of variance (ANOVA) technique. Experimental data was analyzed using the RS/Discover commercial software package [44]. Using this approach, it was verified that the different processes used to fabricate the three APD structures did indeed significantly impact the reliability of the devices. Using the ANOVA technique, the

statistical significance of each input reflects the degree to which the parameter contributes to the variation of the measured responses. If the value of the statistical significance is less than 5%, then the input contribution to the variation of the measured response is considered significant with 95% confidence. Table 4 shows the significance of each factor on the two responses.

Table 4 - Results of D-optimal Experiment

Factor	Statistical Significance		
	Dark Current (I_D)	Breakdown Voltage (V_b)	Device Lifetime (T_D)
Diameter	0.0132	0.0141	0.3151
Temperature	0.0009	0.2192	0.0008
Stress time	0.0013	0.0218	0.4128
APD type	0.2288	0.0001	0.0035

Results indicate that dark-current variation is affected primarily by diameter, temperature, stressing time, and to a lesser degree by the APD type. Breakdown-voltage variation depends on the diameter, stressing time and APD type. Interestingly, the stress temperature did not have a significant effect on the change in breakdown voltage. Finally, the device lifetime is impacted most significantly by stress temperature and APD type.

From these results, it may be concluded that the doping process used in the fabrication of the APD structure has a profound impact on device reliability. Since the undoped devices exhibit the highest degree of reliability, it can be assumed that doping, while enhancing device performance in other ways [23], makes the device less reliable.

Specific causes for the observed differences in device degradation are explored in Section 3.4 below.

3.4 Failure Analysis

3.4.1 SEM and EBIC Analysis

Failure analysis on the thermally stressed doped-barrier, doped-well and undoped devices was carried out using scanning electron microscopy (SEM) and the electron-beam induced current (EBIC) method [39]. Prior to this analysis, the presence of contaminants in passivating nitrides at the junction was hypothesized as a possible cause for dark current increases during stressing.

Figure 17 shows an SEM image of a doped-barrier device prior to accelerated life testing. This image shows no discernible defects. However, defects causing device failure were detected in each type of device after life testing (see Figure 18). Similar results were observed in the doped well and undoped devices. Using EBIC analysis, local defects at the junction region change the electron-beam current indicating the reason for the device failure. Defects near the area of the junction were detected in the EBIC images, and nearly all the SEM images exhibit a similar pattern of defects in the exposed junction area as well. The only exception was the SEM image of an undoped device after life testing, which showed only a small defect in the junction.
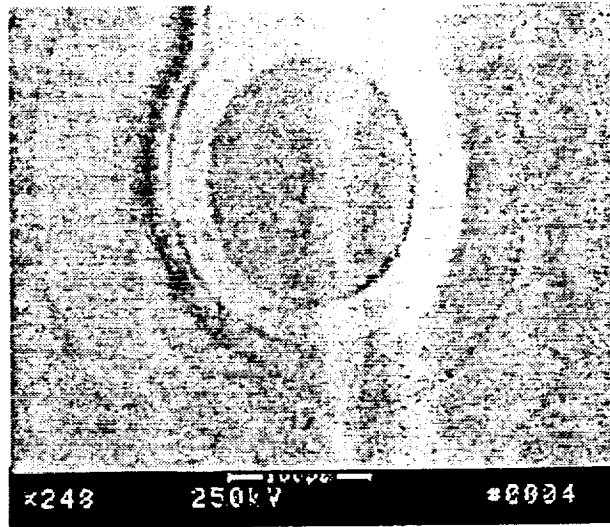
Figure 17. SEM image of GaAs MQW APD before accelerated life testing.

(a) (b)
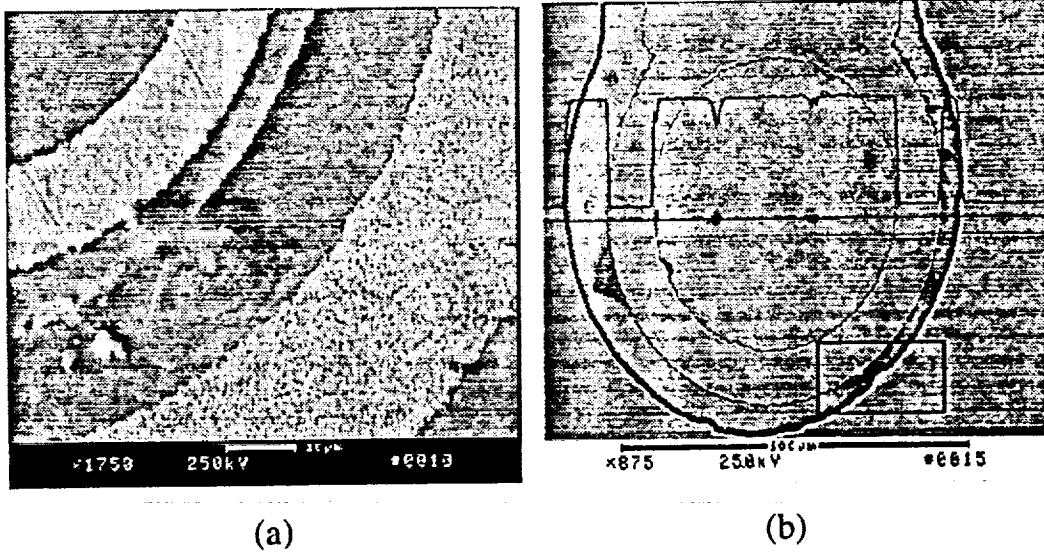
Figure 18. (a) SEM and (b) EBIC images of doped-barrier GaAs MQW APD after
accelerated life testing at 200 degrees C.

3.4.2 EDS Analysis

From SEM and EBIC analysis of the degraded samples, it was determined that the dark current increase could be partially explained by the presence of ionic impurities or contamination in the silicon nitride passivation layer at the junction perimeter. Such contamination generates a leakage path shorting the junction under an electric field. This hypothesis is supported by the fact that unbiased baking of the APD samples resulted in significantly less degradation, which is demonstrated by a comparison of Figures 6 and 7. It has been suggested that these type of defects occur at metal-rich precipitates, some of which occur at crystal dislocations [25-27]. The cause of the gradual reduction in breakdown voltage, on the other hand, is not known explicitly, but presumably involves the field-assisted and/or temperature-assisted drift of some impurity species or defects to localized sites in the pn junction.

A common contaminant for silicon nitride passivating films is ionic sodium. Energy-dispersive spectrometry (EDS) was used to determine whether sodium was the source of contamination in these devices [45]. Using EDS analysis, the composition of a sample and the quantity of each element of a composite material can be obtained. In this case, EDS confirmed the presence of ionic sodium and verified that sodium is the primary contaminant (see Table 5). It is believed that this sodium originated from the APD processing environment or the personnel involved in fabrication. In addition, ionic potassium was detected in the doped-barrier device. (The significant amount of

phosphorus detected in the undoped device was probably due to the etching of the mesa structure).

Table 5 - EDS Results for the Doped-barrier, Doped-well, and Undoped MQW APDs.

Element	Doped-barrier MQW APD	Doped-well MQW APD	Undoped MQW APD
	Weight [%]		
Na	13.68	18.39	14.48
In	-	3.72	1.21
P	4.38	-	21.79
Cl	10.41	-	-
K	11.31	-	-

3.4.3 Dopant Migration Effects

Although ionic contamination is a plausible explanation for device degradation, this effect alone does not account for the statistically significant variations in lifetime among the differently doped APD structures. Since the same passivation process was applied to each structure, one would expect that each would have roughly the same lifetime if contamination were the sole cause of degradation. However, it was observed that the undoped devices were clearly more reliable, followed by the doped well and doped barrier devices, respectively. Therefore, it was theorized that dopant migration might also play a significant role in the device degradation mechanism. This theory was investigated by analyzing dopant migration using capacitance-voltage (C-V) measurements to extract the free carrier concentration in the APD multiple quantum well region before and after

life testing. C-V measurements were performed at 1 MHz using an HP4277A LCZ meter.

For the doped-barrier APD, the free carrier profile in the depletion region is shown in Figure 19. Before life testing, the depletion region width under a reverse bias near the breakdown voltage is approximately 0.195 μm. After life testing, the free carrier concentration significantly increases in the barrier region, and the depletion width decreases to 0.14 μm under reverse bias. Similarly, for the doped-well APD, the free carrier profile before and after life testing appears in Figure 20. Before life testing, the depletion region width under reverse bias is about 0.185 μm. After life testing, the free carrier concentration again increases, and the depletion width shrinks to 0.17 μm.

The free carrier profiles in Figures 19 and 20 are similar to those reported by Aristin et. al. for a doped-barrier MQW APD structure [34]. That paper stated that as the doping concentrations in the barrier increase, dark current increases and breakdown voltage decreases. In the present investigation, the free carrier concentrations increased in doped barrier layers after life testing as well, resulting in comparable increases in dark current.
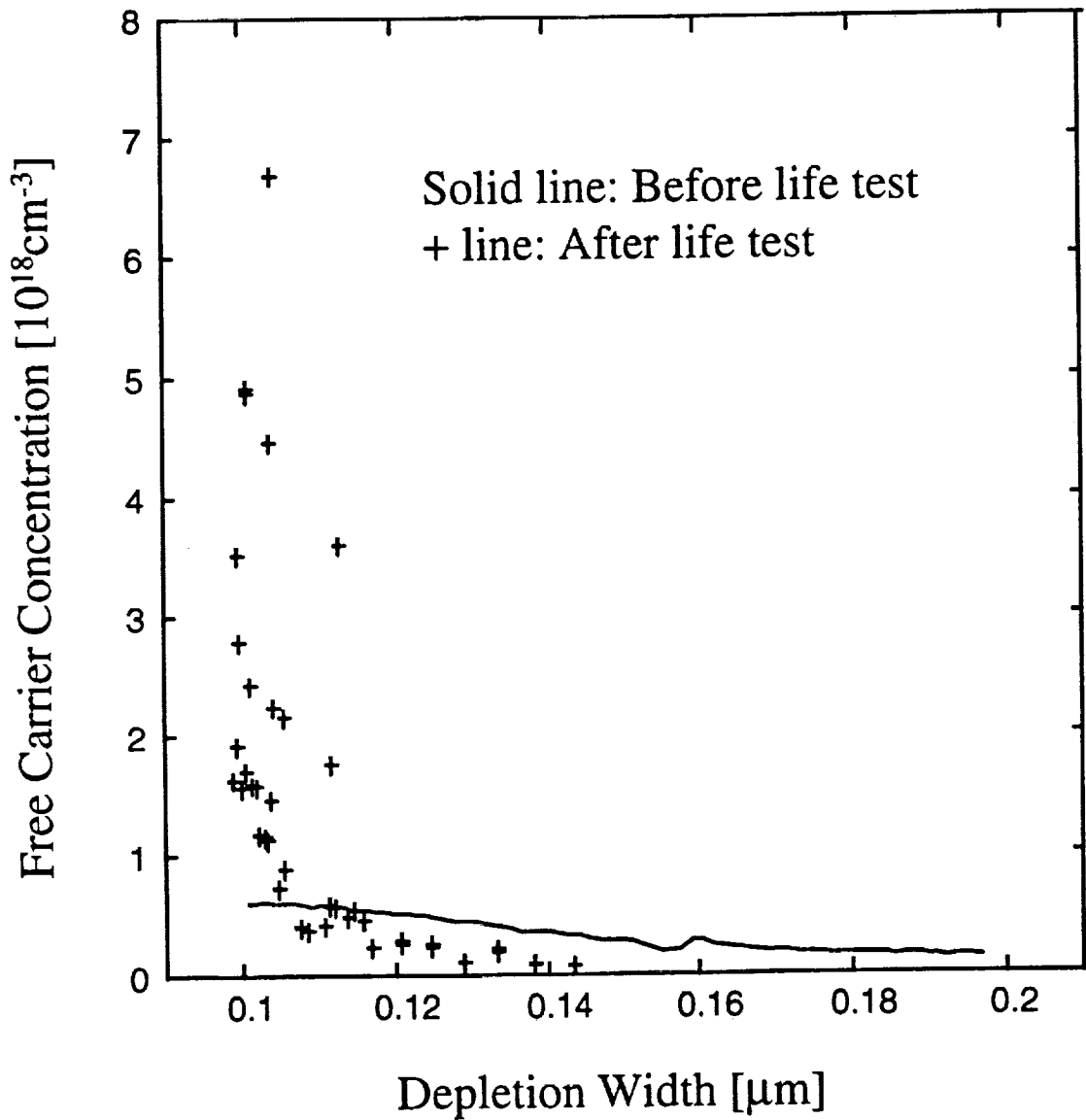
Figure 19. Free carrier concentration profile of doped-barrier APD before and after accelerated life testing.
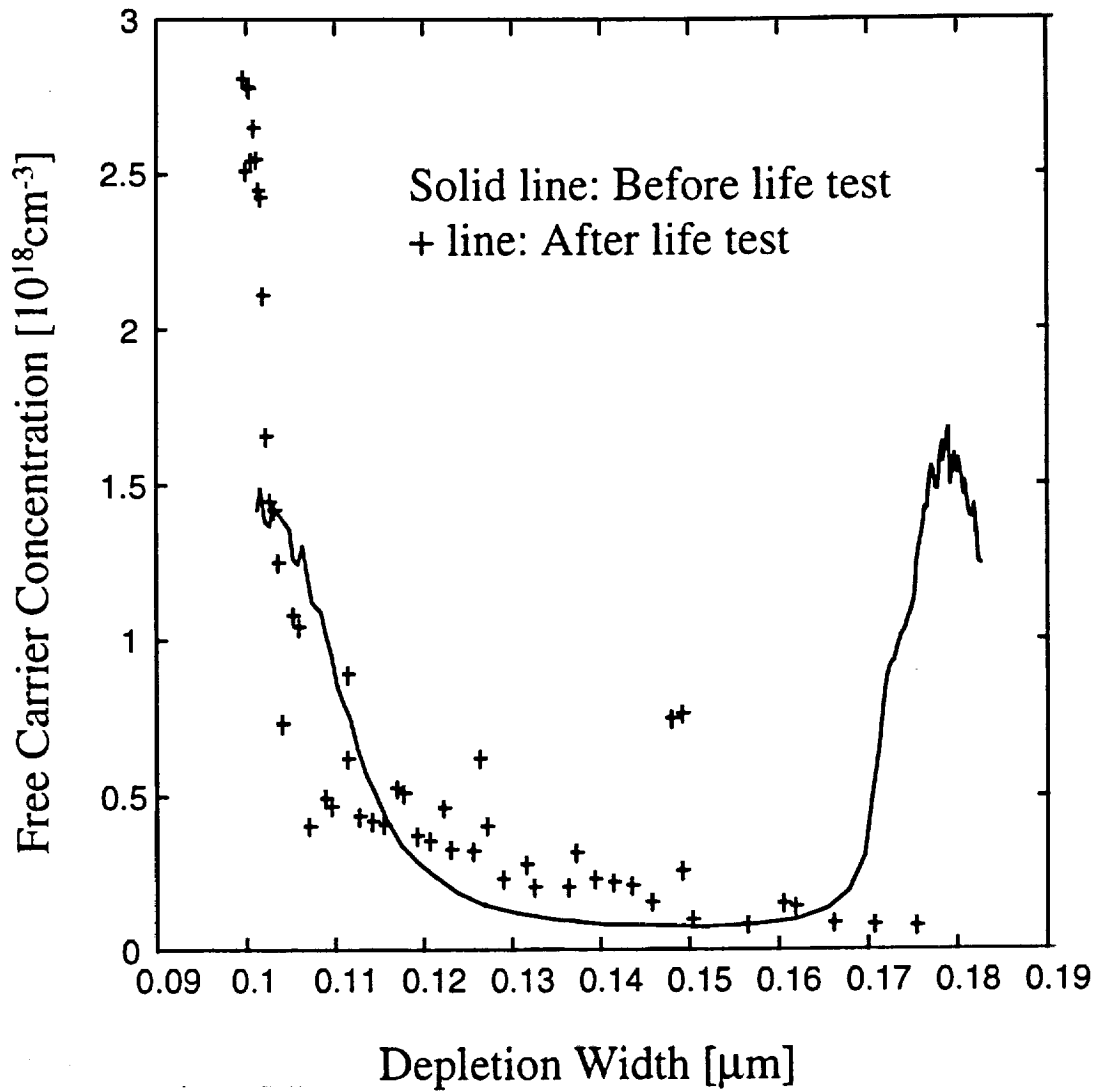
Figure 20. Free carrier concentration profile of doped-well APD before and after accelerated life testing.

From the results of the C-V measurements, it is hypothesized that during the life test, the thermally and electrically excited dopants obtain sufficient energy to migrate into the passivation layer, which causes an increase in free carrier concentration in this region. After entering the passivation layer, these dopants behave similarly to positive surface charges. Because of the accumulation of positive charge, the depletion width is reduced and the electric field in the region where the p-n junction intersects the passivation layer is more intense. Dark current is increased by both the positive charge accumulation as well as the intensified electric field in the narrow depletion region associated with the passivation layer. These increases accelerate the degradation of the device, eventually resulting in failure. The effect is more pronounced in the doped barrier devices since the observed shrinkage in the depletion region width is greater in these devices than in the doped well APD.

3.5 Summary

This chapter has presented accelerated life tests of doped-barrier, doped-well, and undoped AlGaAs/GaAs multiple quantum well avalanche photodiodes from the viewpoint of evaluating long-term reliability. From the life test results, the activation energy of the degradation mechanism and median lifetime of these devices was determined. In addition, the failure probability of the devices was computed from the log-normal failure model by using the average lifetime and the standard deviation of that lifetime as parameters.

Using the ANOVA technique, a comparison of the reliability of the various APD structures was undertaken. Based on this investigation, it was concluded that the doping process used in the multiple quantum well APD fabrication has a significant effect on device reliability. It was found that the undoped APD structure yielded devices that exhibited the highest reliability, followed by the doped well and doped barrier devices, respectively.

Subsequent failure analysis using the SEM and EBIC methods clarified that the dark current increase was in part brought about by the presence of ionic contaminants in the passivation layer at the junction perimeter that generate a leakage path which shorts the junction under the effect of electric field. EDS analysis identified the primary contaminant as ionic sodium. In addition, dopant migration under stress was theorized as a means to explain the observed reliability differences between the device structures. This dopant migration was investigated using C-V measurements, which verified that the redistribution of free carriers after stress is indeed a plausible explanation for reliability differences.

Even though reliability modeling establishes a mapping between processing parameters and a performance metric (APD device lifetime), only limited measured data can be obtained from the long lifetime measurements. Therefore, in the next chapter, an effort to use simulated data as a supplement of experimental data will be described for investigating the effect of manufacturing parameters on performance metrics.

CHAPTER 4

DEVICE SIMULATION

4.1 Introduction

The life testing and reliability modeling effort described in the previous chapter represents a first step in deriving a quantitative mapping between device parameters and APD lifetime. However, the number of APD samples measured was restricted, and they had very limited variation in device diameter and barrier width. Furthermore, the exact doping profiles for APD devices were not available. The objective of the APD simulation effort outlined in this chapter is to use simulated data as a supplemental aid to experimental data for understanding the effect of variations in manufacturing parameters on lifetime, as well as on other measures of device performance such as gain and noise.

4.2 ATLAS Device Simulator

Accurate device simulation requires that measured data first be sufficiently calibrated with the simulation tool. Simulation of APD operation was performed using the ATLAS II device simulation package [46]. This tool is very useful for simulating compound semiconductor devices such as photodiodes. ATLAS II is powerful enough

that even the multiple quantum well structure can be accurately simulated. It provides a comprehensive set of models and fully integrated features. For multiple quantum well APD simulation, two major sub-modules, BLAZE and LUMINOUS, are required [46].

BLAZE is a general simulation tool for heterojunction devices. This module accounts for the effect of position-dependent band structure by modification to the current approximations in a drift-diffusion model. Therefore, BLAZE can be applied to a broad range of device applications including heterojunction photodetectors (APDs, solar cells, etc.), heterojunction diodes, high electron mobility transistors (HEMTs), and light-emitting diodes (LEDs). LUMINOUS is a tool for calculating intensity profiles within the semiconductor device that are translated into photogeneration rates in the device simulator. Simulated electronic response to optical signals for a broad range of photodetectors can be obtained by this module. Hence, LUMINOUS can supply the capabilities required to simulate the performance of optoelectronic devices.

The electrical properties of semiconductor device junctions can be expressed by Poisson's equation (Equation 4.1) as well as the continuity equations for both electrons and holes (Equation 4.2a and 4.2b) as follows [35]:

$$\nabla \cdot (\nabla \psi) = -\frac{q}{\varepsilon_s}\left(p_p - n_p + N_D^+ - N_A^-\right) \tag{4.1}$$

$$\frac{\partial n}{\partial t} = G_n - U_n + \frac{1}{q}\nabla \cdot J_n \qquad\qquad (4.2a)$$

$$\frac{\partial p}{\partial t} = G_p - U_p - \frac{1}{q}\nabla \cdot J_p \qquad\qquad (4.2b)$$

where ψ is the intrinsic Fermi potential, N_D^+ and N_A^- represent the donor and acceptor ionized impurity concentrations, G_n and G_p are the electron and hole generation rate, respectively, and U_n and U_p are the electron and hole recombination rate, respectively.

In the ATLAS II simulations, Newton's two-carrier method is used for solving Poisson's and the continuity equations. Newton's method is very effective when the system of equation is strongly coupled. The program can find numerical solutions to the equations by calculating the values of unknown variables on a pre-determined mesh points within the device structure. The original continuous model is converted to a discrete non-linear model which is an approximation of the original model. This discrete model can be solved by an iterative procedure after an initial guess. The iterative process continues until the result meets certain convergence criteria, or until it does not converge for a certain number of iterations. The initial guess for the variables to be evaluated is important to achieve convergence. During the bias ramp procedure in I-V and C-V calculations, the initial guess for any bias point is obtained by the extrapolation of the two previous results. This method will generally provide good results when the variables to be measured have linear characteristics. However, problems can occur when the

variables behaves nonlinearly such as is the case with current near breakdown or threshold. This will normally require repeated simulations to determine the threshold point at which the voltage steps must be reduced to obtain convergence.

In these simulations, the avalanche multiplication process caused by impact ionization is the most important process during the junction breakdown. Under the effect of an electric field, a incident carrier (electron or hole) acquires sufficient energy to produce an electron-hole pair (EHP). These new produced carriers are accelerated by the field and can acquire high-energy themselves, creating more electron-hole pairs. If insufficient energy was obtained, impact ionization does not occur, and the obtained energy is usually dissipated by heat. In addition, carriers can lose energy by non-ionizing scattering mechanism before obtaining sufficient energy for impact ionization process. The scattering rate can be different for electrons and holes. The impact ionization process is modeled according to the Selberherr model [47]. The generation rate of electron-hole pairs due to impact ionization can be expressed as follows:

$$G = \alpha_n \cdot \frac{|J_n|}{q} + \alpha_p \cdot \frac{|J_p|}{q} \qquad (4.3)$$

where α_n and α_p are the electron and hole ionization rates, respectively. These ionization rates are expressed as a function of electric field as:

$$\alpha_n = \alpha_n^\infty \cdot \exp\left[-\left(\frac{E_n^{crit}}{E}\right)^{\beta_n}\right] \qquad (4.4a)$$

$$\alpha_p = \alpha_p^\infty \cdot \exp\left[-\left(\frac{E_p^{crit}}{E}\right)^{\beta_p}\right] \qquad (4.4b)$$

where E is the electric field component in the current flow direction. All other impact ionization parameters are dependent on the material.

In addition, carriers are accelerated by the local electric field, but release some momentum due to various scattering mechanisms in the junction region. These scattering events can be caused by impurities, lattice vibrations, and other material imperfections. The scattering mechanism can impact the low-field mobilities, which are functions of the local electric field, the lattice temperature and the local doping concentrations, etc. At low electric field, when the doping concentration increases, impurity scattering increases which causes mobility to decrease. For high electric field, the mobility decreases because carriers with high energy will actively participate in scattering process. The mobility models used in ATLAS simulations are both doping-dependent and field-dependent.

Light I-V characteristics are modeled using a $1mW/cm^2$ monochromatic light source operating at 800 nm. From this simulation tool, dark current (I_D), photo current (I_L), and impact ionization rates for electrons (a) and holes (b) can be calculated. The multiplication gain is given by [35]:

$$M(V) = \frac{I_L(V) - I_D(V)}{I_{LO}} \qquad (4.5)$$

where $I_L(V)$ is photocurrent at the applied bias voltage V, $I_D(V)$ is dark current at the applied bias voltage V, and I_{LO} is the photocurrent at unity gain. The impact ionization rate ratio (k) for electron injection defined by [35]:

$$k = \frac{\alpha_p}{\alpha_n} \qquad (4.6)$$

where α_n and α_p are the electron and hole ionization rate, respectively.

In order to simplify the models and to reduce program execution time, the following assumptions were made regarding the simulated structures:

1) All devices have a rectangular geometric configuration.

2) Only SRH and Auger recombination is considered (Optical and surface recombinations are ignored).

3) The p and n contacts are assumed to be perfect ohmic contacts.

4) Doping imbalances in the MQWs are constant throughout the entire structure.

5) The effect of bandgap narrowing in AlGaAs is similar to that in GaAs.

4.3 Comparison between Simulation and Experimental Results

Figure 21 shows that the results of the ATLAS II simulation for a 10-period, doped-well MQW APD. The simulated gain vs. breakdown voltage curve matched the experimental data quite well, indicating that device characterization can be performed using data simulated by ATLAS II as a supplement to experimental data.
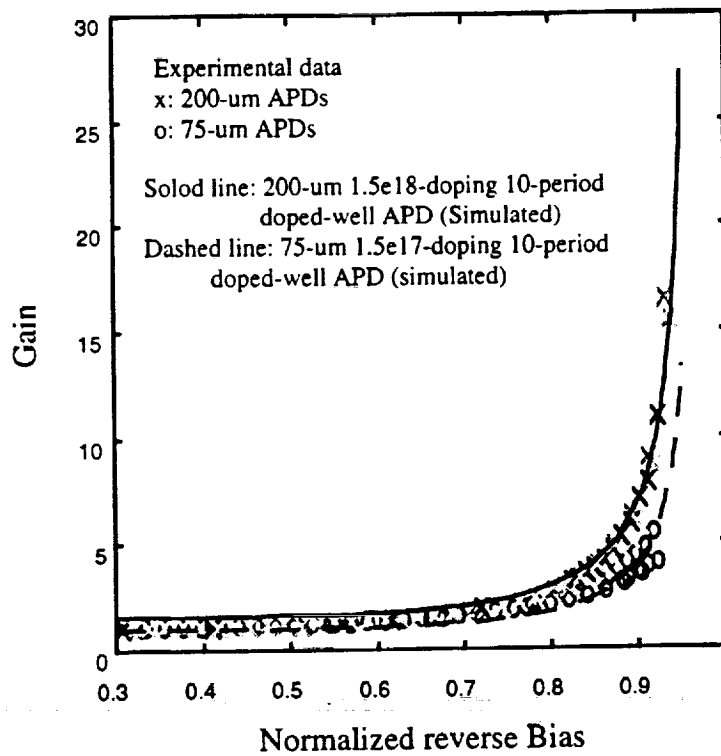
Figure 21 - Experimental & Simulated results of gain vs. breakdown voltage curve for 10-period, doped-well MQW APDs

4.4 Summary

In this chapter, the ATLAS II device simulation framework was described. . It provides a comprehensive set of models useful for simulating simulate the heterojunction III-V compound optoelectronic devices such as photodiodes. It was shown that properly calibrated ATLAS II simulations can be a useful supplement to experimental data in device characterization. In the next chapter, using the data sets generated from ATLAS II device simulator, neural network models which map manufacturing parameters such as device active diameter, barrier width, and doping profile, to device performance metrics (gain, noise, and APD lifetime) will be derived.

CHAPTER 5

DEVICE MODELING USING NEURAL NETWORKS

5.1 Introduction

The ATLAS II simulations described in the previous chapter have been used to generate data sets from which to build neural network models which map the variations in device diameter, doping, and barrier width to device performance. For both gain and noise index, neural network modeling can be accomplished by a direct approach using the results obtained from the ATLAS simulator. Several simulations can be performed using a systematic experimental design to achieve sufficient coverage of the input parameter space, and the results of these simulations can be used to train a neural network to model gain and noise index as a function of the process parameters (see Section 5.3 below).

However, no device simulator presently exists from which similar information regarding the variation of device reliability and lifetime can be extracted. In addition, although extensive lifetime measurements have been performed on MQW APD samples, the devices measured had very limited variation in active diameter and barrier width, and exact doping profiles for these devices are not available. Therefore, in order to extract

and model the variation of device lifetime with these parameters, a less direct approach is required. Specifically, the lifetime model has been extracted by establishing two cascaded sequential mappings (see Figure 22). First, the manufacturing parameters are varied in a designed experiment, and ATLAS is used to model the pre-stress values of the dark current and breakdown voltage of the device for each combination of parameters. Subsequently, the pre-stress dark current and breakdown voltage are used as indicators of device lifetime. These pre-stress dark current and breakdown voltage values are then mapped to device lifetime, again using a neural network. This network is trained to model this relationship using the measured lifetime data obtained in Chapter 3.
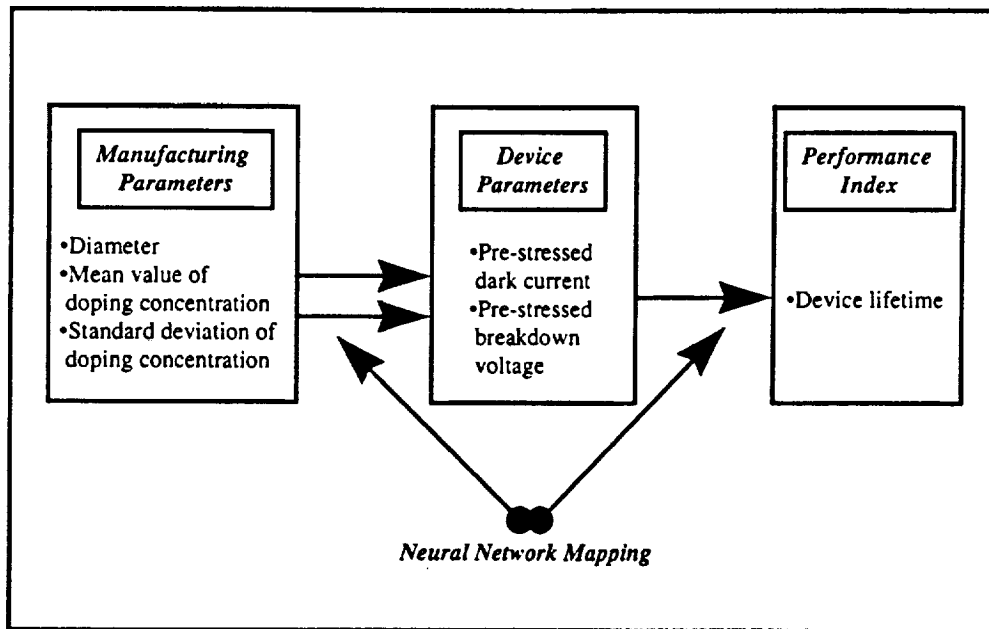
Figure 22 - Scheme used to model device lifetime as a function of manufacturing process parameters.

5.2 Experimental Design

Using ATLAS II simulations, designed experiments were performed to obtain the data necessary to construct neural network models of APD gain, noise, pre-stress dark current, and pre-stress breakdown voltage as a function of device diameter, barrier width, and the mean and standard deviation of the barrier (or well) doping. Gain, noise, and lifetime were the key factors used in this investigation to quantify MQW APD performance. However, as has been previously stated, although gain and noise can be simulated directly using ATLAS II, lifetime cannot. Therefore, the designed experiment is used to characterize the pre-stress values of dark current and breakdown voltage.

The gain index (G) is defined herein as the area under the plot of gain versus reverse bias up to the breakdown voltage. The noise index (N) is defined by the electron-to-hole impact ionization rate ratio which is closely related to the excess noise factor of MQW APDs. The pre-stress dark current is defined as the dark current of a device measured prior to life testing at 90% of its breakdown voltage. The pre-stress breakdown voltage is defined as the breakdown voltage of the device measured prior to life testing from its I-V curve using the tangent line method.

Table 6 - Input Factors for the gain and noise characterization

Parameter	Values
Active Diameter	75-130 μm
Barrier Width	200-800 Å
The Mean doping	10^{17}-10^{18} cm^{-3}
The Standard deviation of doping	(0.1-2) 10^{17} cm^{-3}

The four input factors varied in the gain and noise characterization simulations and their respective ranges of variation are shown in Table 6. The ranges were selected to account for the variety of potential operating conditions used in device fabrication. Only three input factors (diameter, and the mean and standard deviation of barrier or well doping) were varied in the pre-stress dark current and breakdown voltage characterization simulations. Their respective ranges of variation are the same as those shown in Table 7.

Table 7 - Input Factors for the device lifetime characterization

Parameter	Values
Active Diameter	75-130 μm
The Mean doping	10^{17}-10^{18} cm^{-3}
The Standard deviation of doping	(0.1-2) 10^{17} cm^{-3}

Among the many available approaches for statistical experimental design, the D-optimal design technique was selected for this set of experiments. D-optimal designs give flexibility in designing experiments not provided by classical designs (such as factorial designs). They are typically used to select a specified number of runs from a predetermined design space. The number of runs are selected in such a way as to minimize variances in subsequently estimated model coefficients [48]. In addition, the number of experiments can be adjusted according to the experimental budget or schedule. The D-optimal design matrix for the gain and noise characterization simulations appears in Table 8(a), and the design matrix for pre-stress dark current and breakdown voltage characterization is shown in Table 8(b).

Table 8(a) - The design matrix for the gain and noise characterization

Run	1 DIAMETER [μm]	2 BARRIER_WIDTH [Å]	3 DOP_MEAN [10e17cm-3]	4 DOP_STD [10e17cm-3]
1	130	800	10	2
2	75	200	5	1
3	200	500	1	2
4	130	800	1	1
5	130	500	5	0.1
6	75	800	1	2
7	75	200	10	2
8	75	800	1	0.1
9	75	800	5	0.1
10	75	800	10	0.1
11	200	200	1	0.1
12	130	200	10	2
13	200	200	10	0.1
14	75	500	1	0.1
15	130	200	10	0.1
16	130	200	1	1
17	200	200	1	2
18	75	500	5	2
19	75	200	10	0.1
20	200	800	5	2
21	200	200	5	1
22	200	800	10	0.1
23	200	800	1	2
24	200	200	10	2
25	75	200	1	2
26	75	800	10	2
27	75	200	1	0.1
28	200	800	10	2
29	200	800	1	0.1
30	200	500	10	1
31	75	500	10	1

Table 8(b) - The design matrix for the pre-stress dark current and breakdown voltage
characterization

Run	Diameter	Mean_doping	Std_doping
	[μm]	[10e17cm-3]	[10e17cm-3]
1	130	1	1
2	100	5	0.1
3	75	1	0.1
4	130	1	2
5	130	10	0.1
6	100	1	2
7	130	5	1
8	100	10	1
9	75	10	0.1
10	130	10	2
11	75	5	1
12	100	10	1
13	100	1	0.1
14	100	5	2
15	130	10	2
16	75	1	1
17	130	5	0.1
18	75	10	0.1
19	130	5	2
20	130	1	0.1
21	75	1	2
22	130	1	2
23	75	1	0.1
24	75	10	2
25	130	10	0.1
26	75	1	2
27	75	10	2

5.3 Neural Network Modeling

Neural networks possess the capability of learning complex relationships between groups of related parameters [49]. Such learning capabilities are attributed to the fact that neural networks, possessing many simple parallel processing units (called "neurons"), crudely resemble the architecture of the human brain. Neurons in a network are interconnected in such a way that knowledge is stored in the weight of the connections between them.

The most popular method of training feed-forward neural networks is the error back propagation (BP) algorithm. This algorithm has been shown to be every effective in learning arbitrary nonlinear mappings between noisy sets of input and output vectors. BP networks consist of several layers of neurons which receive, process, and transmit critical information regarding the relationships between the input parameters and corresponding responses (see Figure 23). Each neuron contains the weighted sum of its inputs filtered by a nonlinear sigmoidal transfer function. These networks incorporate "hidden" layers of neurons which do not interact with the outside world, but assist in performing classification and feature extraction tasks on information provided by the input and output layers.
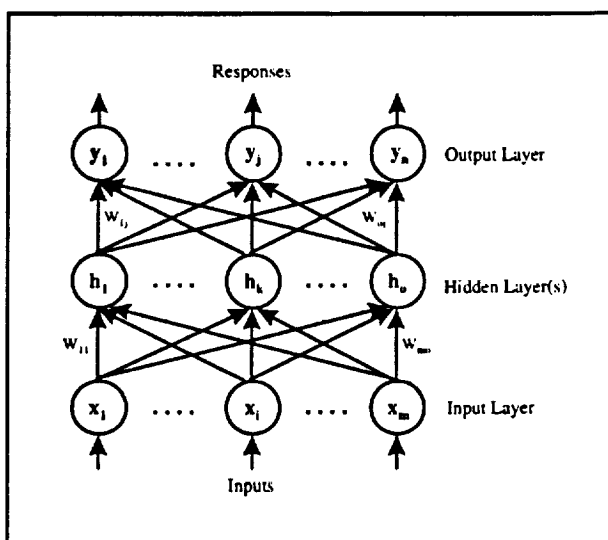
Figure 23- Typical feed-forward error back propagation neural network.

Inputs to the gain, noise and pre-stress dark current and breakdown voltage neural network models include device active diameter, barrier width, the mean value of the doping concentration, and the standard deviation of doping concentration. A separate network is used to map the pre-stress dark current and breakdown voltage (inputs) to the device lifetime (output). The manufacturing parameters are mapped to device lifetime using both networks in a cascaded fashion (see Figure 22 above). Back-propagation neural networks have been used to build models of each response.

5.3.1 Gain and Noise Modeling

The neural network models for gain and noise index described in Section 5.2 were established from 31 ATLAS II simulation runs from the D-optimal experimental design.

A three-layer neural network with four inputs, five hidden neurons, and two outputs was used. The network was trained using ObOrNNS ("Object-Oriented Neural Network Simulator), a C++ program developed by the Intelligent Semiconductor Manufacturing group here at Georgia Tech. Table 9 provides an overview of the network structural and learning parameters, and Figure 24 shows a comparison between training error and prediction for the gain and noise models were 0.619 and 0.057, respectively, and the prediction errors were 0.779 and 0.017, respectively.

Table 9: Neural Network Parameters for Gain and Noise Models

Response	Architecture	Learning rate	Momentum
Gain	4-5-1	0.01	0
Noise	4-5-1	0.01	0
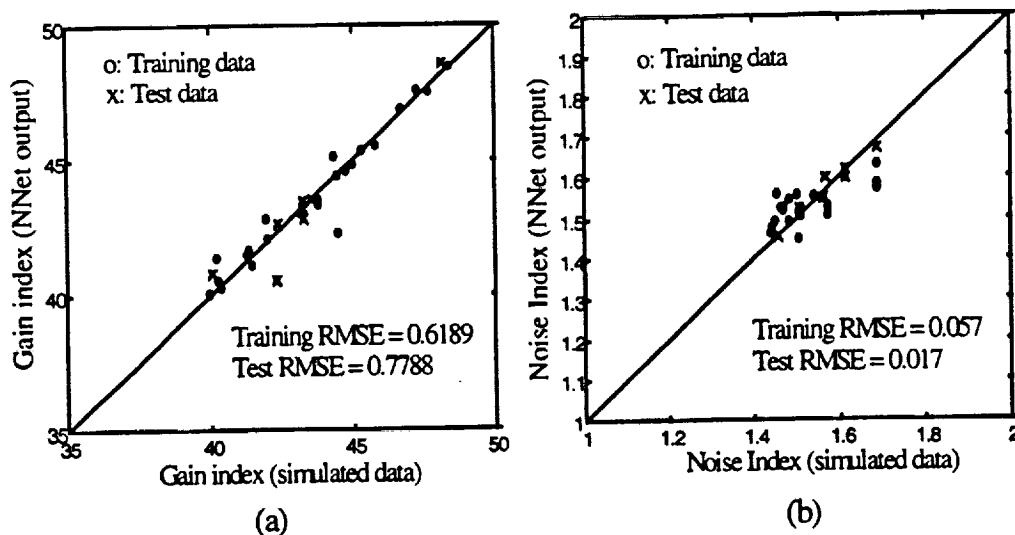
Figure 24 - Neural network modeling results for: (a) Gain index; (b) Noise index.

Based on the results of the neural network modeling, the effect of the various manufacturing parameters on gain and noise index can be quantitatively investigated. Figure 25 shows 3-D contour plots of gain and noise index versus an active diameter and the mean value of doping concentration. In each case, barrier width and the standard deviation of doping concentration remain constant at their mid-range value. Here it is evident that increasing the mean doping concentration results in higher gain. In addition, increasing the active diameter of the APD along with the mean doping concentration results in a higher noise index. These results occur partly due to the fact that increasing the doping concentration can cause more carrier multiplication during the avalanche process, which can increase impact ionization rate ratio (k). As k increases, both the gain and noise index increase as well. These results are in agreement with experimental measurements performed by P. Aristin, et. al. for similarly structured AlGaAs/GaAs MQW APDs [23].
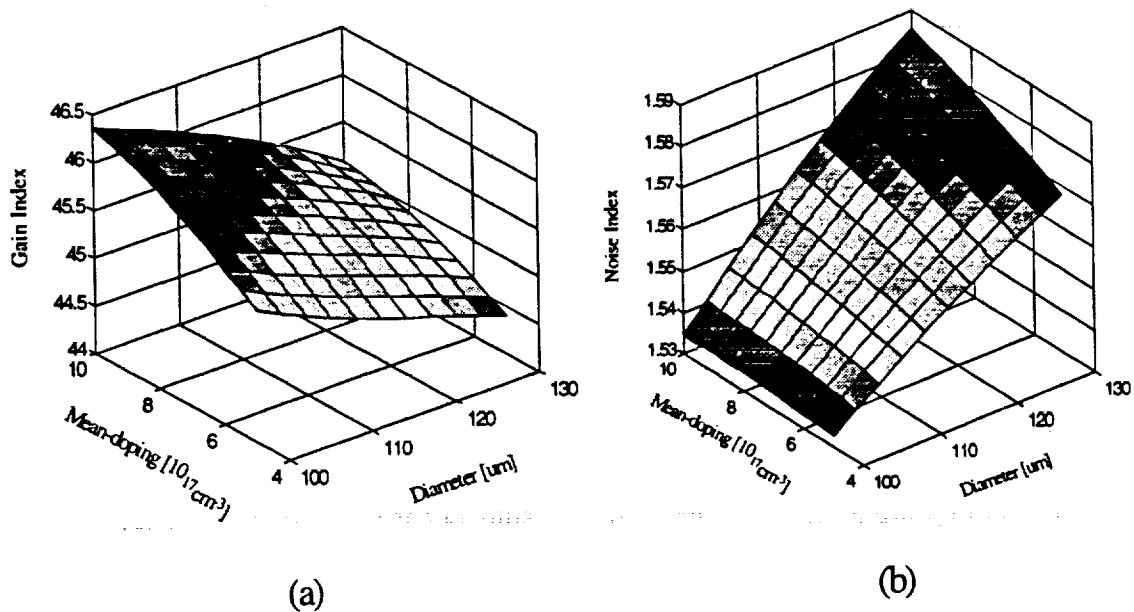
Figure 25 - Contour plots of neural network models of: (a) gain index; and (b) noise index as a function of mean doping concentration and device diameter. Barrier width and doping standard deviation are set to their mid-range values.

In addition to the above models, "inverse" neural network models are also needed for calculating the parametric yield using the procedure described in Section 3.6. The description of the parameters for the inverse neural network models is provided in Table 10. Note that in order to achieve a one-to-one mapping between device outputs and process inputs, two "dummy" device output variables are required for the inverse models. These dummy variables are not directly involved in parametric yield calculations, but are necessary to derive a proper Jacobian determinant [8]. The training and prediction results for the inverse models are shown in Figure 26.

Table 10: Neural Network Parameters for Gain and Noise Inverse Models

Response	Architecture	Learning rate	Momentum
Active Diameter	4-7-1	0.001	0.0005
Barrier Width	4-7-1	0.003	0.001
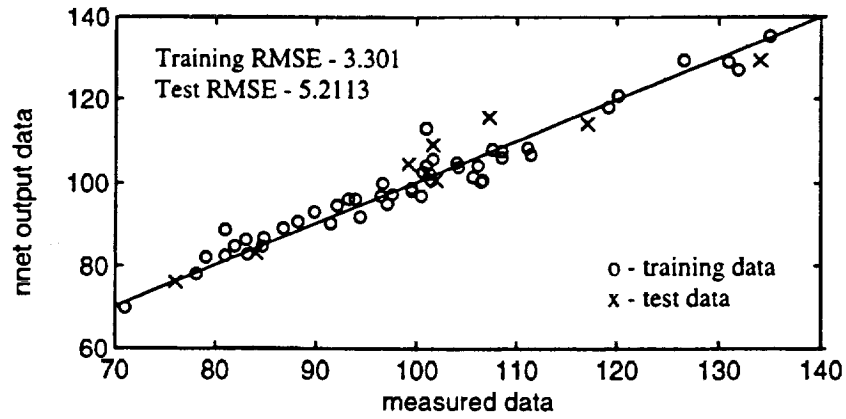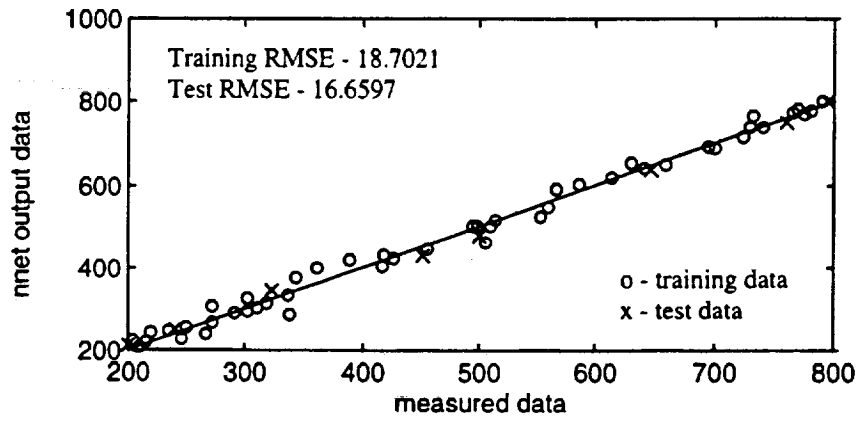
Figure 26 - Gain and Noise Inverse neural network modeling results for: (a) active diameter; (b) barrier width.

71

5.3.2 Device Lifetime Modeling

The neural network models of device lifetime for doped-barrier and doped-well MQW APDs described in Section 5.2 were established from two cascaded models. The first model constructed from 27 ATLAS II simulation runs from the D-optimal experimental design. A three-layer neural network with three inputs (diameter, mean doping, and standard deviation of doping), seven hidden neurons, and two outputs (pre-stress dark current and pre-stress breakdown voltage) was used and trained using ObOrNNS. The second model evaluated using the measurement data from life testing. A three-layer neural network with 2 inputs, three hidden neurons, and one outputs was used.

Table 11: Neural Network Parameters of Device lifetime Models

The first model			
Response	Architecture	Learning rate	Momentum
Pre-stress dark current	3-7-1	0.002	0.001
Pre-stress breakdown voltage	3-7-1	0.002	0.001
The second model			
Response	Architecture	Learning rate	Momentum
Device Lifetime	2-3-1	0.01	0.005

Table 11 provides an overview of the network structural and learning parameters, and Figure 27 shows a neural network modeling results for doped-barrier APDs. It was found that the training error for the pre-stress dark current, pre-stress breakdown voltage, and device lifetime models were 0.0316, 3.3578, and 25.4, respectively, and the prediction errors were 0.0228, 2.0921, and 17.8, respectively. Figure 28 shows a neural

72

network modeling results for doped-well APDs. It was found that the training error for the pre-stress dark current, pre-stress breakdown voltage, and device lifetime models were 0.0420, 2.2316, and 36.3871, respectively, and the prediction errors were 0.0839, 3.0852, and 65.5723, respectively. The results of neural network modeling for the doped-barrier and the doped-well APDs are summarized in Table 12.

Table 12: Neural Network Parameters for device lifetime Models

Doped-barrier APD model			
	Pre-stress dark current	Pre-stress breakdown voltage	Device lifetime
Training Error	0.0316	3.3578	25.4
Prediction Error	0.0228	2.0921	17.8
Doped-well APD model			
	Pre-stress dark current	Pre-stress breakdown voltage	Device lifetime
Training Error	0.0420	2.2316	36.3871
Prediction Error	0.0839	3.0852	65.5723
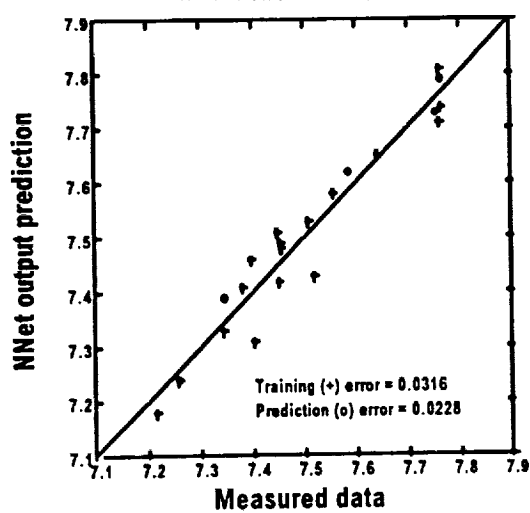
(1) Pre-stress breakdown voltage
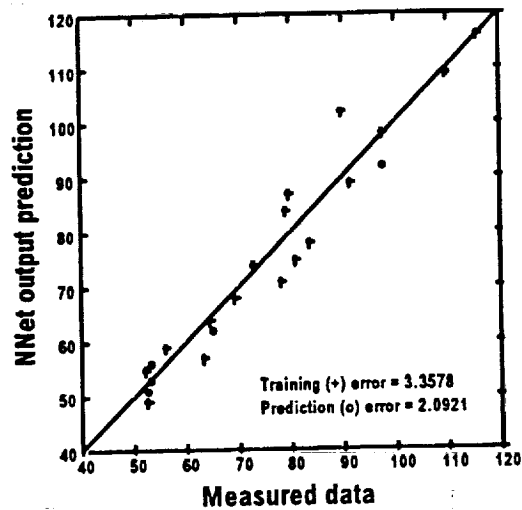
(2) Pre-stress dark current

(a) Pre-stress dark current and breakdown voltage
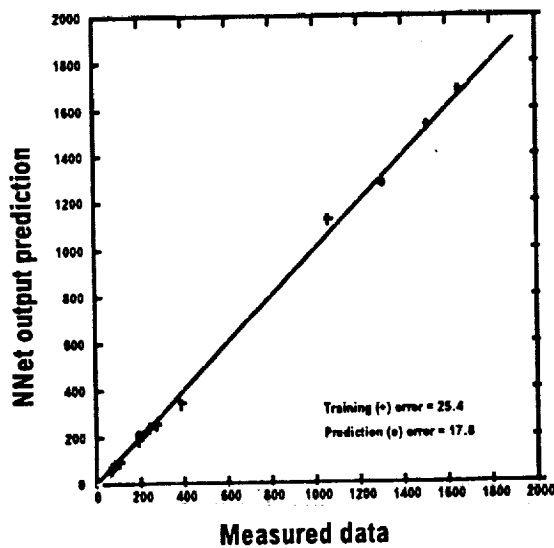
(b) Lifetime

Figure 27 - Device Lifetime Neural Network Modeling Results for Doped-barrier APDs: (a) Pre-stress dark current and breakdown voltage model; (b) lifetime model.
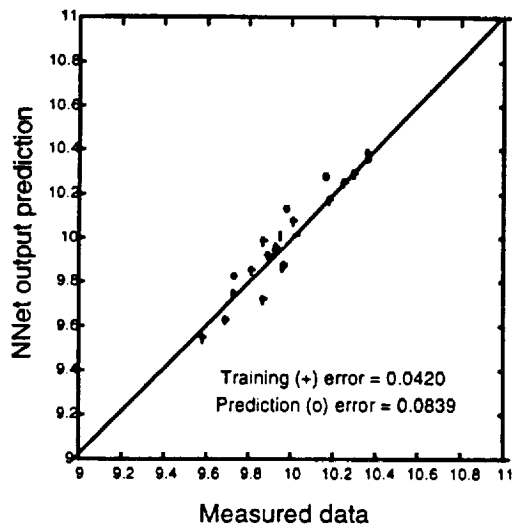
(1) Pre-stress breakdown voltage
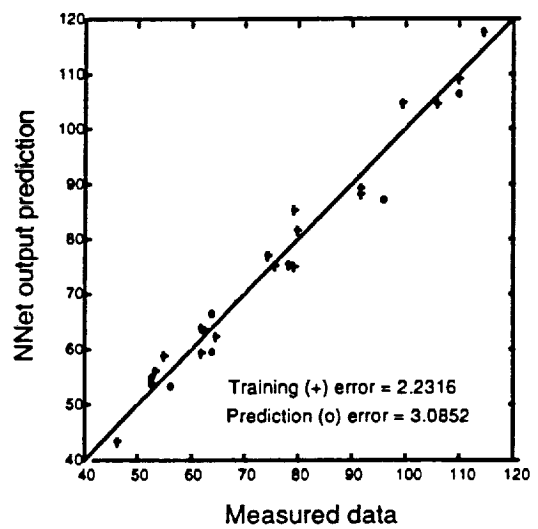
(2) Pre-stress dark current

(a) Pre-stress dark current and breakdown voltage
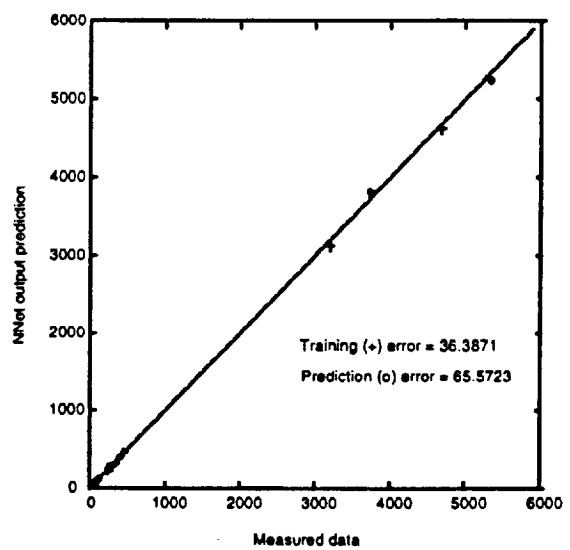
(b) Lifetime

Figure 28 - Device Lifetime Neural Network Modeling Results for Doped-well APDs: (a) Pre-stress dark current and breakdown voltage model; (b) lifetime model.

In addition to the above models, "inverse" neural network models are also needed for calculating the parametric yield using the procedure described in Chapter 6. The description of the parameters for the inverse neural network models is provided in Table 13. Note that in order to achieve a one-to-one mapping between device outputs and process inputs, two "dummy" device output variables are required for the inverse models. The training and prediction results for the inverse models of doped-barrier APDs and doped-well APDs for three different temperature models are shown in Figure 29 and Figure 30, respectively.

Table 13: Neural Network Parameters for device lifetime Inverse Models

Doped-barrier APD model			
Response	Architecture	Learning rate	Momentum
Device Diameter	3-9-7-1	0.001	0.0005
Doped-well APD model			
Response	Architecture	Learning rate	Momentum
Device Diameter	3-9-7-1	0.0005	0.0005
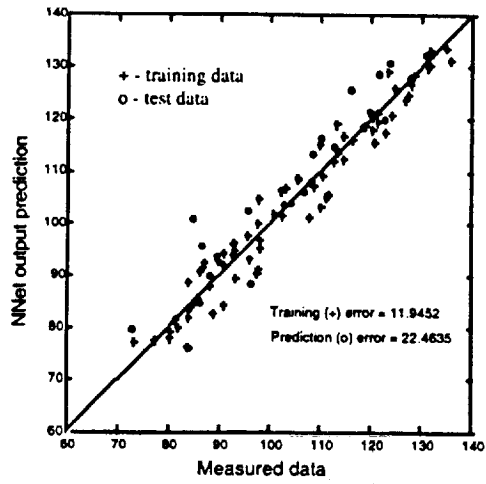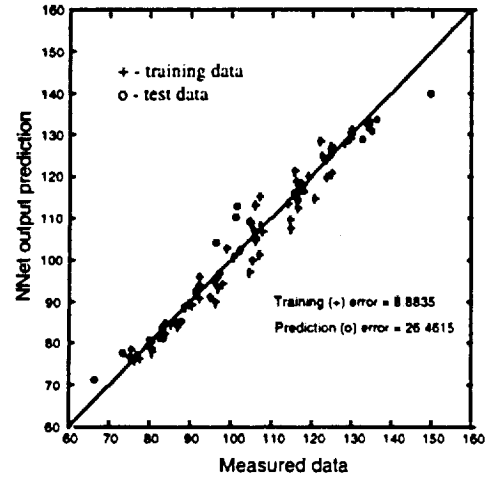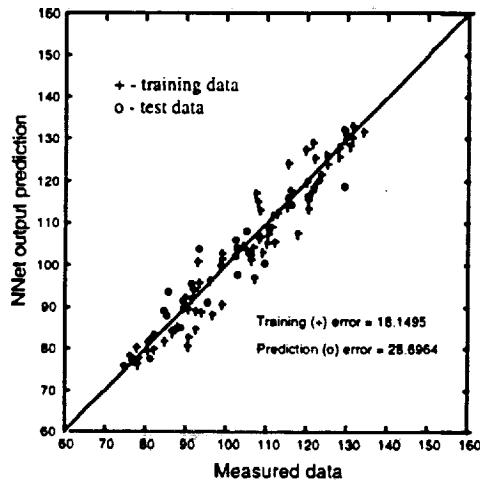
Figure 29 - Lifetime Inverse Neural Network Modeling Results of diameter for doped-barrier APDs.
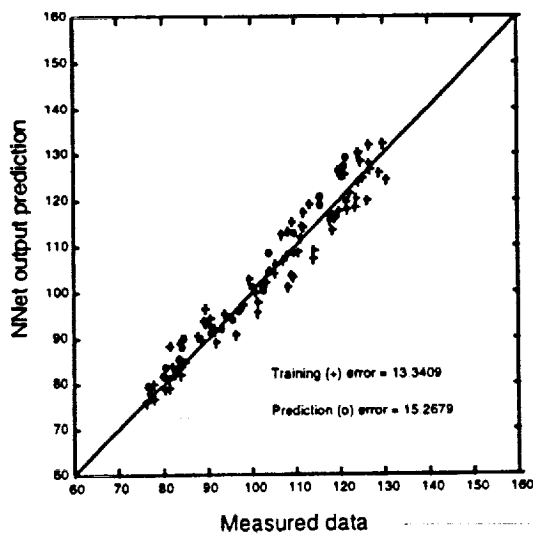
(a)
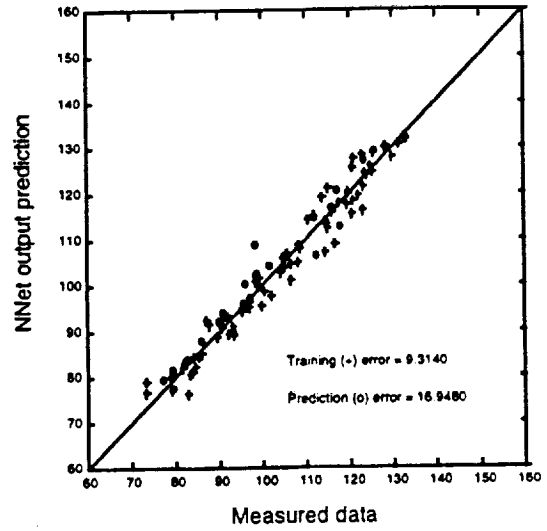
(b)
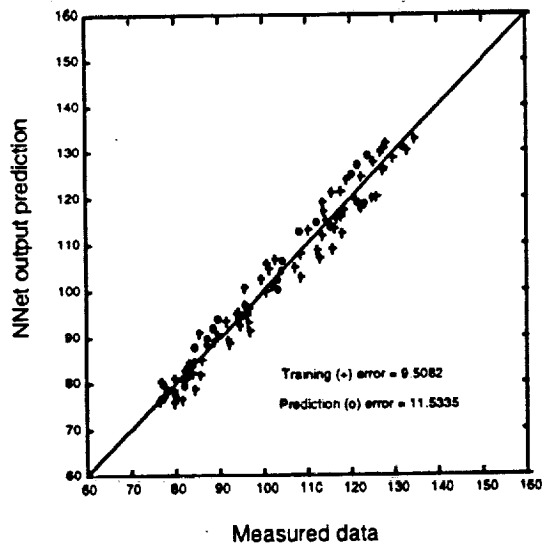
(c)

Figure 30 - Lifetime Inverse Neural Network Modeling Results of diameter for doped-well APDs.

5.4 Sensitivity Analysis

Sensitivity analysis is useful to analyze the response of the neural network models derived above. The sensitivity of one input value with respect to the other inputs is found by calculating the normalized partial derivative of that response with respect to the input of interest while maintaining the other input variables as constants [50]. If f is a function of two input variables, x_1 and x_2, and a response $y = f(x_1, x_2)$, then the sensitivity of x_1 is given by [51]:

$$S(f, x_1) \cong \left. \frac{\left| f(x_1 + \Delta x_1, x_2) - f(x_1, x_2) \right|}{\Delta x_1} \right|_{\Delta x_1 \to 0} \cdot \frac{x_1}{\left| f(x_1, x_2) \right|} \qquad (5.1)$$

where f is the functional relationship encoded in the neural network model, dx_1 is an incremental perturbation of x_1, and $x_1/f(x_1, x_2)$ is a normalization factor. For neural network process models, sensitivity analysis consists of using a specific vector of the inputs and making incremental changes to one input of interest. All other input variables remain constant. The first (unperturbed) vector is then used to calculate the neural network output by trained neural network model. The sensitivity is simply the ratio of the difference between the network output for the initial input vector and the perturbed input vector to the increment multiplied by the normalization factor. The results of sensitivity analysis are used to determine which input factors have the relatively more impact on the particular response.

5.4.1 Gain and Noise Modeling

Using the methodology described above, sensitivity analysis for gain and noise index was also performed. The sensitivity of each parameter was defined in terms of a 10% deviation from nominal (or mid-range) values. The results of the sensitivity analysis showing the relative influence on gain and noise index of each process parameter is shown in Figure 31. It can be seen that the gain index is impacted primarily by the active diameter and the barrier-width. The noise index is impacted most by active diameter, barrier-width, and the mean value of the doping concentration. The standard deviation of the doping concentration has almost no effect on the noise index.

(a)   (b)
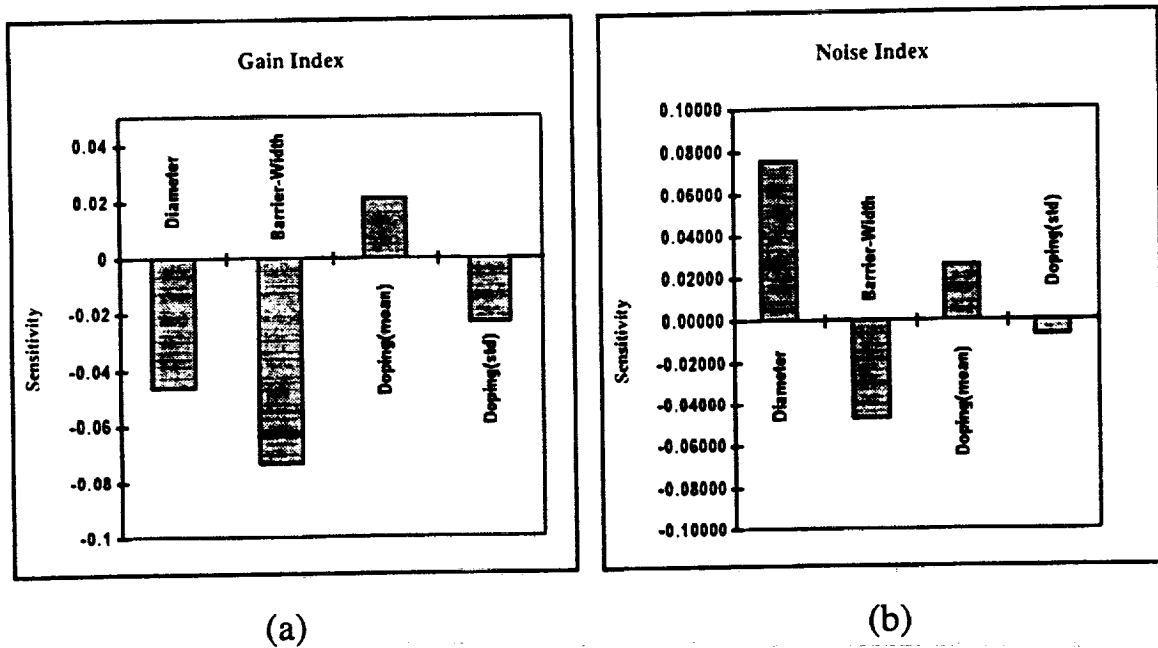
Figure 31 - Results of sensitivity analysis for: (a) Gain index; (b) Noise index.

5.4.2 Device Lifetime Modeling

Sensitivity analysis of device lifetime for both doped-barrier and doped-well MQW APDs was also illustrated. Three lifetime models for each case were evaluated. The sensitivity of each parameter was defined in terms of a 5% deviation from nominal (or mid-range) values. From the results shown in Figure 32, it can be seen that the device lifetime for both the doped-barrier and doped-well models is negatively impacted by the active diameter and the mean value of doping concentration. It was also found that the lifetime of the doped-well MQW APD is more sensitive than the doped-barrier MQW APD. The standard deviation of the doping concentration has almost no impact in both cases.

(a)   (b)
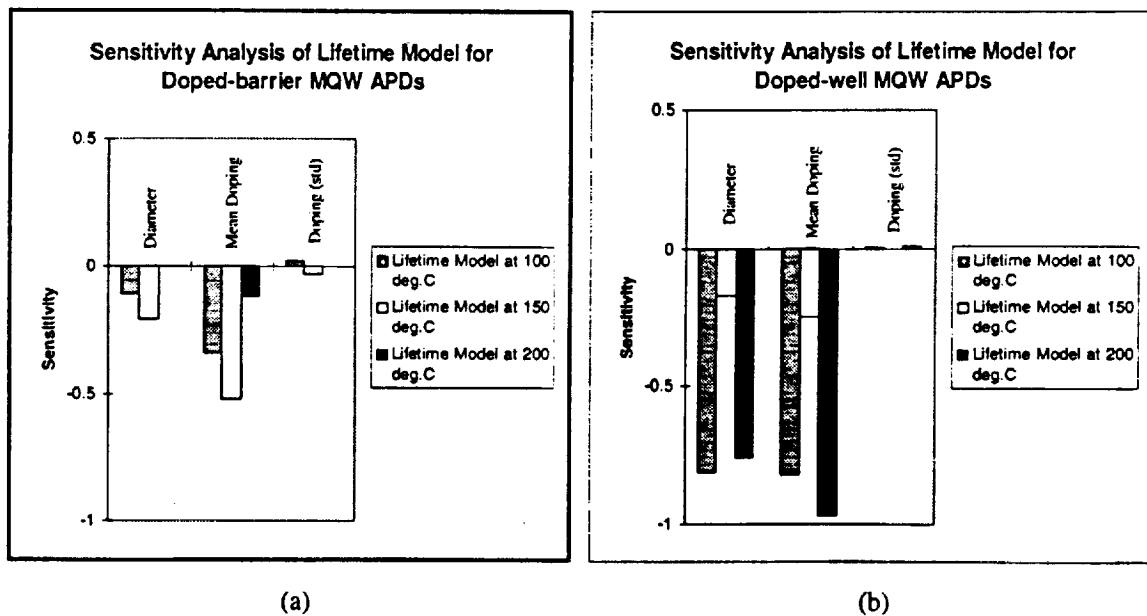
Figure 32 - Results of sensitivity analysis for: (a) Doped-barrier APDs; (b) Doped-well APDs.

5.5 Summary

In this chapter, neural network models for gain, noise, and device lifetime were evaluated from ATLAS II device simulation runs from the D-optimal experimental design. In addition, sensitivity analysis of these models was also performed to analyze the response of the neural network models. It was found that these results are good in agreement with experimental measurements and previously established physical trends. In the next chapter, parametric yield prediction of each performance metric (gain, noise, and device lifetime) will be accomplished using these neural network models.

CHAPTER 6

STATISTICAL PREDICTION OF PARAMETRIC PERFORMANCE OF GaAs MQW APDs

6.1 Introduction

In this chapter, a systematic methodology for modeling the parametric performance of GaAs MQW APDs is presented. The approach described first requires a model to be developed which reflects the probability distribution of each of the relevant process variables. This model can be obtained directly from measured process data. A second model is then required to account for the correlation between this measured process data and device performance metrics. This can be derived either from the evaluation of analytical expressions relating process variables to performance or through device simulation. The availability of the above models enables the computation of the joint probability density function required for predicting performance using the Jacobian transformation method [8], which converts the process variable distributions to the device performance metric distributions. The resulting density function can then be numerically integrated to determine parametric yield. Since they have demonstrated the capability of highly accurate function approximation for mapping complex, nonlinear data sets, neural networks have been used for generating the models described above [52].

This methodology will provide device designers with the ability to understand the manufacturability of various design options, and will enable process engineers to extrapolate the consequences of process modifications by processing a relatively small set of test structures. These capabilities will ultimately allow device yield prediction prior to high-volume manufacturing in order to evaluate the impact of both design decisions and process capability. In the applying this methodology to the MQW APDs, it is shown herein that using a small number of test devices with varying active diameters, barrier and well widths, and doping concentrations enables accurate prediction of the expected performance variation of APD gain and noise in larger populations of devices.

6.2 Statistical Variation of Manufacturing Parameters

For MQW APDs fabrication, a few of the relevant parameters which may vary in a typical manufacturing process include the active diameter (A), barrier width (B), the mean value of doping concentration (M) and its standard deviation (S). Usually, it is assumed that these manufacturing parameters will vary according to the normal distribution. However, this may not always be the case in reality [53]. Several commonly occurring distributions in semiconductor device fabrication are shown in Figure 33. These deviations from the ideal Gaussian shape regularly appear in IC fabrication.
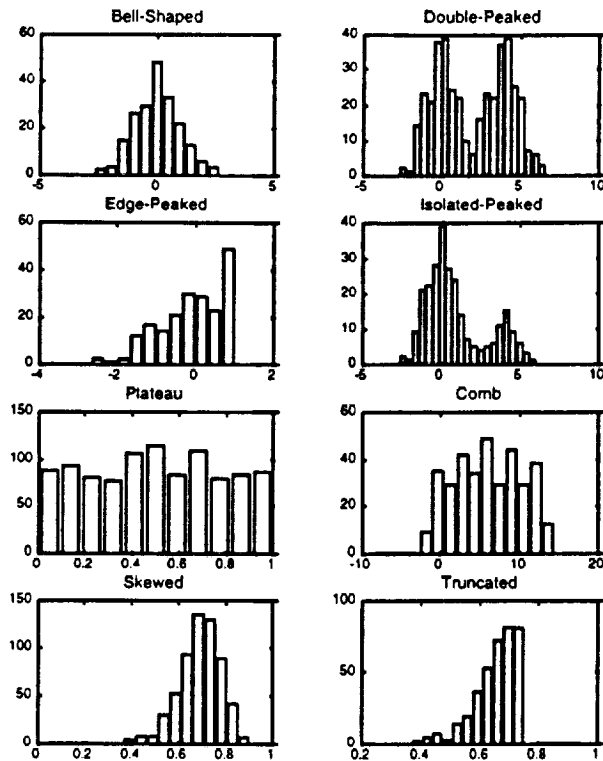
Figure 33 - Commonly occurring distributions in semiconductor device fabrication.

The bell-shaped distribution is the standard normal distribution. Skewed, truncated, and edge-peaked distributions are asymmetric distributions which typically occur when a process specification limit exists on one side and is relatively close to the nominal value. Double-peaked and isolation-peaked distributions are bimodal patterns suggesting the presence of two overlapping Gaussian processes, resulting in a valley in the middle of range of data. The plateau distribution is a flat-topped pattern, such as the uniform distribution, indicating multiple process conditions affecting the distribution which have not yet to be sufficiently isolated. The comb distribution is consists of regularly

alternating high and low values of the probability density function caused by measurement errors, rounding errors, or errors in the method of grouping the data. It is important to consider each of these as possible distributions in APD fabrication in order to accurately characterize fluctuations in parametric yield.

6.3 Generating Joint Density Functions of Process Variables

The histograms described in Section 6.2 provide models of marginal probability density functions (pdfs) for each device parameters. Since the random variables of the discrete type is investigated as device parameters, these marginal pdfs are related to the joint probability density function for all parameters as follows [8]:

$$f_1(x_1) = \int ... \int f(x_1, x_2, ..., x_n) dx_n ... dx_2 \approx \sum_{x_2} \cdots \sum_{x_n} f(x_1, x_2, ..., x_n) \qquad (6.1)$$

where $f_1(x_1)$ is the marginal pdf for parameter x_1 and $f(x_1, x_2, ..., x_n)$ is the joint pdf for n different device parameters. In the present work, the random variables x_i's are the manufacturing parameters A, B, M, and S.

As an example, consider the joint pdf for two random variables. Multiple integrals of the joint pdf using Equation (6.1) provide probability information along several dimensions in the same way that integrating a marginal pdf gives the probability of finding a single variable in given interval (see Figure 34).
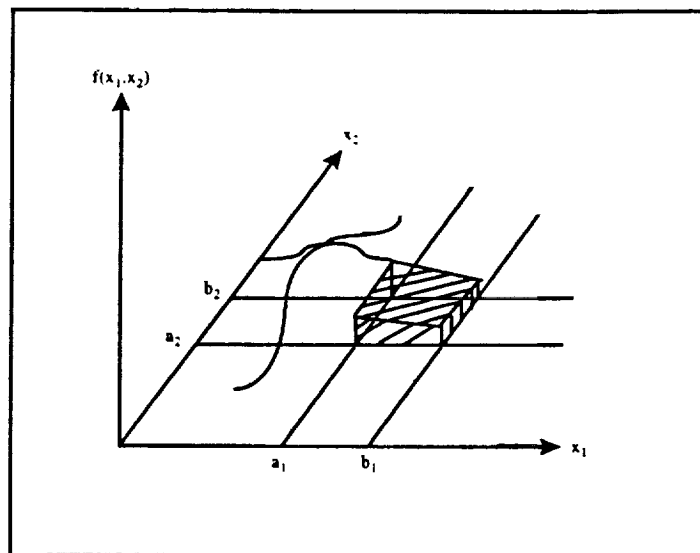
Figure 34 - A joint density function of two variables. The probability of finding x_1 is between a_1 and b_1 and simultaneously finding x_2 is between a_2 and b_2 is given by the shaded volume.

The joint pdf can be found by determining the relative frequency of device performance along several dimensions. This can be accomplished by partitioning the device parameter space into divisions with appropriate granularity, counting the number of devices in each category, and dividing by total number of devices measured (The last step insures that joint pdf is normalized). To illustrate this process, consider Table 14, which describes a hypothetical bivariate distribution of barrier width and mean doping for a population of devices. When tabular histograms such as this are properly normalized, the resulting data can be plotted to give a surface (such as in Figure 25) which approximates the form of the joint pdf. This procedure can be extended to as many

dimensions as desired, and the resulting hypersurface likewise approximates the multidimensional joint pdf.

Table 14 - Hypothetical Bivariate Histogram for Barrier Width and Diameter
Barrier Width [10^{-10} m]

		200-320	320-440	440-560	560-680	680-800
	71-82	26	24	24	20	26
	82-93	195	180	180	150	195
Diameter [um]	93-104	299	276	276	230	299
	104-115	182	168	168	140	182
	115-126	78	72	72	60	78

Since the exact form of the manufacturing parameter distributions is difficult to predict, the usual assumption of normal behavior may be inadequate. In order to circumvent this difficulty, neural networks are again proposed as a mechanism to encode the functional form of the overall joint parameter distribution directly from measured (or simulated) data. BP networks can be readily used to learn the mapping between manufacturing parameter values (inputs) and their corresponding relative frequency (output). In this way, the joint parameter density function will be encoded in the network. The validity of this approach has recently been demonstrated by Gibson and et. al. in [54], where it was shown that BP neural networks can successfully model both normal and non-normal pdfs. In fact, for the non-normal case, it was shown that neural nets modeled

the underlying distribution with significantly greater accuracy than can be achieved using traditional multinormal statistics.

6.4 Generating Joint Density Function of Device Parameters

Once the joint pdf of the device parameters has been computed, the next step is to derive the joint pdf for functions of these parameters. For example, if the joint pdf of active diameter (A) and barrier-width (B) is known, we would like to use this information to calculate the joint pdf of device performance characteristics such as gain index (G) or noise index (N), since each of these performance measures are functions of A and B. Often, we will be interested in functions of several manufacturing parameters, but for the sake of simplicity, we will consider only two. Let us consider two sets of random variables X_i (representing the manufacturing parameters) and Y_i (representing the performance metrics), where the Y_i's are functions of the X_i's:

$$x_1 = A; x_2 = B; y_1 = G; y_2 = N \tag{6.2}$$

The functional relationship between the manufacturing process variables and performance metrics can be expressed as:

$$\begin{aligned} y_1 &= H_1(x_1, x_2) \\ y_2 &= H_2(x_1, x_2) \end{aligned} \tag{6.3}$$

where H_1 and H_2 are continuous, differentiable functions.

Now x_1 and x_2 can be solved in terms of y_1 and y_2 to obtain:

$$x_1 = G_1(y_1, y_2)$$
$$x_2 = G_2(y_1, y_2)$$

(6.4)

where G_1 and G_2 are also continuous and differentiable. The joint pdf of random variables y_1 and y_2, $u(y_1, y_2)$, is given by [8]:

$$u(y_1, y_2) = f(x_1, x_2) |J(y_1, y_2)|$$

(6.5)

where $f(x_1 = G_1(y_1, y_2), x_2 = G_2(y_1, y_2))$ is the joint pdf of x_1 and x_2, and $J(y_1, y_2)$ is the Jacobian of the transformation. The Jacobian is given by the following determinant:

$$J(y_1, y_2) = \begin{bmatrix} \dfrac{dx_1}{dy_1} & \dfrac{dx_1}{dy_2} \\ \dfrac{dx_2}{dy_1} & \dfrac{dx_2}{dy_2} \end{bmatrix}$$

(6.6)

Recall that the joint pdf of the manufacturing parameters, $f(x_1, x_2)$ is available from the previously obtained neural network models of the joint parameter density.

6.4.1 Results for Gain and Noise Modeling

To construct a joint density function for the four processing parameters, four different statistical distributions from those shown in Figure 33 were selected, and random numbers were generated according to these four distributions using MATLAB [55]. The arbitrarily selected distributions were the bell-shaped, truncated, plateau, and combed distribution for device diameter, barrier-width, mean value of doping concentration, and standard deviation of doping concentration, respectively. Under more realistic conditions, actual input distributions would be derived from in-line measurements in a manufacturing environment, but these commonly occurring distributions were selected merely in order to demonstrate the yield prediction methodology. The histograms of the input parameters are shown in Figure 35.

Using data derived from these distributions as training data, a back-propagation neural network with a 4-9-1 (input-hidden-output) architecture was used to model the joint density function for all four input variables. The parameters for this network are shown in Table 15. To verify this model, the marginal density functions for each input variable were reproduced as shown in Figure 36. As this Figure shows, the marginal distribution of each input parameter is well-matched with the neural network predictions.
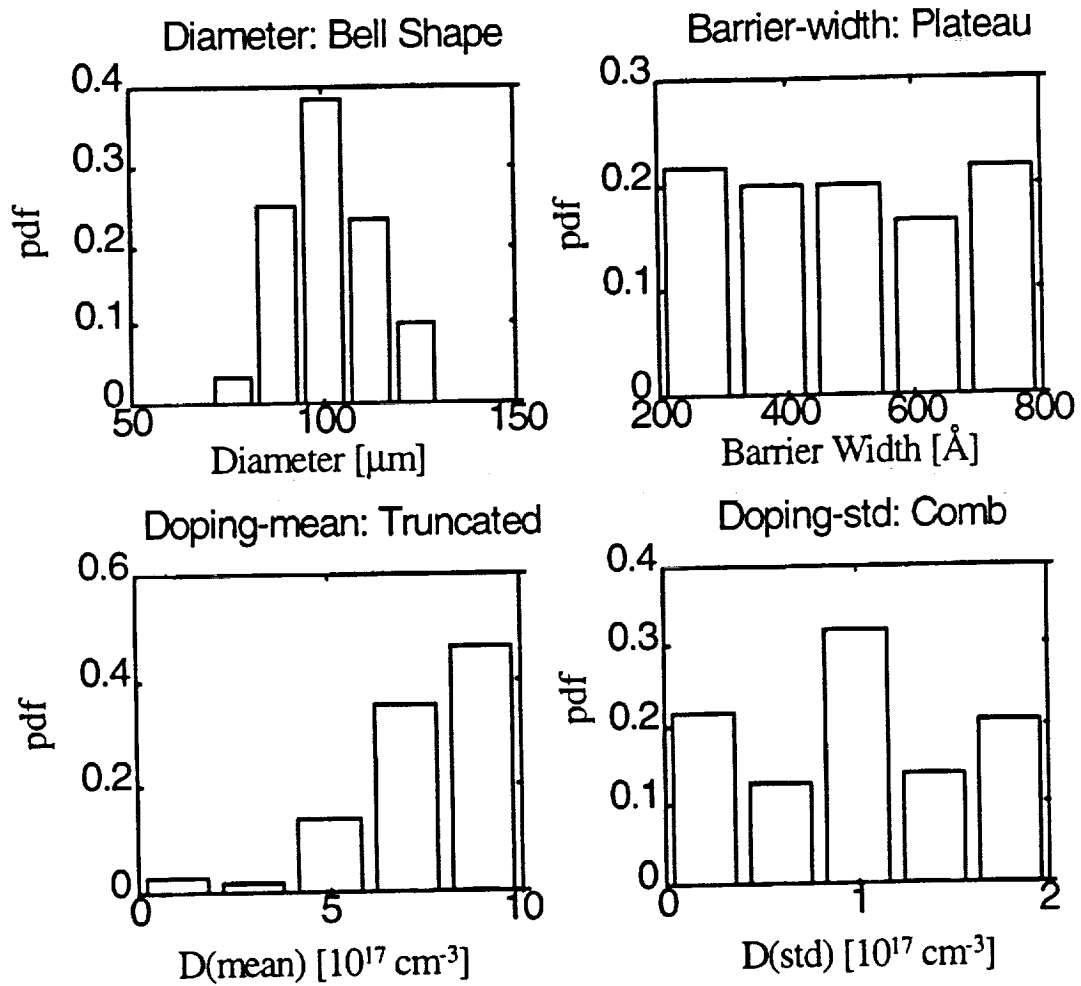
Figure 35 - Histograms of input parameters for gain and noise modeling.

Table 15 - Network Parameters for gain and noise Joint pdf Model

Response	Architecture	Learning rate	Momentum
Joint pdf	4-9-1	0.0005	0.0001

Solid line: Neural Network Output
Dotted line: Input Parameter Distribution
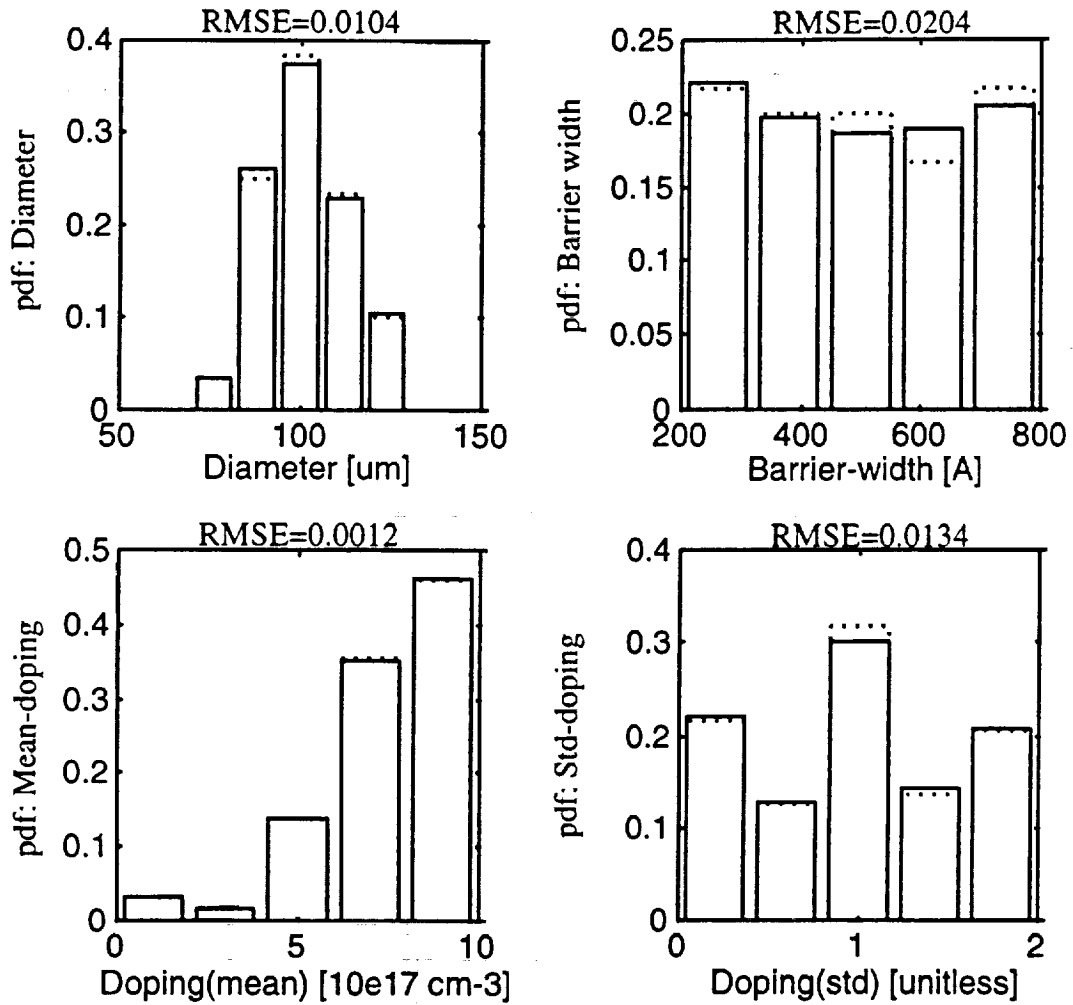
Figure 36 - Predictions of joint pdf neural network model.

6.4.2 Results for Device Lifetime Modeling

For the device lifetime modeling, three processing parameters were used to construct a joint density function. The arbitrarily selected distributions in this case were the bell-shaped, truncated, and combed distribution for device diameter, mean value of doping concentration, and standard deviation of doping concentration, respectively. The histogram of the input parameters are shown in Figure 37.
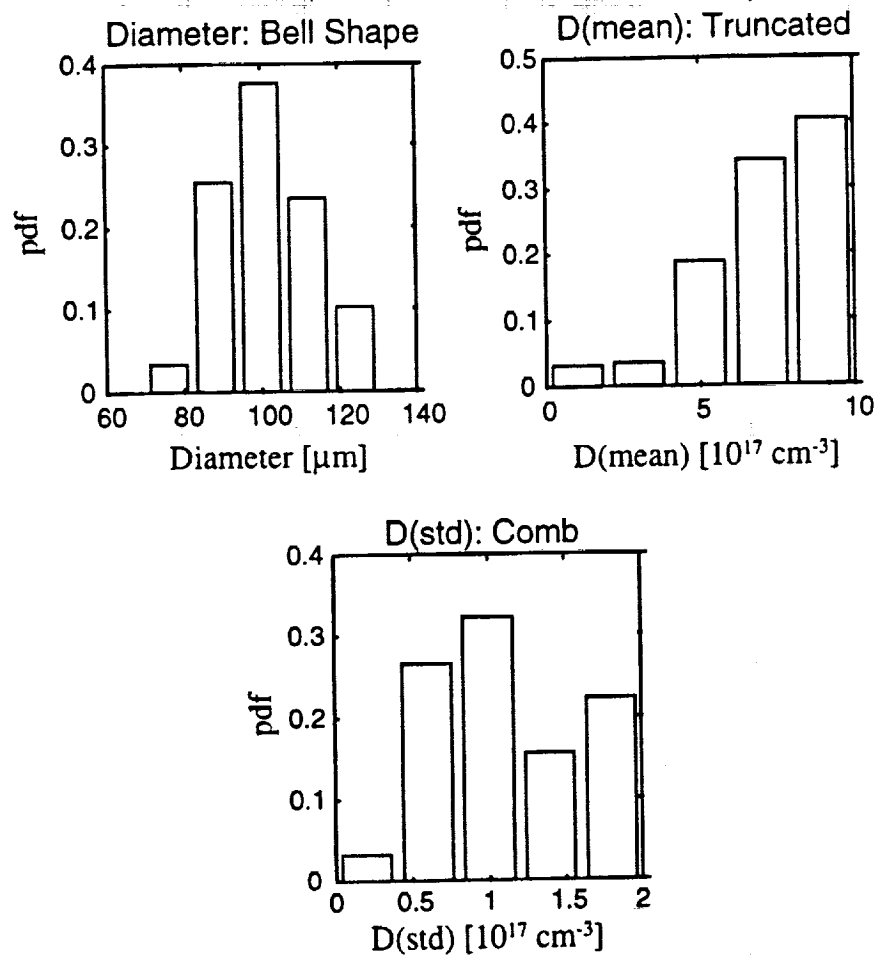
Figure 37 - Histograms of input parameters for lifetime modeling.

Using data derived from these distributions as training data, a back-propagation neural network with a 3-7-1 (input-hidden-output) architecture was used to model the joint density function for all three input variables. The parameter for this network are shown in Table 16. To verify this model, the marginal density functions for each variable were reproduced as shown in Figure 38. As this figure illustrates, the marginal distribution of each input parameter is well-matched with the neural network predictions.

Table 16 - Network Parameters for lifetime Joint pdf Model

Response	Architecture	Learning rate	Momentum
Joint pdf	4-7-1	0.002	0.001

6.5 Parametric Yield Calculation

Once $u(y_1, y_2)$ has been calculated from Equation (6.5), then the marginal densities of the device performance metrics (gain index, noise index or lifetime) may be calculated as follows:

$$I_1(y_1) = \int u(y_1, y_2) dy_2 \approx \sum_{y_2} u(y_1, y_2)$$

$$I_2(y_2) = \int u(y_1, y_2) dy_1 \approx \sum_{y_1} u(y_1, y_2)$$

$$(6.7)$$

Figure 38 - Predictions of lifetime joint pdf neural network model.
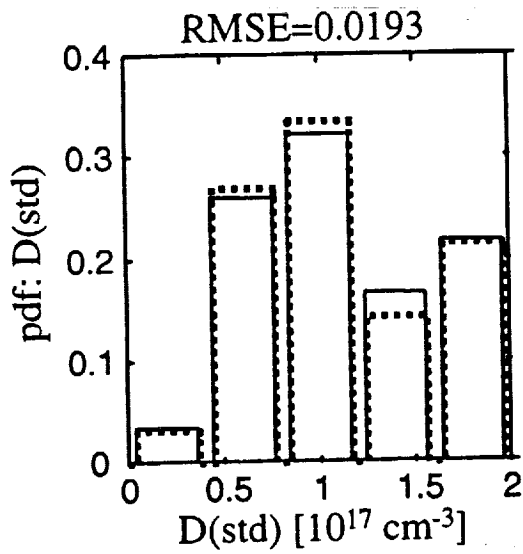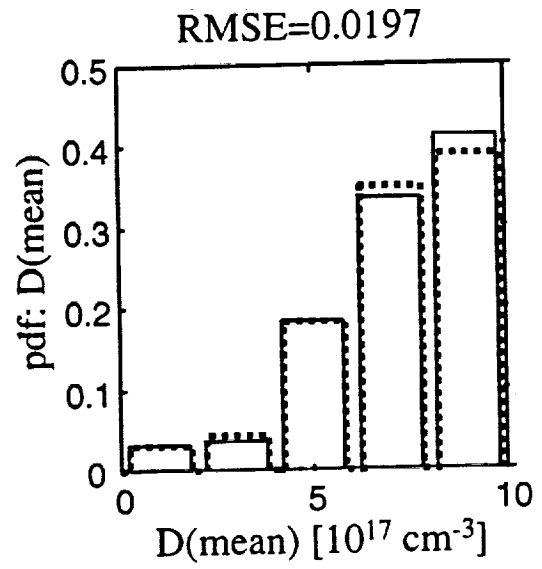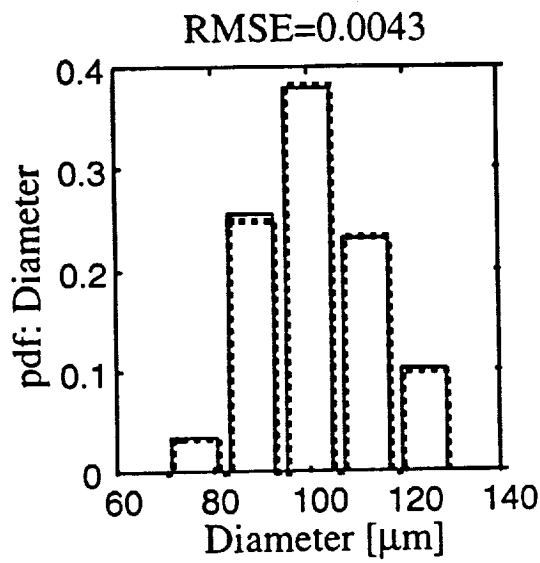
Solid: Neural Network Output
Dotted: Input Parameter Distribution

where $I_1(y_1)$ and $I_2(y_2)$ are the marginal pdfs of the performance characteristics. The parametric yield of the circuit with respect to a given performance measure is then derived from the marginal pdfs as:

$$PY_i = \int_{a_i}^{b_i} I_i(y_i)dy_i \approx \sum_{i=0}^{n-1} I_1(y_{1i}) \cdot (y_{i+1} - y_i) \qquad (6.8)$$

where a_i and b_i represent the limits of integration surrounding regions of interest, and PY_i provides the probability of the device satisfying a particular performance criterion. Using this methodology, the parametric yield of gain, noise and device lifetime can be predicted based on the variation of the manufacturing parameters.

6.5.1 Results for Gain and Noise Modeling

In order to calculate the parametric yield using the joint density function, the Jacobian determinant is must be calculated. The derivatives required for the Jacobian matrix were estimated in the same way that sensitivity analysis was performed using the change in the output quantity with respect to a 5% deviation in the parameter of interest. Following the computation of the Jacobian determinant, parametric yield may be calculated using Equation (6.8). Figure 39 shows the resulting distribution of gain and noise index.
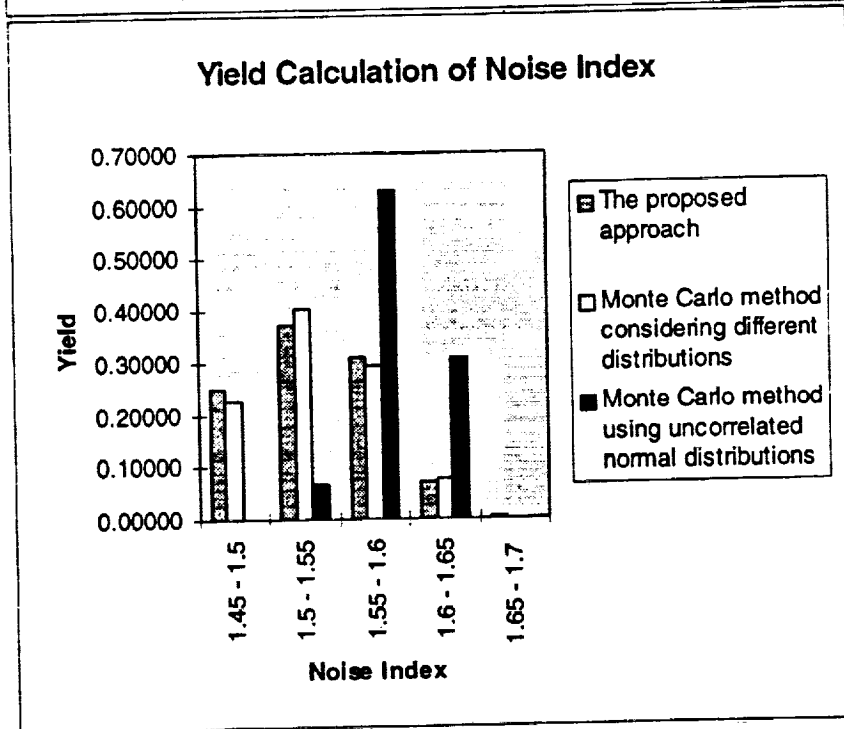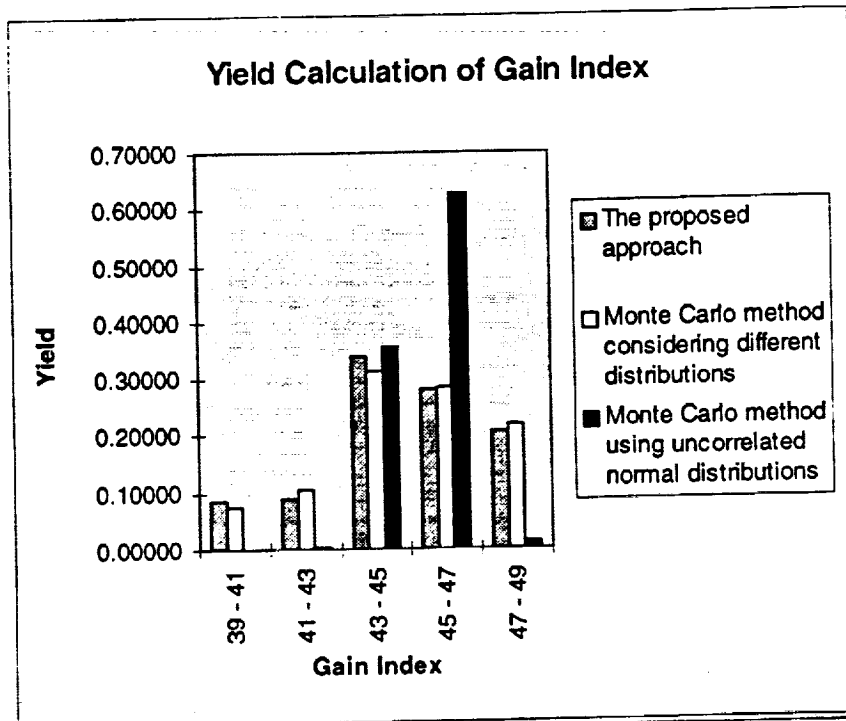
Figure 39 - Final distributions of gain and noise index.

In order to validate this approach, these results can be compared with the Monte Carlo method. Toward that end, simulations consisting of 20,000 randomly generated instances of data were used for calculating parametric yield using the Monte Carlo technique. These randomly generated data sets were fed into the neural network models for gain and noise to calculate the device response. Using the output of the neural network model for each instance of input data, the distribution of gain and noise can be calculated. The two different Monte Carlo simulations were performed. The first approach assumed that all input parameters were independent and normally distributed, ignoring any correlations which might exist between the input parameters. The second Monte Carlo simulation, however, did make use of the different input distributions provided in Figure 35. The Monte Carlo results are also shown in Figure 39.

As expected, Figure 39 shows that the Monte Carlo method performed without considering the correlation of input parameters cannot predict parametric yield accurately. For example, if the uncorrelated Monte Carlo approach is used, the number of devices achieving a gain index between 45 - 47 is severely overestimated. Likewise, the number of devices with a gain index from 47 - 49 is underestimated. In either case, this approach gives misleading information about the effect of the APD manufacturing parameters on device performance.

On the other hand, the newly proposed methodology for parametric yield calculation is comparable to results achieved using the Monte Carlo method that does consider different (and potentially correlated) input distributions, but with significantly fewer simulations. Although some computational overhead is incurred in deriving the

neural network pdf and jpdf models, these models only need to be derived once. In contrast, the Monte Carlo procedure will always require an inordinate number of simulations. Furthermore, it is also asserted here that since the Monte Carlo method uses the same distribution for each input parameter and does not account for possible correlations between parameters, some degree of accuracy is inherently lost. By modeling the input pdfs and their joint pdf directly, the proposed method overcomes this shortcoming.

6.5.2 Results for Device Lifetime Modeling

Since the devices investigated in the APD lifetime study exhibited very limited variation in active diameter and their exact doping profile was unknown, the parametric yield prediction of device lifetime was investigated using the cascaded model described in Section 5.1. Initially, neural network models and inverse neural network models for two cascaded mappings was developed and tested using the OBORNNS simulator. Then, a simulated joint probability density function of the relevant input manufacturing parameters (i.e. - active diameter, and mean and standard deviation of doping concentration), was generated from these models. Finally, parametric yield estimation of APD device lifetime was performed via the Jacobian transformation method. Two APD structures (doped-barrier and doped-well) were investigated using this procedure.

6.5.2.1 Doped Barrier MQW APD

Using the Jacobian matrix and the cascaded neural network models, the parametric yield for doped-barrier APDs is calculated using Equation (6.8). The neural network models with three different temperatures, 100°C, 150°C, and 200°C, were evaluated for calculating parametric yield. Figure 40 shows the resulting distribution of device lifetime for doped-barrier APDs.

In order to validate this approach, these results are again compared with the Monte Carlo method consisting of 20,000 randomly generated instances of data. These randomly generated data sets were fed into the neural network models for device lifetime to calculate the device response. Using the output of the neural network model for each instance of input data, the distributions of device lifetime for three different temperatures can be calculated. The two different Monte Carlo simulations were also performed. The first assumed that all input parameters were independent and normally distributed, ignoring any correlations which might exist between the input parameters. The second Monte Carlo simulation made use of the different input distributions provided in Figure 37. The Monte Carlo results are also shown in Figure 40.

As expected, Figure 40 shows that the Monte Carlo method performed without considering the correlation of input parameters cannot predict parametric yield accurately. For example, if the uncorrelated Monte Carlo approach is used, the number of devices achieving a device lifetime (log-scale) at 100°C between 3.12 - 3.18 is underestimated,

101

and the number of devices with a device lifetime at 100°C from 3.18 - 3.24 is overestimated.

6.5.2.2 Doped Well MQW APD

Using the same methodology described in Section 6.5.2.1, the parametric yield for doped-well APDs is also calculated using Equation (6.8). Figure 41 shows the resulting distribution of device lifetime for doped-barrier APDs.

As expected, Figure 41 shows that the Monte Carlo method performed without considering the correlation of input parameters cannot predict parametric yield accurately. For example, if the uncorrelated Monte Carlo approach is used, the number of devices achieving a device lifetime at 150°C between 2.30 - 2.46 is overestimated and the number of devices with a device lifetime at 150°C from 2.54 - 2.70 is underestimated.
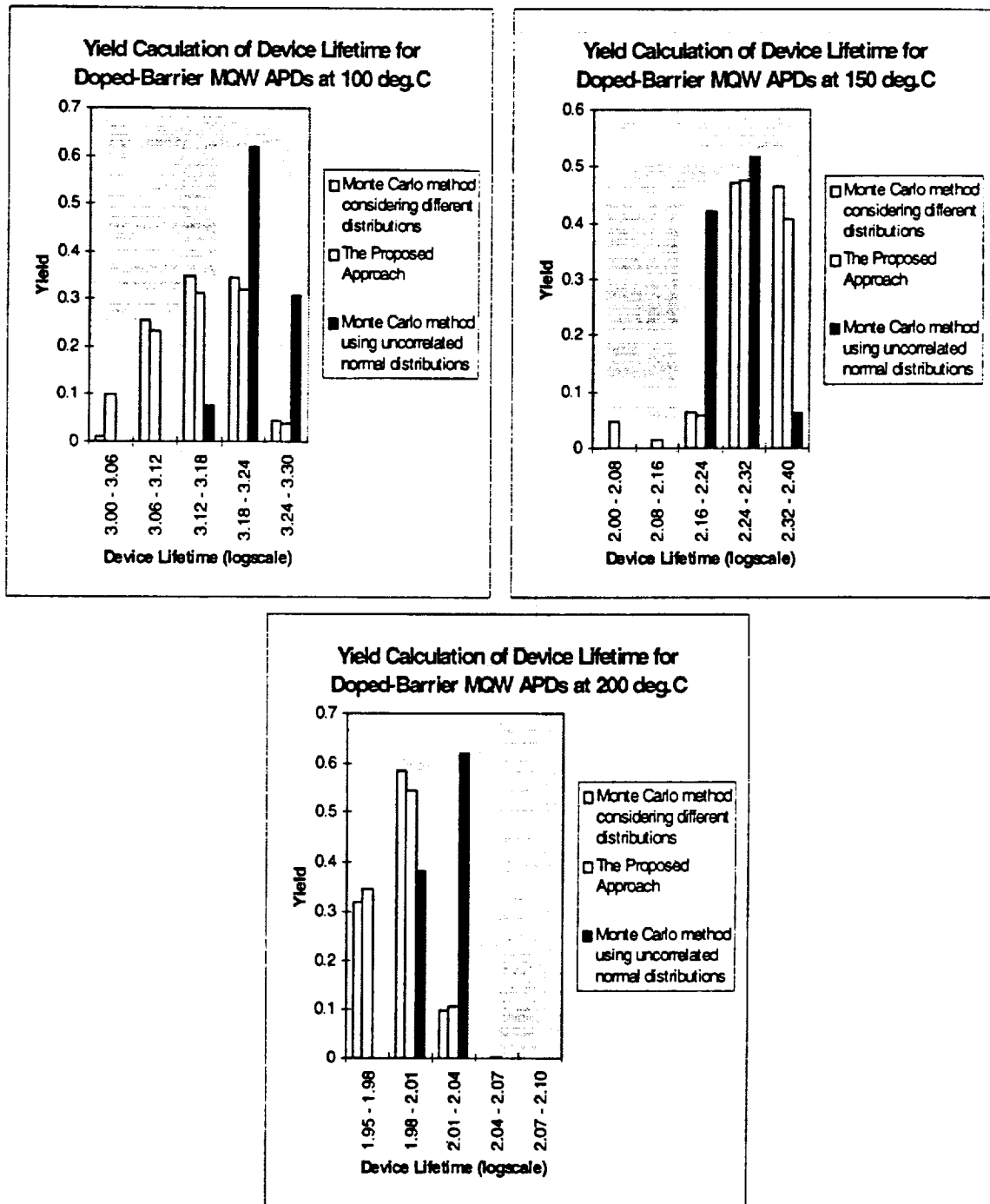
Figure 40 - Final distribution of device lifetime for doped-barrier APDs.
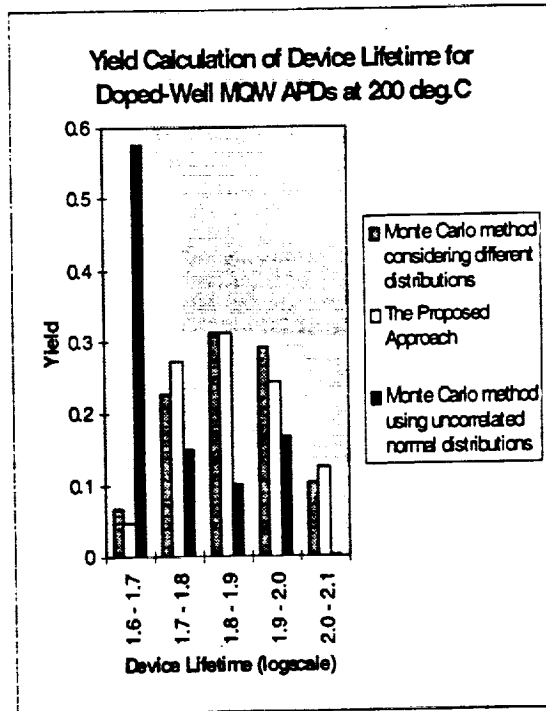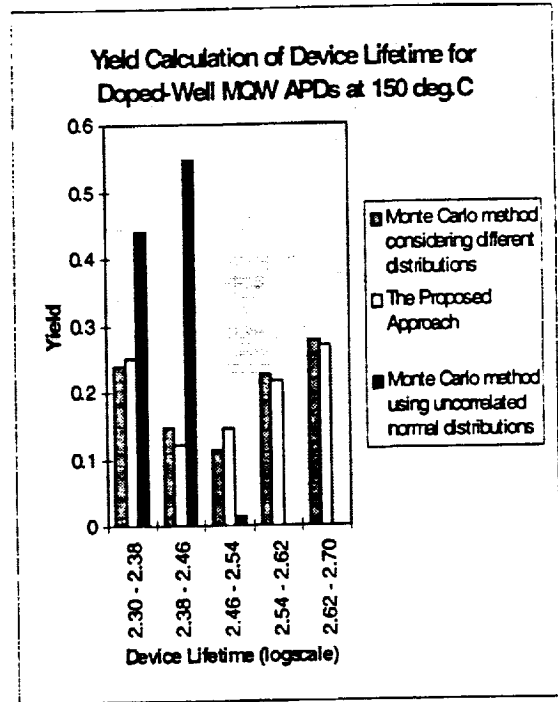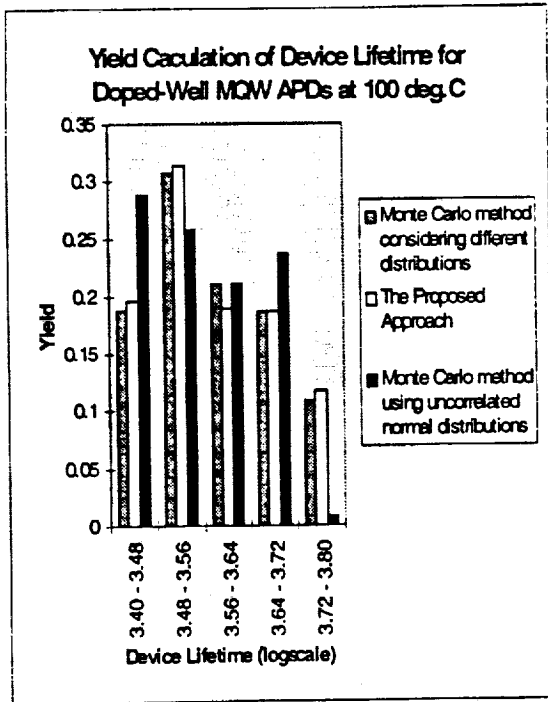
Figure 41 - Final distribution of device lifetime for doped-well APDs.

6.6 Sensitivity of Parametric Yield to Distributions of Manufacturing Parameters

6.6.1 Overview of Problem

Based on the preliminary results of the APD gain, noise and device lifetime yield calculation, it becomes desirable to investigate how different distributions of the manufacturing parameters impact parametric yield. For example, truncated distributions are often found in manufacturing due to the application of statistical process control procedures. The "tightness" of process specifications determines where the distribution is truncated (i.e. +/- 3-sigma, etc.). It is useful to evaluate the sensitivity of the parametric performance of the device to the choice of truncation point. In addition, it is valuable to search for regions in the yield space which are relatively insensitive to changes in the distributions of the input parameters. In such regions, the performance of the device will be relatively robust to manufacturing variations. One possible approach to accomplish this is to: 1) perform sensitivity analysis on each output response, finding the insensitive region for each input parameter; 2) generate pseudo-random data sets of input parameters in the insensitive region; and 3) use these distributions to calculate the parametric yield and check the distribution of each output response. This analysis will allow the process engineer and device designer to work together to define performance metrics which are insensitive to process fluctuations, thereby ensuring high parametric yield.

In this section, three different hypothetical scenarios will be investigated. First, the effect of different ranges of input parameter distributions on the parametric yield is

discussed. This will allow the prediction of the ranges of the input parameter distributions which can reduce process variations and increase parametric yield. Second, the impact of different distributions of input parameters on the parametric yield is examined. Finally, the sensitivity of the parametric performance to the choice of truncation point is evaluated for truncated distributions.

6.6.2 Result and Discussion

6.6.2.1 Effect of range of input distribution

The first scenario involves three normal distributions of device diameter with different mean values which were constructed to evaluate parametric yield. The histograms for these distributions are shown in Figure 42. The distributions for barrier width, mean value of doping concentration, and standard deviation of doping are the same for each of these cases. From these input distributions, the proposed methodology was applied to calculate the parametric yield. Figure 43 illustrates the resulting distribution of gain and noise for doped-well APDs.

Figure 42 - Histograms of input parameters in scenario 1: Diameter.
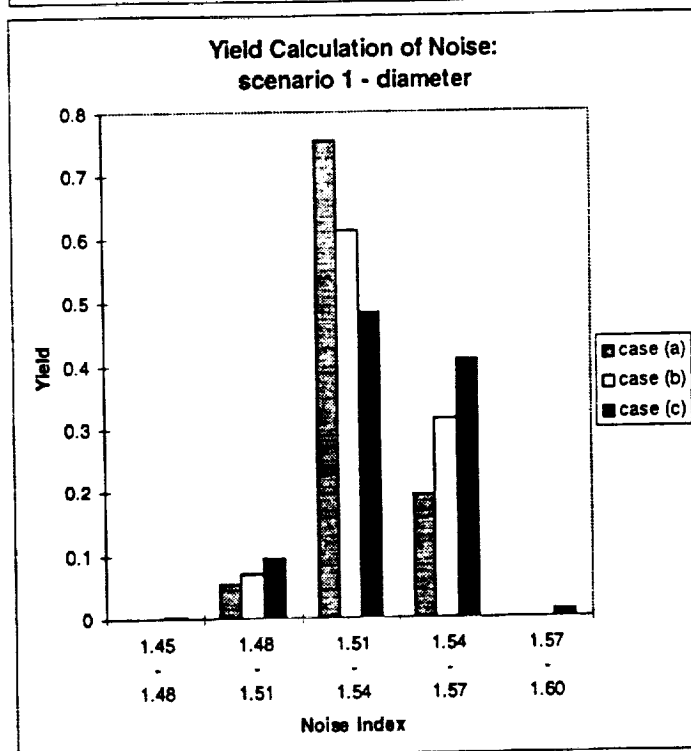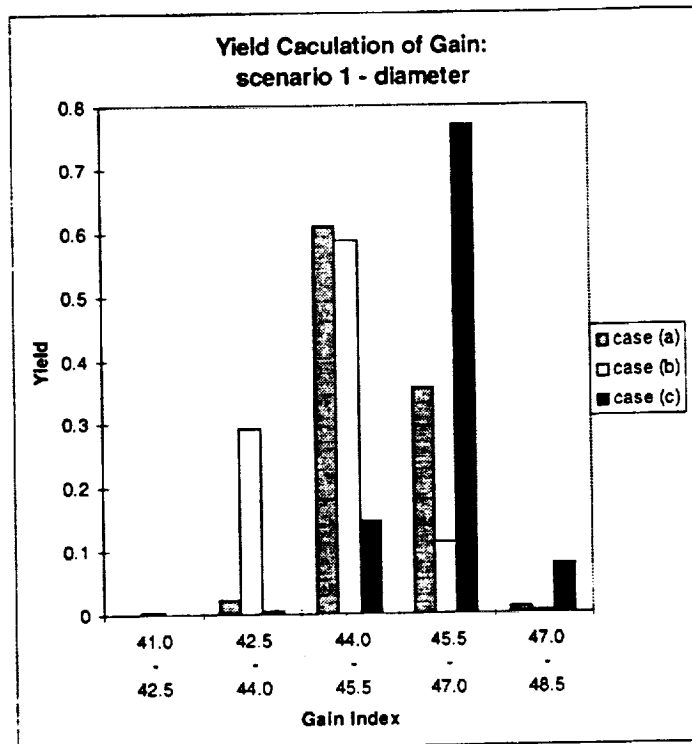
Figure 43 - Final distributions of gain and noise in scenario 1: Diameter.

The results in Figure 43 show that the different ranges of device diameter significantly impacted parametric yield. These results are in good agreement with Figure 21, which indicates that large diameter devices exhibit higher light current compared to smaller devices. In other words, a larger diameter device can convert more optical energy to the light current, resulting in a higher gain index. If the desired range of gain index is no less than 44, then case (c), which contains larger diameter devices, provides the highest yield. Likewise, if the desired range of noise index is between 1.51 - 1.54, then case (a), which contains smaller diameter devices, shows the highest yield.

Three statistical distributions of the mean value of doping concentration with different mean values were also constructed. The histograms of these distributions are shown in Figure 44. The distributions for device diameter, barrier width, and standard deviation of doping are the same for these cases. From these input distributions, the new methodology was again applied to calculate the parametric yield. Figure 45 illustrates the resulting distribution of gain and noise for doped-well APDs.

The results in Figure 45 show the effect of mean value of doping concentration on parametric yield. More dopants can participate in the impact ionization process for the higher doping case. This results in larger light current and higher gain index. In addition, since more dopants participating in the avalanche process can contribute to the ionization rate, noise index also increases with higher doping. If the desired range of gain index is no less than 45.5, then case (a), which contains devices with a smaller mean value of doping concentration, exhibit the highest yield. Likewise, if the desired range of noise index is no less than 1.54, then case (c), which contains devices with larger mean value of

Figure 44 - Histograms of input parameters in scenario 1: Mean doping.
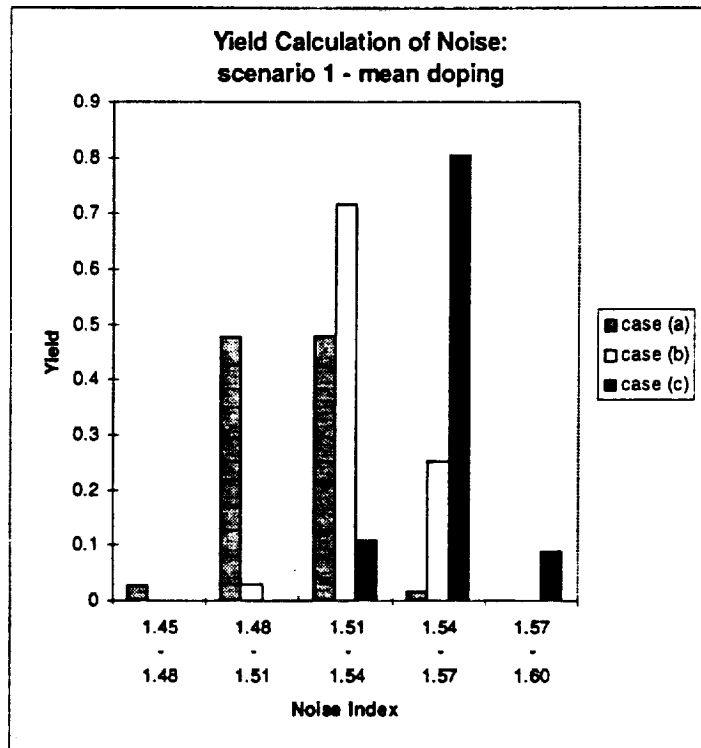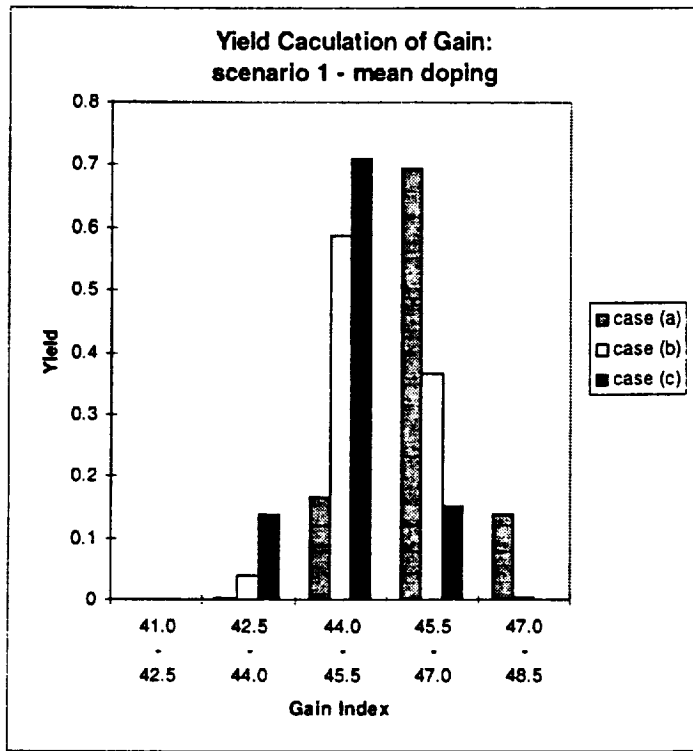
Figure 45 - Final distributions of gain and noise in scenario 1: Mean doping.

doping concentration, can obtain highest yield. There is obviously a design trade-off between higher gain index for a small mean value of doping concentration and higher noise index for a large mean value of doping concentration.

6.6.2.2 Effect of Different Distributions

For this scenario, three different statistical distributions (normal, truncated and uniform distribution) of device diameter are investigated to evaluate parametric yield. The histograms of these input distributions are shown in Figure 46. The distributions for barrier width, mean value of doping concentration, and standard deviation of doping were the same for these cases. Figure 47 illustrates the resulting distribution of gain and noise for doped-well APDs.

The results shown in Figure 47 prove different distributions of device diameter do impact parametric yield in the case of gain. For example, if the higher gain index is desired, then case (c), which contains truncated distribution of diameter, shows the highest yield since the truncated distribution has a large population in larger device diameter. However, noise index is relatively insensitive to the different diameter distributions. From the final distribution of noise index in Figure 47, it is seen that noise index is fairly insensitive to the different distributions in device diameter.

In addition, simulations involving three different statistical distributions of mean value of doping concentration were also performed to evaluate parametric yield for gain and noise. The histogram of these input distributions are shown in Figure 48. The

distributions for device diameter, barrier width, and standard deviation of doping are the same for these cases. Figure 49 shows the resulting parametric yield distribution of gain and noise for doped-well APDs.
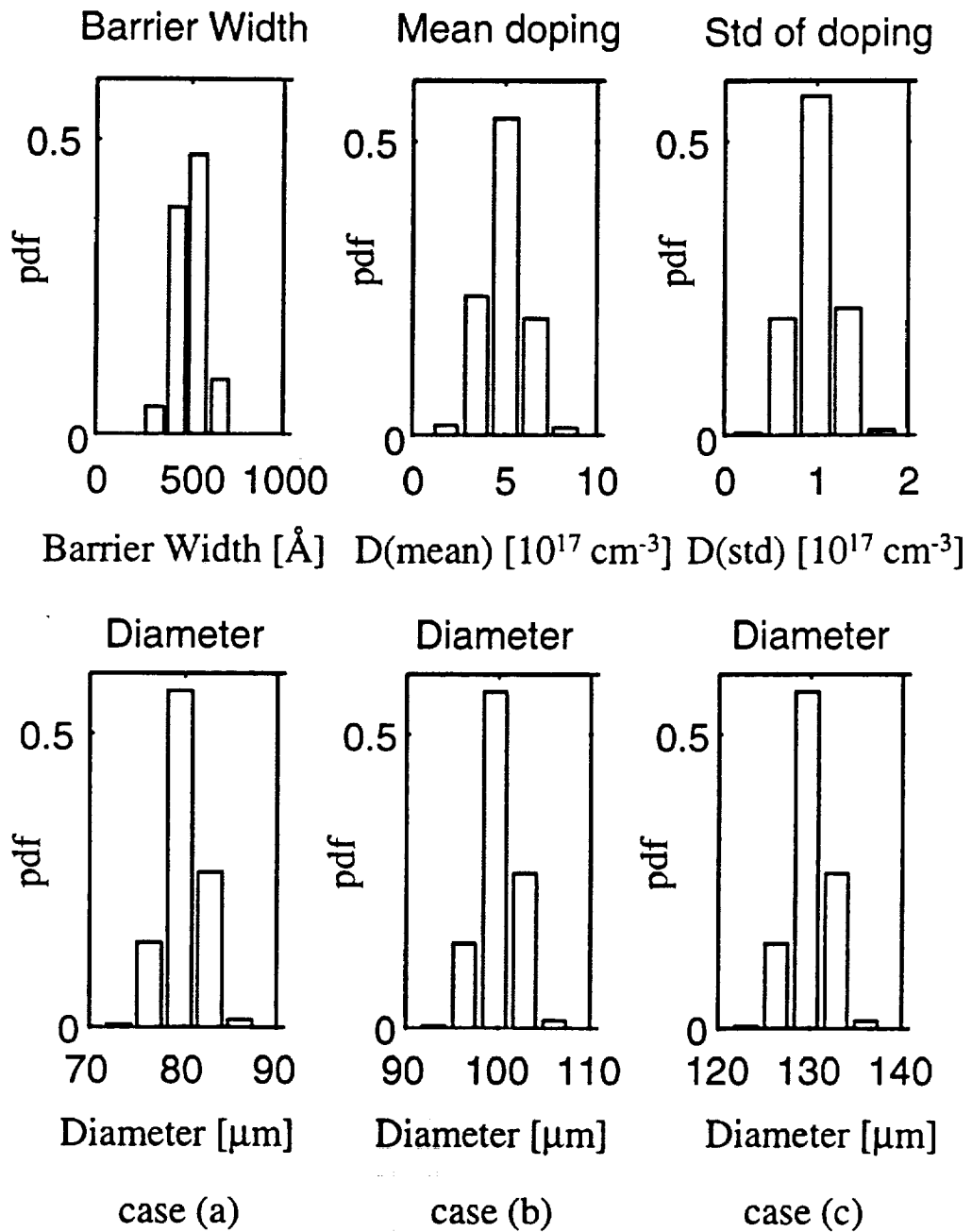

Figure 46 - Histograms of input parameters in scenario 2: Diameter.

Figure 47 - Final distributions of gain and noise in scenario 2: Diameter.
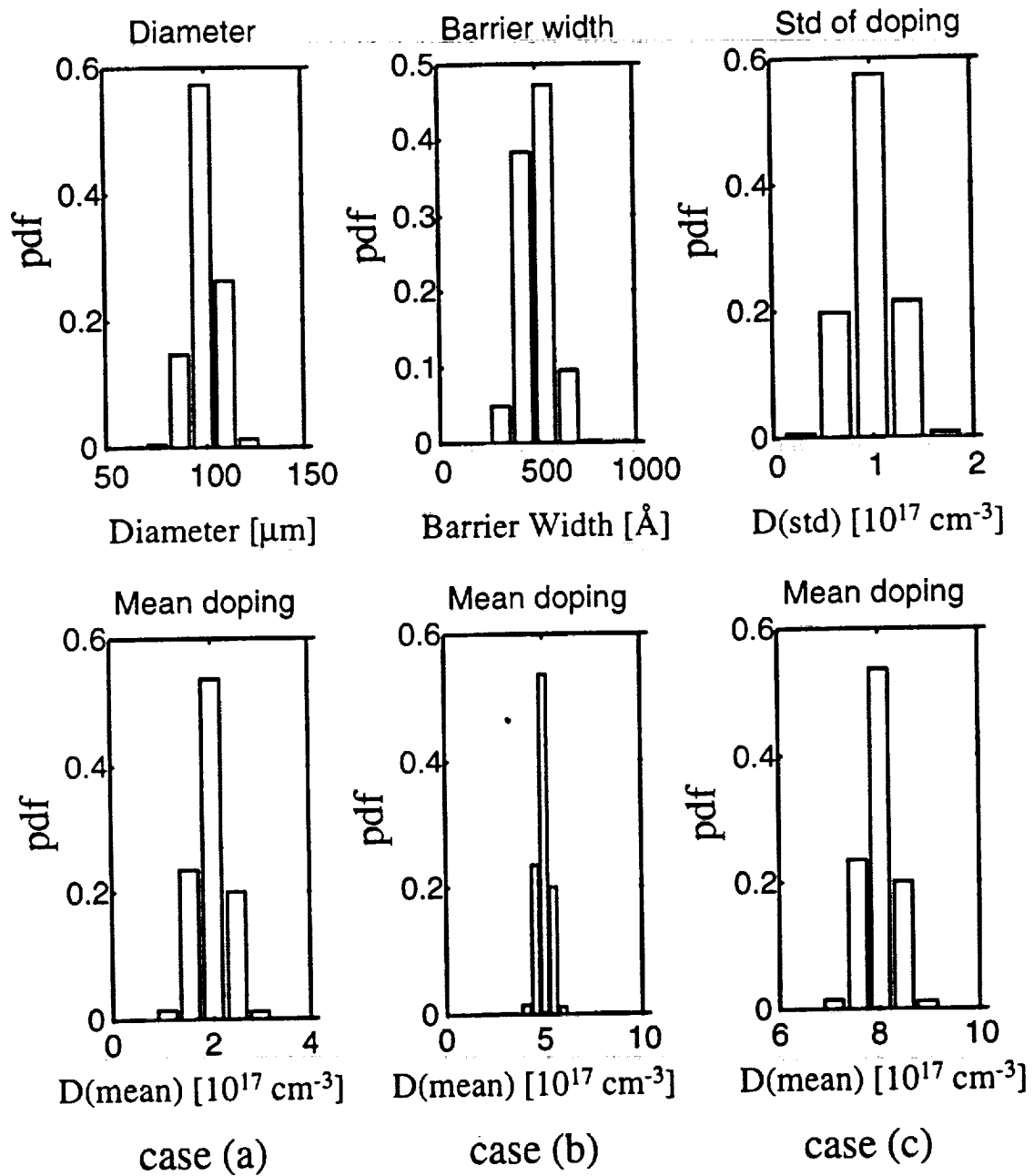
Figure 48 - Histograms of input parameters in scenario 2: Mean doping.
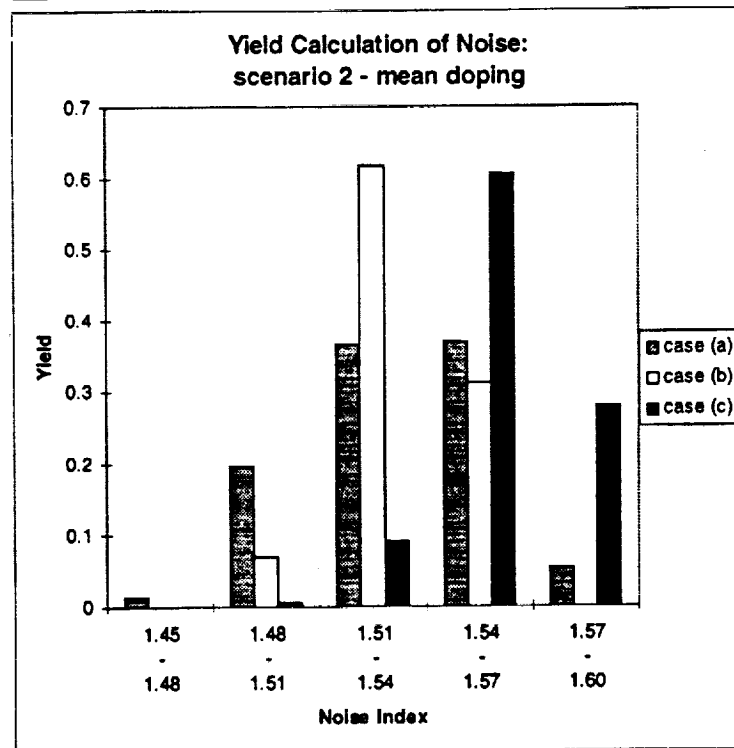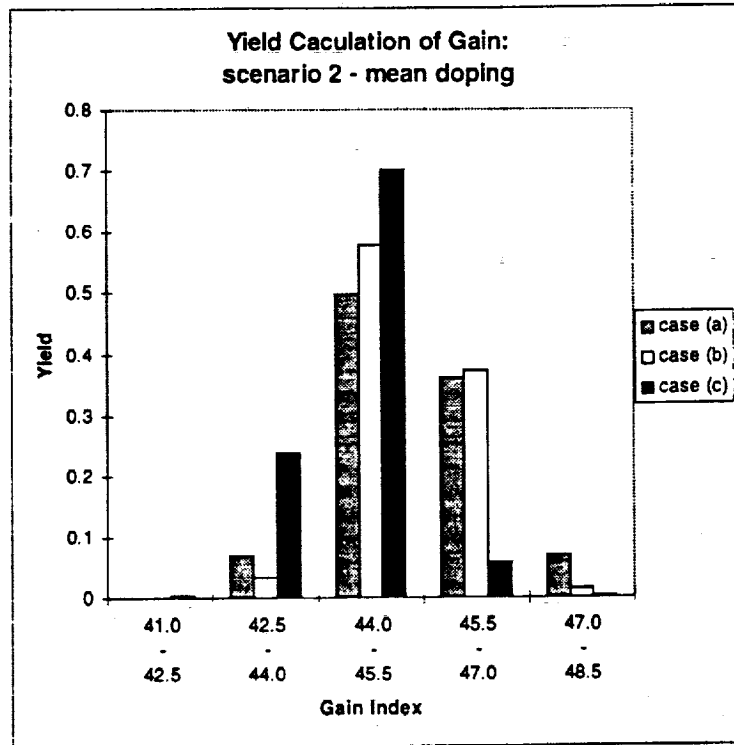
Figure 49 - Final distributions of gain and noise in scenario 2: Mean doping.

The results shown in Figure 49 verify that different distributions of mean value of doping concentration can impact parametric yield. These results also shows a good agreement that truncated distribution with a larger population in large mean value of doping concentration exhibit the highest yield. Note that since the large noise index (which means a large ionization coefficient ratio) is required for reducing excess noise, a high mean value of doping concentration is preferred for higher parametric yield.

6.6.2.3 Effect of Truncated Distributions

Finally, the sensitivity of the parametric performance of the device to the choice of truncated point for truncated distributions was investigated. Truncated distributions are often found in manufacturing due to the application of statistical process control procedures. Since any manufacturing process contains inherent process fluctuation, quick detection of out-of-control states is required to maintain product conformance. Usually, the process specifications serve to control the process by truncating the distribution of the measured parameter. It can therefore be useful to evaluate which truncated point provides the highest yield.

Three different truncation points of device diameter were investigated to evaluate parametric yield for gain and noise. The histograms of these input distributions are shown in Figure 50. The truncation points for case (a), case (b), and case (c) are [73, 121], [81, 115], and [90, 108], respectively. The distributions for barrier width, mean value of doping concentration, and standard deviation of doping were the same for each

117

case. Figure 51 illustrates the resulting parametric yield distribution of gain and noise for doped-well APDs.

From these results, it was found that different truncation points of device diameter do not significantly impact parametric yield. Regardless of different truncated points in diameter distributions, both gain and noise are insensitive to these distributions.

Different truncation points for the mean value of doping concentration were also studied to evaluate parametric yield for gain and noise. The histograms of these input distributions are shown in Figure 52. The truncated points for case (a), case (b), and case (c) are [0.1, 9.9], [2.5, 7.5], and [3.75, 6.25], respectively. The distributions for device diameter, barrier width, and standard deviation of doping are the same for these cases. Figure 53 shows the resulting yield distributions of gain and noise for doped-well APDs.

These results confirm that different truncation points of mean value of doping concentration impact parametric yield. If the truncation points are very tight, the resulting yield distribution is also tight. If parametric yield for noise is desired in the range of [1.51, 1.57], case (b) and case (c) yield 92% and 96%, respectively. Therefore, if the process is hard to control, then distributions with wide truncation points can yield nearly similar results to distributions with narrow truncation points. It is also noted that parametric yield of gain is almost insensitive to the different truncation points in the mean value of doping concentration.
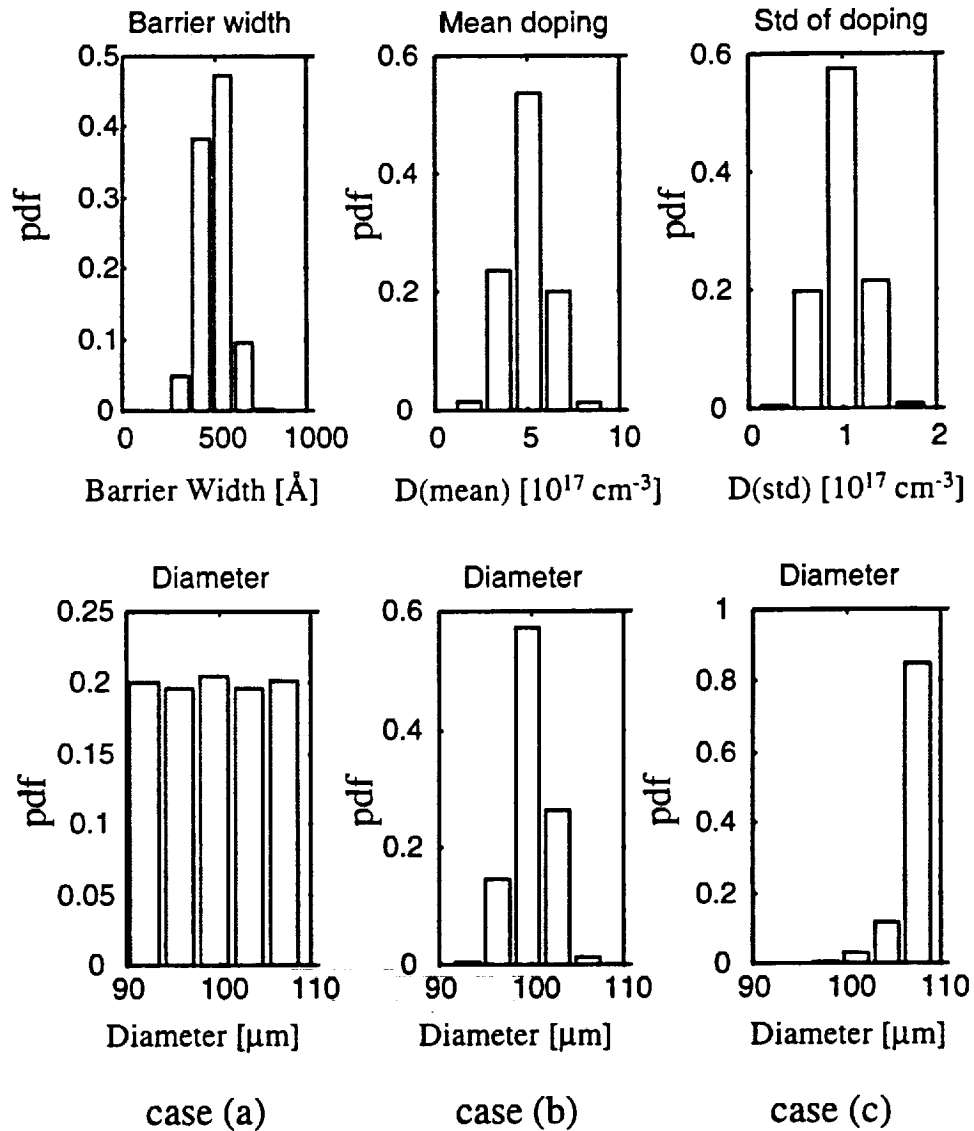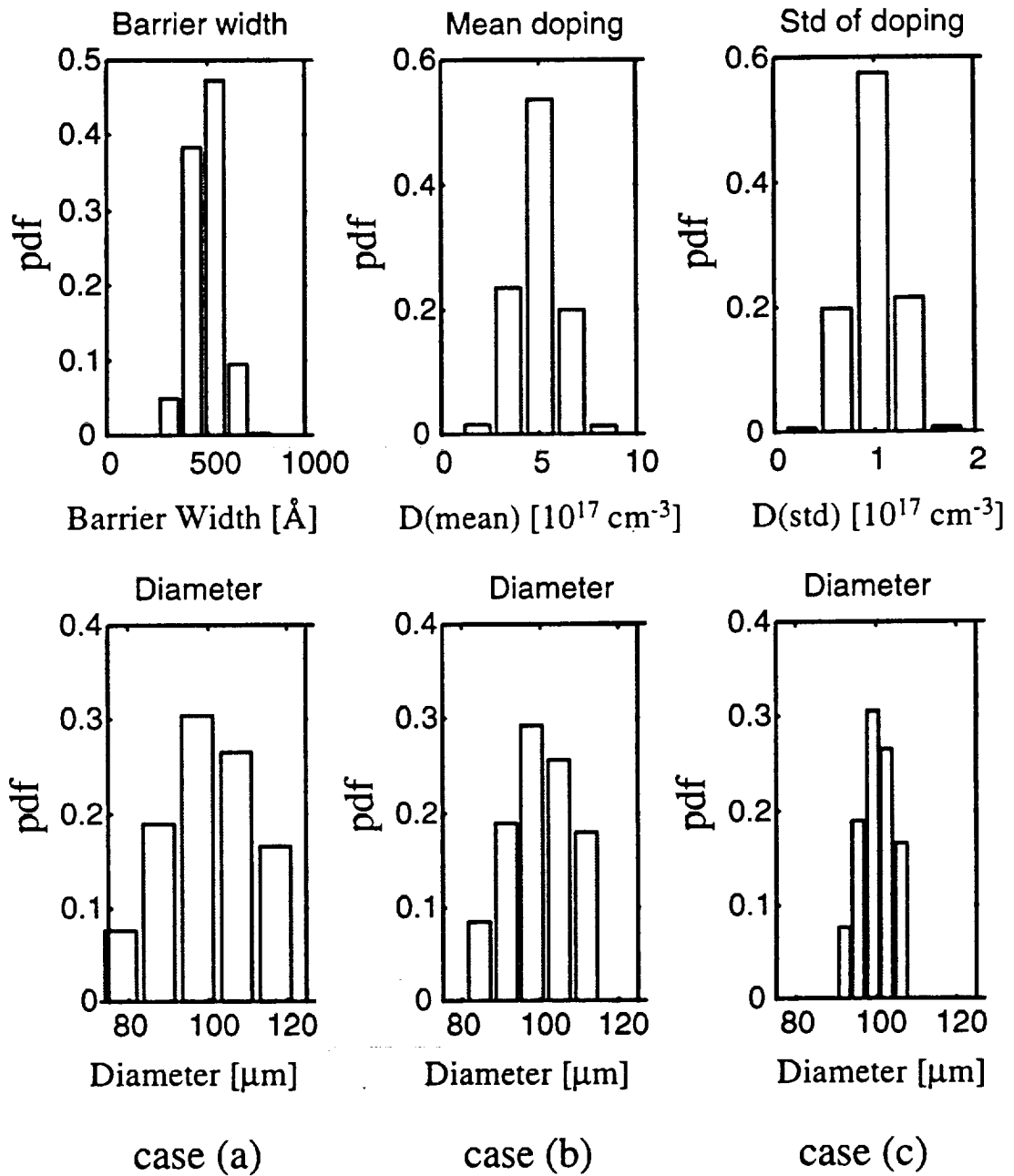
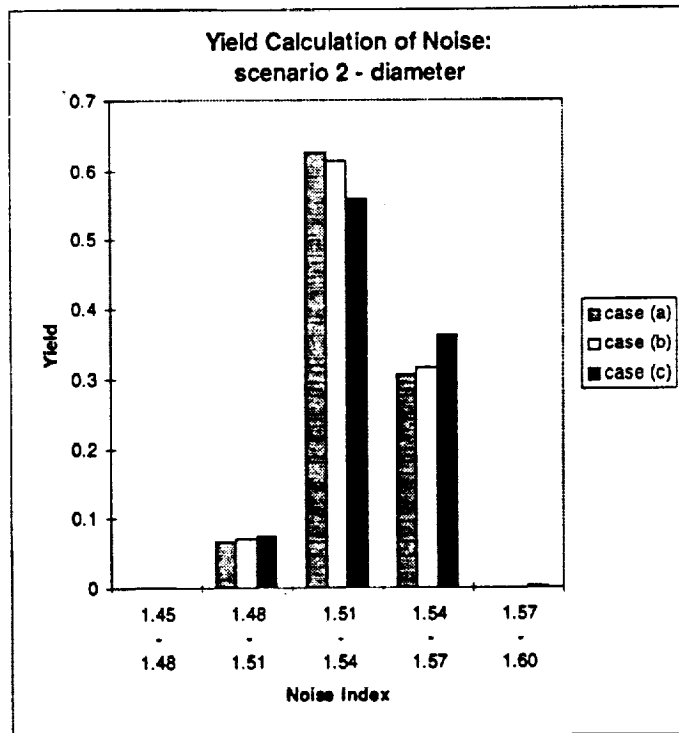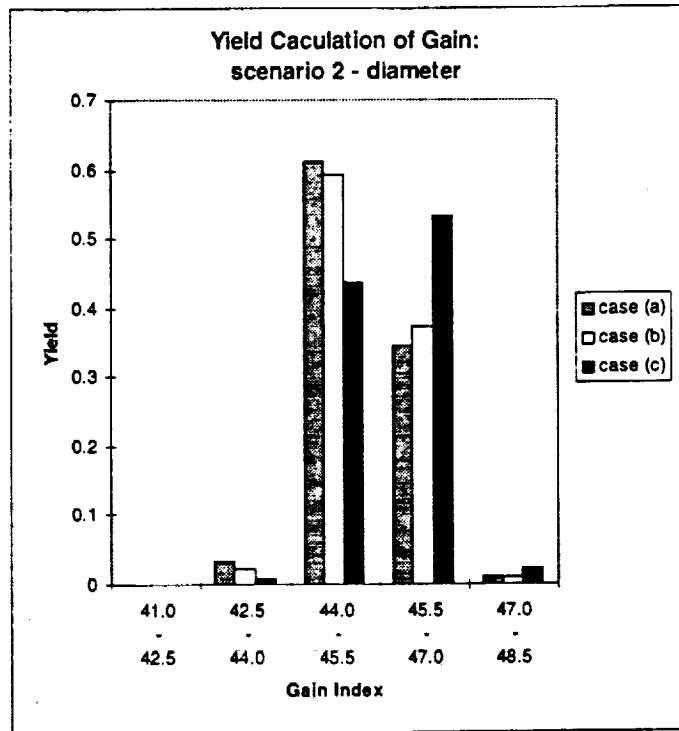Figure 50 - Histograms of input parameters in scenario 3: Diameter.
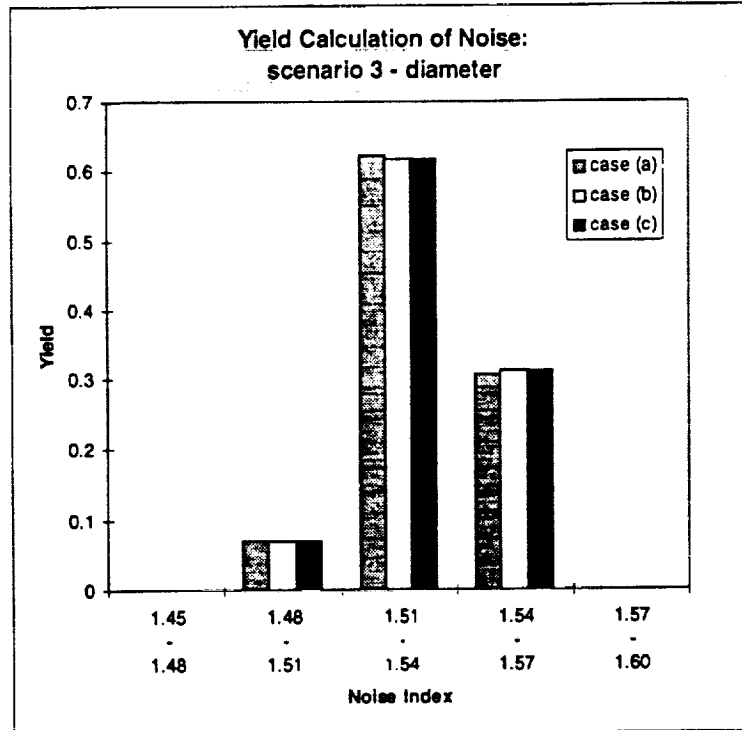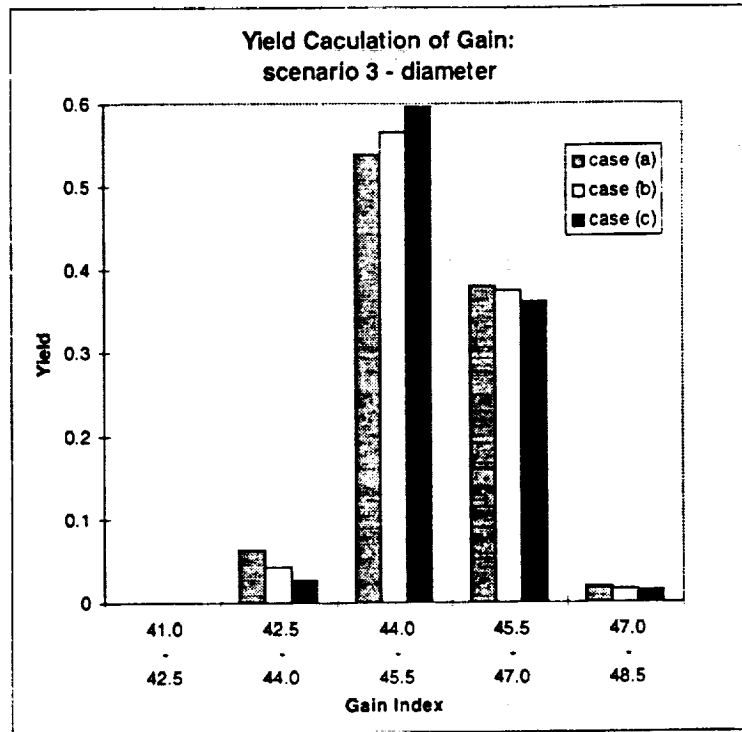
Figure 51 - Final distributions of gain and noise in scenario 3: Diameter.
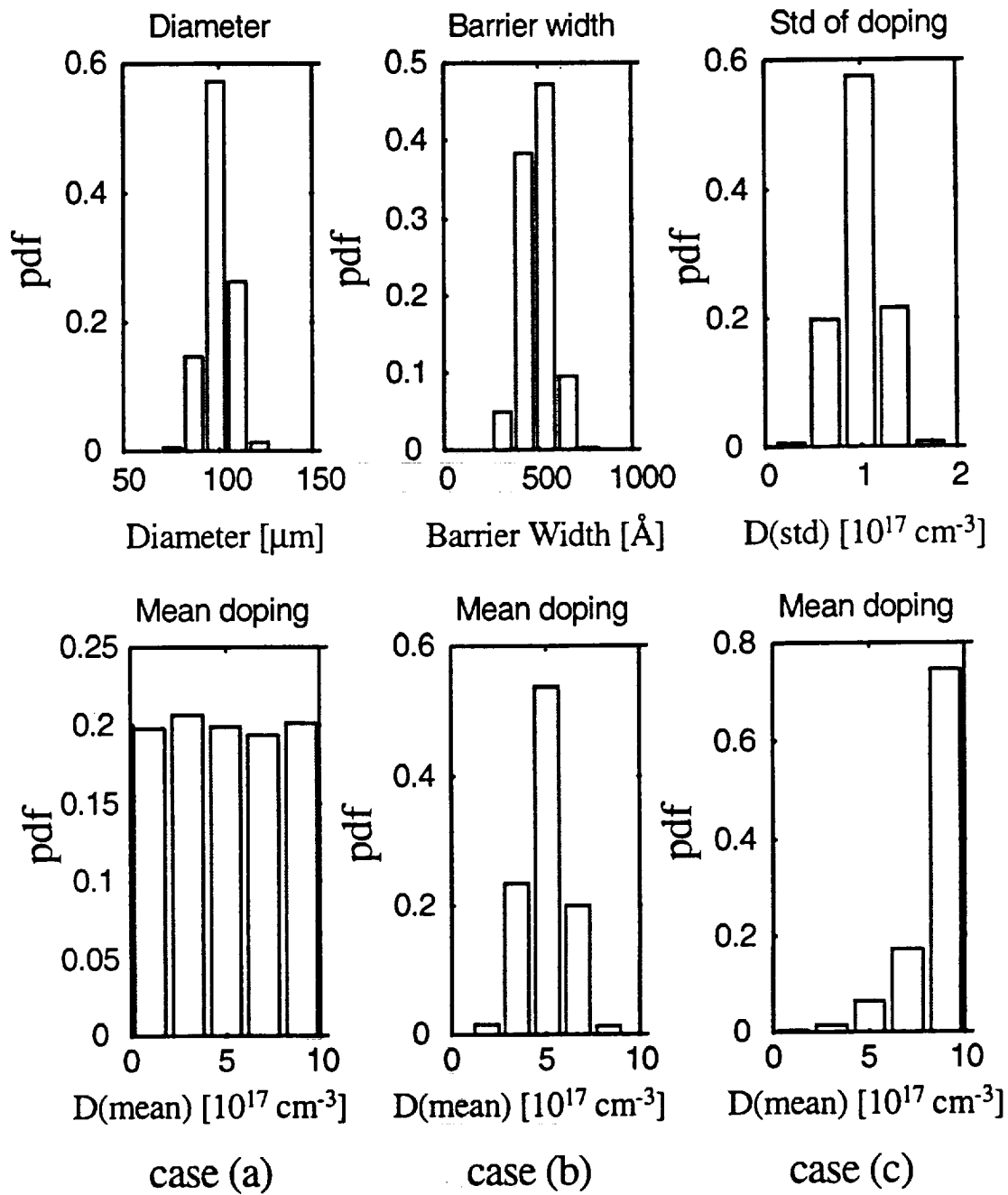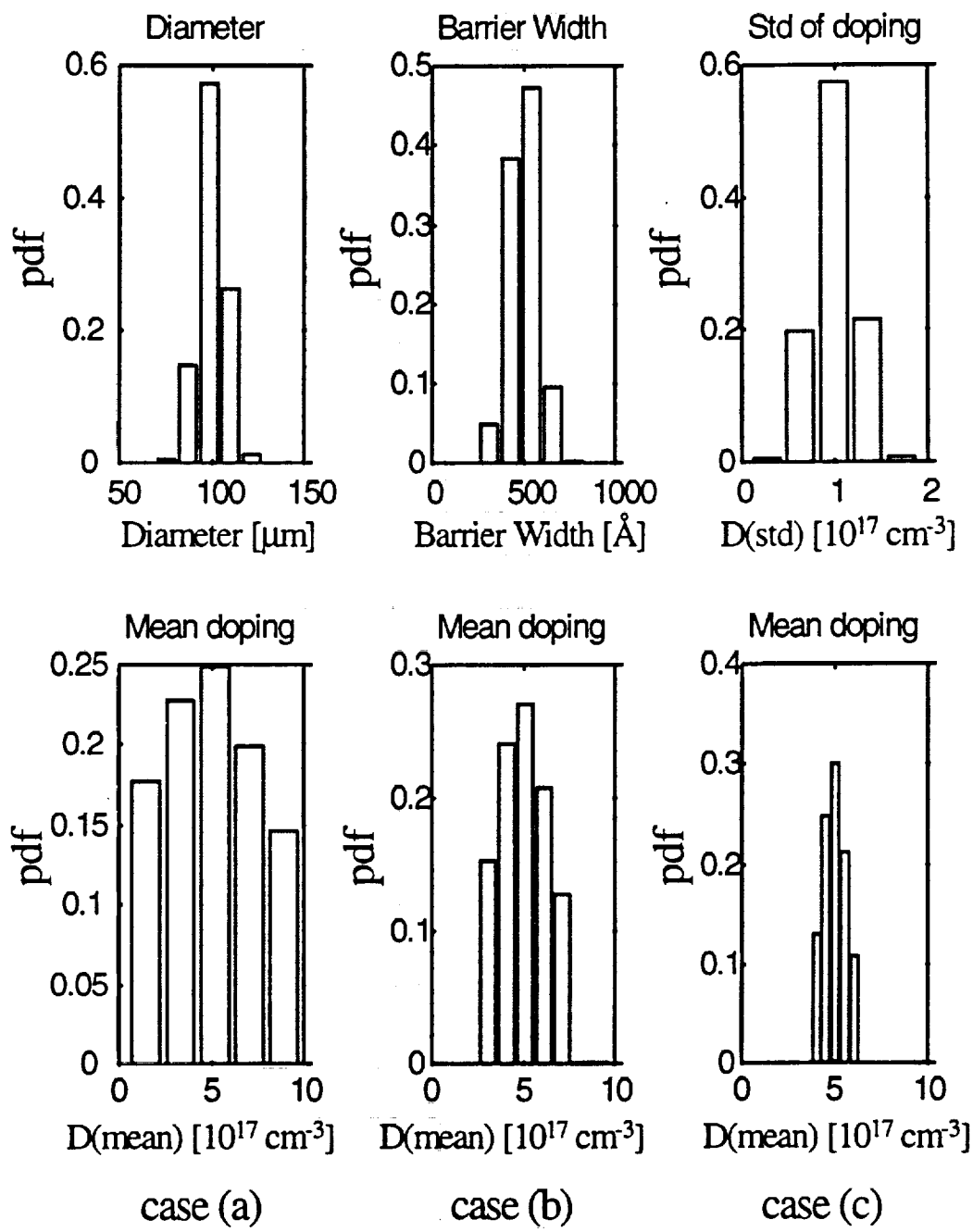
Figure 52 - Histograms of input parameters in scenario 3: Mean doping.
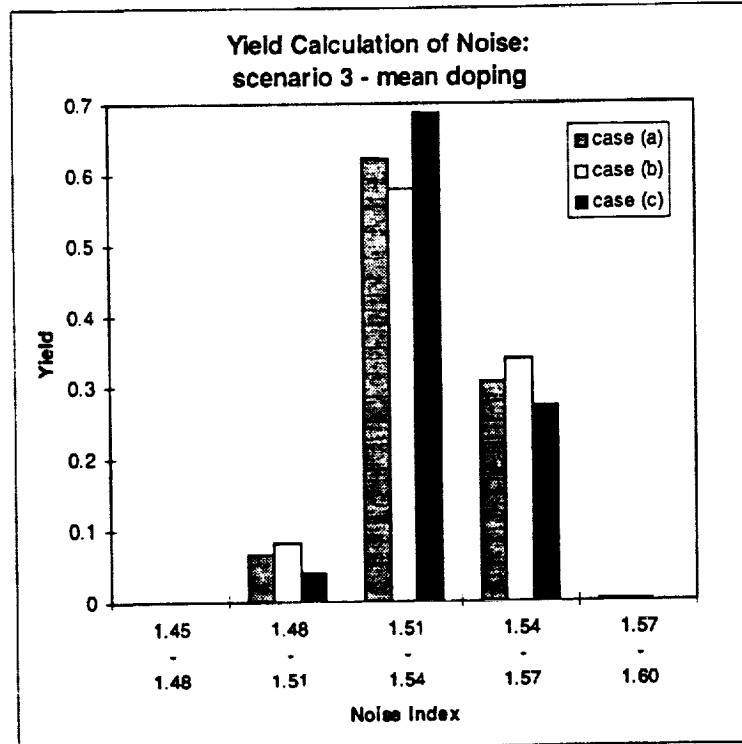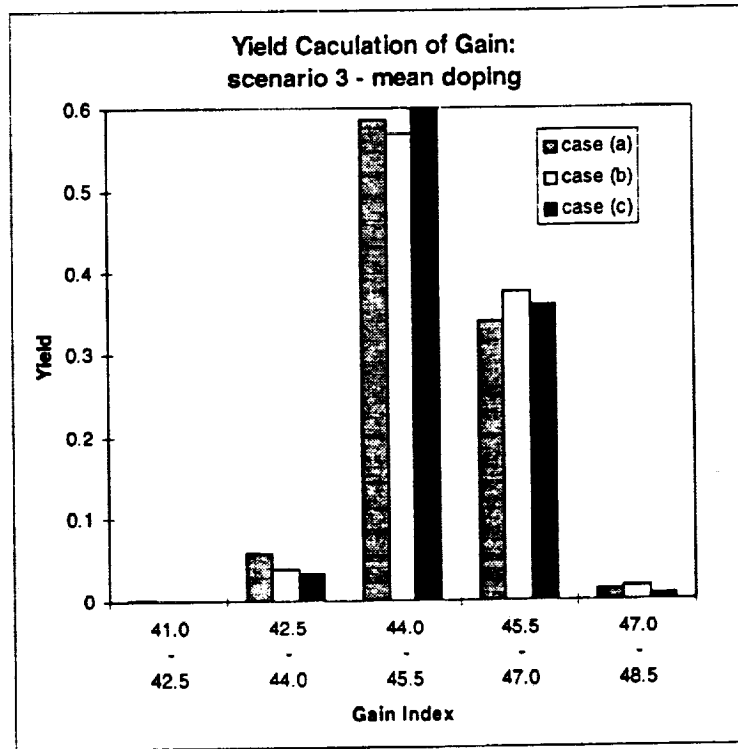
Figure 53 - Final distributions of gain and noise in scenario 3: Mean doping.

Different truncation points of the standard deviation of doping concentration were also performed to evaluate parametric yield for gain and noise. The histograms of these input distributions are shown in Figure 54. The truncated points for case (a), case (b), and case (c) are [0.1, 1.9], [0.4, 1.6], and [0.75, 1.25], respectively. The distributions for device diameter, barrier width, and standard deviation of doping were the same for each case. Figure 55 shows the resulting yield distribution of gain and noise for doped-well APDs.

The results shown in Figure 55 confirm that different truncation points for the standard deviation of doping concentration can also impact parametric yield. Case (c), which corresponds to narrow truncation points, exhibits the highest yield of gain. Thus, delta doping, which is conceptually similar to narrow truncation limits, can be a great advantage in improving parametric yield. Therefore, precise control of the doping profile is a key factor to fabricate high performance devices. Noise index, on the other hand, is fairly insensitive to the placement of the truncation points in the standard deviation of doping concentration.
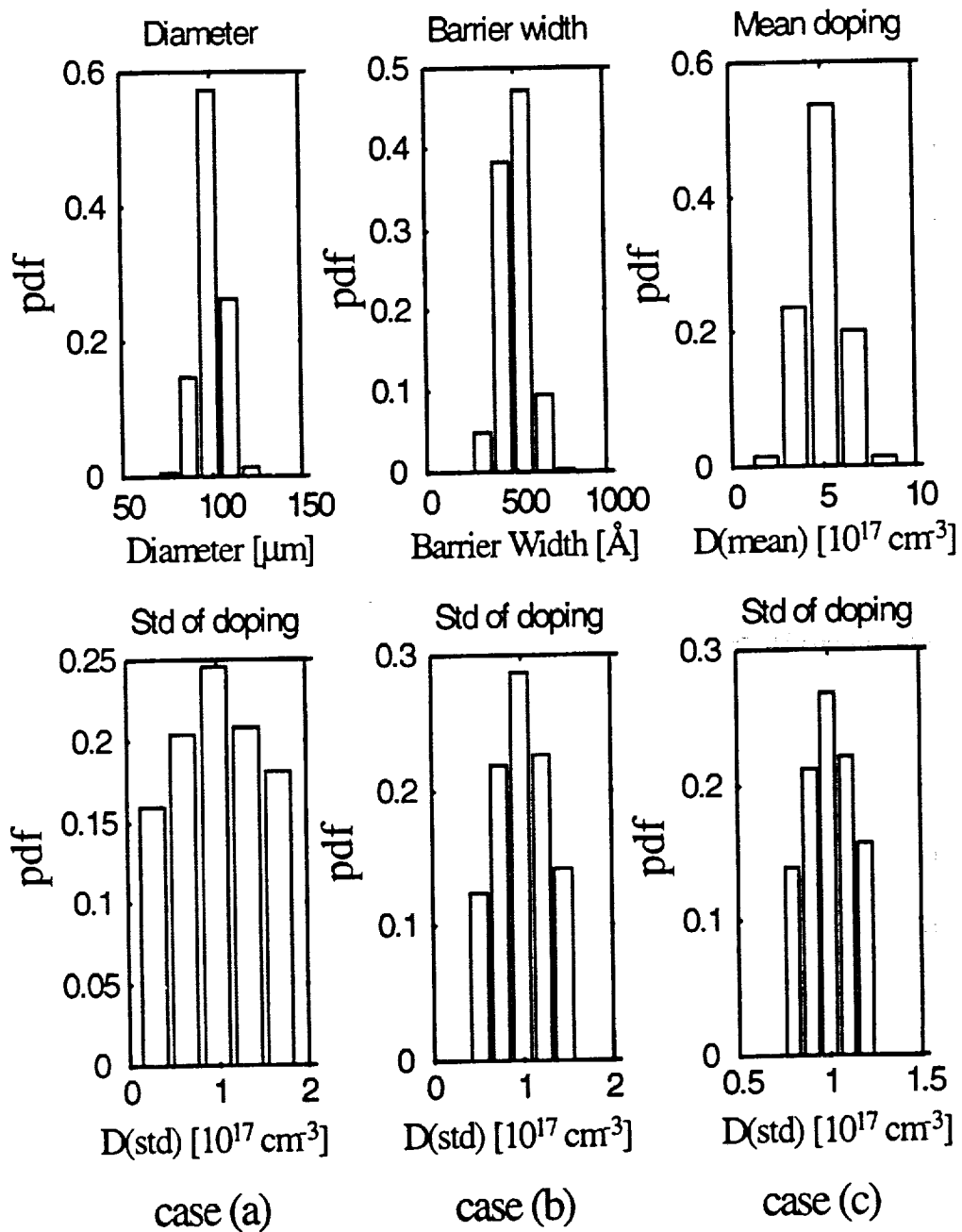
Figure 54 - Histograms of input parameters in scenario 3: Std of doping.
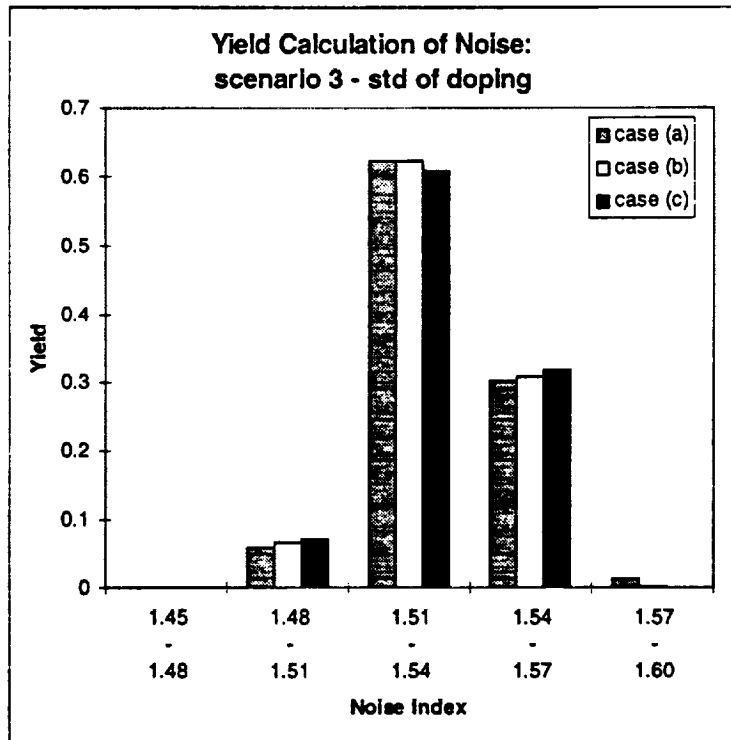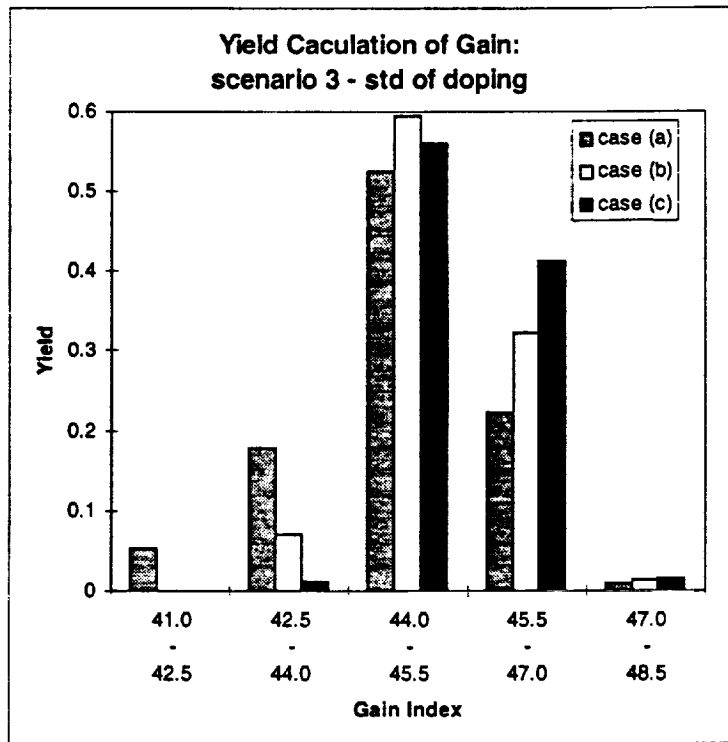
Figure 55 - Final distributions of gain and noise in scenario 3: Std of doping.

6.7 Summary

In this chapter, a systematic methodology for the parametric yield prediction of GaAs MQW APDs has been presented. It was shown that using a small number of test devices with varying device diameters, barrier and well widths, and doping concentrations enables accurate prediction of the expected performance variation of APD gain, noise and device lifetime in larger populations of devices. Neural networks are successfully used for generating the models to characterize the manufacturing variations. This approach provides device designer with the ability to understand the manufacturability of various design options and enables process engineers to determine the consequences of process modifications. This will ultimately allow device parametric yield estimation prior to high-volume manufacturing in order to evaluate the manufacturability rely on design decisions and process capability.

CHAPTER 7

CONCLUSION

7.1 Summary

Throughout this thesis, reliability modeling and parametric yield prediction of GaAs/AlGaAs multiple quantum well (MQW) avalanche photodiodes (APDs) have been presented. These devices are being considered as a potential candidate for an ultra-low noise image capture mechanism application for high definition systems.

First, the effect of various doping methods on the reliability of GaAs/AlGaAs multiple quantum well (MQW) avalanche photodiode (APD) structures fabricated by molecular beam epitaxy (MBE) was investigated. Reliability was examined by accelerated life tests by monitoring dark current and breakdown voltage. Median device lifetime and the activation energy of the degradation mechanism were computed for undoped, doped-barrier, and doped-well APD structures. Lifetimes for each device structure were examined via a statistically designed experiment. Analysis of variance showed that dark current is affected primarily by device diameter, temperature and stressing time, and breakdown voltage depends on the diameter, stressing time and APD type. It was concluded that the undoped APD has the highest reliability, followed by the

doped well and doped barrier devices, respectively. To determine the source of the degradation mechanism for each device structure, failure analysis using the electron-beam induced current method was performed. This analysis revealed some degree of device degradation caused by ionic impurities in the passivation layer, and energy-dispersive spectrometry subsequently verified the presence of ionic sodium as the primary contaminant. However, since all device structures were similarly passivated, sodium contamination alone did not account for the observed variation between the differently doped APDs. This effect was explained by dopant migration during stressing, which was verified by free carrier concentration measurements using the capacitance-voltage technique.

Reliability modeling provided one method for estimating device performance as a function of process variables. Since literally millions of these devices must be fabricated for imaging arrays, it is critical to evaluate potential performance variations of individual devices in light of the fact that even in a defect-free manufacturing environment, random variations in the APD fabrication process lead to varying levels of device performance. Accurate device performance prediction requires precise characterization of these manufacturing variations. Therefore, a novel methodology for modeling the parametric yield prediction of GaAs MQW APDs has also been presented. The approach described requires a model of the probability distribution of each of the relevant process variables, as well as a model to account for the correlation between this measured process data and device performance metrics. The availability of these models enables the computation of the joint density function required for predicting performance using the Jacobian

transformation method. The resulting density function can then be numerically integrated to determine parametric yield. Since they have demonstrated the capability of highly accurate function approximation and mapping of complex, nonlinear data sets, neural networks has been used as a tool for generating the models described above. In apply this methodology to the MQW APDs, it was shown that using a small number of test devices with varying active diameters, barrier and well widths, and doping concentrations enables accurate prediction of the expected performance variation of APD gain and noise in larger populations of devices. This approach will ultimately allow device yield prediction prior to high-volume manufacturing in order to evaluate the manufacturability rely on both design specifications and process capability.

7.2 Suggestions for Future Work

Neural network modeling for parametric yield of GaAs MQW APDs have been accomplished in this thesis. However, it was a nontrivial effort to obtain the inverse neural network models required for estimating the parametric yield based on device lifetime. Usually one hidden layer is enough to build a neural network model, but two hidden layers were required to build accurate models for device lifetime modeling. One task that needs to be performed in the future is neural network model optimization. Genetic algorithms has been successfully used for parameter optimization of neural networks and recipe synthesis in semiconductor manufacturing process [56]. Thus, if

genetic algorithms are applied for neural network optimization in this application, more accurate and efficient neural network models should be achieved.

Another task to be pursued in the future is to utilize the methodology for calculating parametric yield described in this thesis to semiconductor devices fabricated by other certain manufacturing processes. For instance, parameter variation for the high electron mobility transistor (HEMT) fabricated in molecular beam epitaxy can be investigated using this methodology. The device variable can be modeled by measured data or device simulations, such as ATLAS.

In addition, this methodology can also be applied for modeling circuit performance. For example, the parameter variation for CMOS circuit can be predicted using this approach. The circuit variables can be modeled by measured data or SPICE circuit simulations. It was shown that this approach is superior to the prevailing Monte Carlo method by reducing the computation load and relaxing the assumption of a specific statistical distribution. If parametric yield prediction for newly developed circuits using a given manufacturing process is needed, this new methodology can predict parametric yield with a small number of test structures prior to high-volume manufacturing in order to evaluate the impact on manufacturability of both design specifications and process capability.

Publications

- I. Yun, H. Menkara, Y. Wang, I. Oguzman, J. Kolnik, K. F. Brennan, G. S. May, C. J. Summers, and B. K. Wagner, "Reliability Assessment of Multiple Quantum Well Avalanche Photodiodes," *1995 IEEE International. Reliability Physics Symposium (IRPS) Proceedings, 33rd Annual*, April 1995.

- I. Yun, H. Menkara, Y. Wang, I. Oguzman, J. Kolnik, K. F. Brennan, G. S. May, C. J. Summers, and B. K. Wagner, "Effect of Doping on the Reliability of GaAs Multiple Quantum Well Avalanche Photodiodes," *IEEE Transactions On Electron Devices*, vol. 44, no. 4, April 1997.

- I. Yun, and G. S. May, "Evaluating the Manufacturability of GaAs/AlGaAs Multiple Quantum Well Avalanche Photodiodes Using Neural Networks," *21st International Electronics Manufacturing Technology Symposium Proceedings*, Oct. 1997.

- I. Yun, and G. S. May, "Parametric Yield Estimation of GaAs/AlGaAs Multiple Quantum Well Avalanche Photodiodes Using Neural Networks," *Intelligent Engineering Systems Through Artificial Neural Networks*, vol. 7, (C. H. Dagli, Ed.), New York: ASME Press, 1997.

- I. Yun, and G. S. May, "Parametric Yield Modeling of GaAs Multiple Quantum Well Avalanche Photodiodes," to be published.

APPENDIX A

Calculation of Free Carrier Concentration from the Capacitance-Voltage Technique for MQW APDs

Let assume that the APD considered as a parallel-plate capacitor. Let A is the device area and ε is the semiconductor permittivity and C_p is the package capacitance and C_m is the measured capacitance from the HP LCZ meter. Let assume M measured capacitance are obtained from HP LCZ meter and assume two measured capacitance $C_{m(k+1)}$ and $C_{m(k-1)}$ at two different bias voltage V_{k+1} and V_{k-1}, respectively.

The actual capacitance (C_{ak}) is calculated by

$$C_{ak} = C_{mk} - C_p \quad \text{for k=1,...,M.} \tag{A.1}$$

Hence, the depletion width is expressed in the following:

$$W_k = \frac{\varepsilon \cdot A}{C_{ak}} \tag{A.2}$$

Now, we can approximate $d(1/C^2)/dV$ by using $\Delta(1/C^2)$ and ΔV as follows:

$$\Delta V_k = V_{k+1} - V_{k-1} \tag{A.3}$$

$$\Delta\left(\frac{1}{C^2}\right)_k = \frac{1}{\left(C_a^2\right)_{(k+1)}} - \frac{1}{\left(C_a^2\right)_{(k-1)}} \tag{A.4}$$

Hence, the net carrier concentration can be calculated by the approximation:

$$N(W_k) = \frac{2 \cdot \Delta V_k}{q \cdot \varepsilon \cdot A^2 \cdot \Delta\left[(1/C^2)\right]_k} \tag{A.5}$$

Therefore, from the equation (A.2) and (A.5), the distribution of net carrier concentration with respect to the depletion region can be obtained.

APPENDIX B

Sample ATLAS Simulation Program

Light Current and Noise Index Simulation of 10-period Doped-well MQW APDs

```
$
$ 10-period Doped-well MQW photodiode
$
$ Mesh construction
$
mesh rect smooth=4 diag.flip
x.mesh  loc=0    s=75
x.mesh  loc=75.0 s=75
y.mesh  loc=0.0          s=0.4
y.mesh  loc=0.96               s=0.4
y.mesh  loc=0.97               s=0.0025
y.mesh  loc=1.525     s=0.0025
y.mesh  loc=2.08               s=0.0025
y.mesh  loc=2.09               s=0.4
y.mesh  loc=3.05               s=0.4
$
$ Structure Definition
$
region  number=1 x.min=0 x.max=75 y.min=0 y.max=1.0 gaas
region  number=2 x.min=0 x.max=75 y.min=1.0 y.max=1.05 gaas
region  number=3 x.min=0 x.max=75 y.min=1.05 y.max=1.1 material=AlGaAs
x.composition=0.42
region  number=4 x.min=0 x.max=75 y.min=1.1 y.max=1.15 gaas
region  number=5 x.min=0 x.max=75 y.min=1.15 y.max=1.2 material=AlGaAs
x.composition=0.42
region  number=6 x.min=0 x.max=75 y.min=1.2 y.max=1.25 gaas
region  number=7 x.min=0 x.max=75 y.min=1.25 y.max=1.3 material=AlGaAs
x.composition=0.42
region  number=8 x.min=0 x.max=75 y.min=1.3 y.max=1.35 gaas
region  number=9 x.min=0 x.max=75 y.min=1.35 y.max=1.4 material=AlGaAs
x.composition=0.42
region  number=10 x.min=0 x.max=75 y.min=1.4 y.max=1.45 gaas
```

region number=11 x.min=0 x.max=75 y.min=1.45 y.max=1.5 material=AlGaAs
x.composition=0.42
region number=12 x.min=0 x.max=75 y.min=1.5 y.max=1.55 gaas
region number=13 x.min=0 x.max=75 y.min=1.55 y.max=1.6 material=AlGaAs
x.composition=0.42
region number=14 x.min=0 x.max=75 y.min=1.6 y.max=1.65 gaas
region number=15 x.min=0 x.max=75 y.min=1.65 y.max=1.7 material=AlGaAs
x.composition=0.42
region number=16 x.min=0 x.max=75 y.min=1.7 y.max=1.75 gaas
region number=17 x.min=0 x.max=75 y.min=1.75 y.max=1.8 material=AlGaAs
x.composition=0.42
region number=18 x.min=0 x.max=75 y.min=1.8 y.max=1.85 gaas
region number=19 x.min=0 x.max=75 y.min=1.85 y.max=1.9 material=AlGaAs
x.composition=0.42
region number=20 x.min=0 x.max=75 y.min=1.9 y.max=1.95 gaas
region number=21 x.min=0 x.max=75 y.min=1.95 y.max=2.0 material=AlGaAs
x.composition=0.42
region number=22 x.min=0 x.max=75 y.min=2.0 y.max=2.05 gaas
region number=23 x.min=0 x.max=75 y.min=2.05 y.max=3.05 gaas
$
$ Node Definition
$
electrode   name=cathode number=1 top
electrode   name=anode number=2 bottom
$
$ Doping configuration
$
doping   uniform conc=3e18 p.type direction=y regions=1
doping   uniform conc=1.65e18 p.type direction=y y.min=1.115 y.max=1.120
doping   uniform conc=1.5e18 n.type direction=y y.min=1.130 y.max=1.135
doping   uniform conc=1.65e18 p.type direction=y y.min=1.215 y.max=1.220
doping   uniform conc=1.5e18 n.type direction=y y.min=1.230 y.max=1.235
doping   uniform conc=1.65e18 p.type direction=y y.min=1.315 y.max=1.320
doping   uniform conc=1.5e18 n.type direction=y y.min=1.330 y.max=1.335
doping   uniform conc=1.65e18 p.type direction=y y.min=1.415 y.max=1.420
doping   uniform conc=1.5e18 n.type direction=y y.min=1.430 y.max=1.435
doping   uniform conc=1.65e18 p.type direction=y y.min=1.515 y.max=1.520
doping   uniform conc=1.5e18 n.type direction=y y.min=1.530 y.max=1.535
doping   uniform conc=1.65e18 p.type direction=y y.min=1.615 y.max=1.620
doping   uniform conc=1.5e18 n.type direction=y y.min=1.630 y.max=1.635
doping   uniform conc=1.65e18 p.type direction=y y.min=1.715 y.max=1.720
doping   uniform conc=1.5e18 n.type direction=y y.min=1.730 y.max=1.735
doping   uniform conc=1.65e18 p.type direction=y y.min=1.815 y.max=1.820
doping   uniform conc=1.5e18 n.type direction=y y.min=1.830 y.max=1.835
doping   uniform conc=1.65e18 p.type direction=y y.min=1.915 y.max=1.920
doping   uniform conc=1.5e18 n.type direction=y y.min=1.930 y.max=1.935
doping   uniform conc=3e18 n.type direction=y regions=23

```
$
$ Model Definition
$
material material=GaAs taup0=1.e-9 taun0=1.e-9
impact    selber an1=299400 an2=299400 bn1=684800 bn2=684800 ap1=221500 ap2=221500
bp1=657000 bp2=657000 betan=1.6 betap=1.75 egran=222000
models  material=GaAs srh auger conmob fldmob print
$
$ Light source definition
$
beam    num=1 x.origin=37.5 y.origin=-1.0 angle=90.0 wavelength=.8 min.window=-9.0
max.window=9.0
$
$ Find initial solution
$
symb    newton carr=0
solve   init
symb    newton carr=2
method  trap autonr climit=75000 ctolt.fact=500.0 maxtrap=10
solve   prev
output    e.field j.electron e.velocity e.mobility h.mobility qss e.temp h.temp val.band con.band
qfn qfp impact recomb tot.doping
save outf=MQWIV7s2a2.out
solve    b1=1
$
$ Find I-V curve using voltage ramp
$
log        outf=MQWIV7s2a2.log master
solve   prev   v1=0.0  vstep=-2    vfinal=-20 elect=1
solve   prev   v1=-21     vstep=-1    vfinal=-36 elect=1
solve   prev   v1=-36.2   vstep=-0.05    vfinal=-38.5 elect=1
save outf=MQWIV39a2.out
tonyplot MQWIV7s2a2.log
$
$ Calculation of alpha(n) and alpha(p)
$
plot.1d alphan  a.x=37.5 b.x=37.5 a.y=1.0 b.y=3.05 points outfile=andw1.dat ascii
plot.1d alphap  a.x=37.5 b.x=37.5 a.y=1.0 b.y=3.05 points outfile=apdw1.dat ascii
end
```

References

[1] Y. Apanovich, R. Cottle, E.Lyumkis, B. Polsky, A. Shur, P. Blakey, C. Hill, and P. Ashburn, "2D simulation of heterojunction devices including energy balance and lattice," *ESSDERC '94*, pp. 463-466, 1994

[2] S. Nassif, A. Strojwas, and S. Director, "FABRICS II: A Statistical Simulator of the IC Fabrication Process," *IEEE Trans. CAD Integrated Circuits & Systems*, vol. CAD-1, no. 3, pp. 40-47, January, 1984.

[3] I. Chen and A. J. Strojwas, "A methodology for optimal test structure design for statistical process characterization and diagnosis," *IEEE Trans. CAD Integrated Circuits & Systems*, vol.CAD-6, no.4, pp.592-600, July, 1987

[4] K. Eshbaugh, "Generation of Correlated Parameters for Statistical Circuit Simulation," *IEEE Trans. CAD*, vol. 11, no. 10, pp. 1198-1206, Oct., 1992.

[5] C. Chao and L. Milor, "Performance Modeling of Analog Circuits Using Additive Regression Splines," *Proc. CICC*, pp. 301-304, 1994.

[6] W. Joyce, K. Liou, F. Nash, P. Bossard, and R. Hartman, "Methodology of Accelerated Aging," *AT&T Tech. Journal*, vol. 64, no. 3, March, 1985.

[7] F. Nash, *Estimating Device Reliability*, Boston: Kluwer, 1993.

[8] W. Hines and D. Montgomery, *Probability and Statistics in Engineering and Management Science*, New York, NY: Wiley, 1980.

[9] B. Kim and G. May, "Modeling Reactive Ion Etching of Silicon Dioxide Films Using Neural Networks," *Proc. 1994 Electronic Components & Technology Conference*, pp. 273-278, May, 1994.

[10] S. Han, M. Ceiler, S. Bidstrup, P. Kohl, and G. May, "Modeling the Properties of PECVD Silicon Dioxide Films Using Optimized Back-Propagation Neural Networks," *IEEE Trans. Comp., Pack., & Manufac. Tech.*, vol 17, no. 2, pp. 174-182, June, 1994.

[11] M. Baker, C. Himmel, and G. May, "Time Series Modeling of Reactive Ion Etching Using Neural Networks," *IEEE Trans. Semi. Manufac.*, vol. 8, no. 1, pp. 62-71, Feb. 1995.

[12] Z. Nami, A. Erbil, and G. May, " Semi-Empirical MOCVD Modeling Using Neural Networks," *Proceeding of the 1994 SPIE Conference on Microelectronic Manufacturing*, vol. 2334, pp. 295-303, 1994.

[13] J. N. Hollenhorst, O. G. Lorimor, and L. Marchut, "Long wavelength photodetectors: Performance and Reliability," *SPIE Proc. Int. Soc. Opt. Eng.*, vol. 1174, pp. 88-93, 1989.

[14] Y. Zebda, J. Hinckley, P. Bhattacharya, J. Singh, and F-Y. Juang, "High-speed Multiquantum Well Avalanche Photodiodes," *SPIE Proc. Int. Soc. Opt. Eng.*, vol. 861, pp. 125-129, 1987.

[15] W. Kuebart, O. Hildebrand, and B. Kramer, "Status and trends of indium-phosphide-based avalanche photodiodes and optoelectronic integrated circuits," *SPIE Proc. Int. Soc. Opt. Eng.*, vol. 2149, pp. 278-289, 1994.

[16] R. H. Haitz, A. Goetzberger, R. M. Scarlett, and W. Shockley, "Avalanche effects in silicon p-n junctions. I. Localized photomultiplication studies on microplasmas," *J. Appl. Phys.*, vol. 34, 1963

[17] T. Kaneda, "Silicon and Germanium Avalanche Photodiodes," W. T. Tsang, Ed., *Semiconductors and Semimetals*, vol. 22, Part D, New York: Academic, pp. 247-328, 1985.

[18] M. Niwa, Y. Tashiro, K. Minemura, and H. Iwasaki, " High Sensitivity HI-LO Germanium Avalanche Photodiode for 1.5 µm Wavelength Region Single Mode Optical Fiber Communication Use," *NEC Res. Dev.*, no.77, pp. 13-21, April, 1985.

[19] N. Susa, H. Nakagome, O. Mikami, H. Ando, and H. Kanbe, "New InGaAs/InP Avalanche Photodiode Structure for the 1-1.6 µm Wavelength Region," *IEEE J. Quantum. Electron.*, QE-16, pp. 864-870, 1980.

[20] R. J. McIntyre, "Multiplication Noise in Uniform Avalanche Photodiodes," *IEEE Trans. Elec. Dev.*, vol. ED-13, no.1, pp.164-168, Jan. 1966.

[21] R. Chin, N. Holonyak, Jr., G. Stillman, J. Tang, and K. Hess, "Impact Ionization in Multilayered Heterojunction Structures," *Electron. Lett.*, vol. 16, 1980.

[22] K. Brennan and C. Summers, "The Variably Spaced Superlattice Energy Filter Quantum Well Avalanche Photodiode: A Solid-State Photomultiplier," *IEEE J. Quantum. Electron.*, vol. QE-23, no. 3, March, 1987.

[23] P. Aristin, A. Torabi, A. Garrison, H. Harris, and C. Summers, "Evaluation of New Multiple Quantum Well Avalanche Photodiode: the MQW, the Doped Barrier and Doped Quantum Well," *Inst. Phys. Conf. Ser.*, no. 120, 1992.

[24] H. Sudo, Y. Nakano, and G. Iwane, "Reliability of Germanium Avalanche Photodiodes for Optical Transmission Systems," *IEEE Trans. Elec. Dev.*, vol. ED-33, no. 1, Jan., 1986.

[25] H. Sudo, M. Suzuki, and N. Miyahara, "Observation of Surface Degradation Mode of InP/InGaAs APDs During Bias-Temperature Test," *IEEE Elec. Dev. Lett.*, vol. EDL-8, no. 9, Sept., 1987.

[26] H. Sudo and M. Suzuki, "Surface Degradation Mechanism of InP/InGaAs APDs," *IEEE J. Lightwave Tech.*, vol. 6, no. 10, Oct. 1988.

[27] Y. Kuhara, H. Terauchi, and H. Nishizawa, "Reliability of InGaAs/InP Long-Wavelength p-i-n Photodiodes Passivated with Polyimide Thin Film," *IEEE J. Lightwave Tech.*, vol. LT-4, no. 7, July, 1986.

[28] J. Bauer and R. Trommer, "Long-Term Operation of Planar InGaAs/InP p-i-n Photodiodes," *IEEE Trans. Elec. Dev.*, vol. ED-35, no. 12, Dec., 1988.

[29] C. Skrimshire, J. Farr, D. Sloan, M. Robertson, P. Putland, J. Stokoe, and R. Sutherland, "Reliability of Mesa and Planar InGaAs PIN Photodiodes," *IEE Proceedings*, vol. 137, pt. J, no. 1, Feb., 1990.

[30] K. Brennan, "The p-n Junction Quantum Well APD: A New Solid State Photodetector for Lightwave Communications Systems and On-Chip Detector Applications," *IEEE Trans. Elec. Dev.*, vol. ED-34, no. 4, pp. 782-792, April 1987.

[31] I. Yun, H. Menkara, K. Brennan, G. May, C. Summers, and B. Wagner, "Effect of Doping on the Reliability of GaAs Multiple Quantum Well Avalanche Photodiodes," *IEEE Trans. Elec. Dev.*, vol. 44, no. 4, pp. 535-544, April, 1997.

[32] A. Torabi, K. Brennan, and C. J. Summers, "Growth and Application of Superlattices and Quantum Wells," *SPIE Proc.*, vol. 835, 1988.

[33] H. M. Menkara, B. K. Wagner, and C. J. Summers, "Gain Properties of Doped GaAs/AlGaAs Multiple Quantum Well Avalanche Photodiode Structures." *Appl. Phys. Lett.*, vol. 66, no. 14, April 1995.

[34] P. Aristin, A. Torabi, A. Garrison, H. Harris, and C. Summers, "New Doped Multiple Quantum Well Avalanche Photodiode: The Doped Barrier Al(0.35)Ga(0.65)As/GaAs Multiple Quantum Well Avalanche Photodiode," *Appl. Phys. Lett.*, vol. 60, no. 1, pp. 85-87, Jan., 1992.

[35] S. M. Sze, *Physics of Semiconductors Devices*, New York: Wiley, 1981.

[36] F. Capasso, W. Tsang, A. Hutchinson, and G. Williams, "Enhancement of Electron Impact Ionization Rate Ratio," *Appl. Phys. Lett.*, vol. 40, 1982.

[37] M. Kinch, "Metal-insulator-semiconductor infrared detectors," *Semiconductors and Semimetals*, vol. 18, R. Willardson and A. Beers, Eds., New York: Academic, 1981.

[38] G. E. Box, W. G. Hunter, and J. S. Hunter, *Statistics for Experimenters*, New York: Wiley, 1978.

[39] E. Pollino, *Microelectronic Reliability*, vol. 2, Boston: Artech House, 1989.

[40] T. B. Vander Wood, "Identification of Particulate Contaminants in IC Manufacture," *Solid State Tech.*, vol. 28, no. 8, Aug., 1985.

[41] P. Blood and J. W. Orton, *The Electrical Characterization of Semiconductors: Majority Carriers and Electron States*, London: Academic Press, 1992.

[42] F. Nash, *Estimating Device Reliability*, Boston: Kluwer, 1993.

[43] Z. Galil and J. Kiefer, "Time- and Space-Saving Computer Methods, Related to Mitchell's DETMAX, for Finding D-Optimum Designs," *Technometrics*, vol. 22, Aug., 1980.

[44] *RS/Discover User's Guide*, BBN Software Products Corporation, June 1988.

[45] B. Richards and P. Footner, *The Role of Microscopy in Semiconductor Failure Analysis*, Oxford; New York: Oxford University Press, 1992.

[46] *ATLAS II User's Manual*, Silvaco International, 1993.

[47] S. Selberherr, *Analysis and Simulation of Semiconductor Devices*, New York, Springer-Verlag, 1984.

[48] K. K. Lin and C. J. Spanos, "Statistical equipment modeling for VLSI manufacturing: an application for LPCVD," *IEEE Trans. on Semi. Manufac.*, vol.3, no.4, pp.216-29, Nov., 1990.

[49] J. Freeman and D. Skapura, *Neural Networks*, Addison-Wesley: New York, 1991.

[50] A. Deif, *Sensitivity Analysis in Linear Systems*, New York, Springer-Verlag, 1983.

[51] J. E. Purviance and M. D. Meehan, "A Sensitivity Figure for Yield Improvement," *IEEE Trans. Microwave Theory and Techniques*, vol.36, no. 2, pp. 413-417, Feb. 1988.

[52] D. Gibson, R. Poddar, G. May, and M. Brooke, "Using Neural Networks to Estimate Probability Density Functions," *1995 World Congress on Neural Networks*, Washington, DC, July 1995.

[53] M. Page, " Analysis of Non-normal Process Distributions," *Semiconductor International*, vol. 17, no. 12, pp. 88-96, Oct. 1994.

[54] D. Gibson, R. Poddar, G. May, and M. Brooke, "Statistically Based Parametric Yield Prediction for Integrated Circuits," *IEEE Trans. Semi. Manufac.*, vol. 10, no.3, August, 1997.

[55] *MATLAB User's Guide*, The Math Works Inc., February, 1993.

[56] S. Han and G. S. May, "Using neural network process models to perform PECVD silicon dioxide recipe synthesis via genetic algorithms," *IEEE Trans. Semi. Manufac.*, vol. 10, no. 2, pp 279-287, May, 1997.

Vita

Ilgu Yun was born on ██e ██, ██7 in ████l, ████a. He received the B.S. degree in Electrical Engineering from Yonsei University in Seoul, Korea in 1990. After his fulfillment of mandatory military service in the Korean Army Athletic Forces in 1992, he joined the Georgia Institute of Technology, where he received the M.S. degree in Electrical and Computer Engineering in 1995. Since he became a member of Georgia Tech Computer Integrated Manufacturing (GTCIM) group under the supervision of Dr. Gary S. May in 1993, he has held the position of Graduate Research Assistant in Electrical and Computer Engineering at Georgia Institute of Technology and has worked on reliability modeling and parametric yield prediction of GaAs multiple quantum well avalanche photodiodes applied to the high definition imaging camera system supported by the National Aviation Space Administration (NASA).

His research interests include process modeling, simulation and control, and yield modeling applied to computer integrated manufacturing for III-V compound semiconductor optoelectronic integrated circuits. He married Hyunjung Cha in 1993, and he has a son, Jiho (Greg).